



Politecnico di Torino

DIPARTIMENTO DI INGEGNERIA MECCANICA E AEROSPAZIALE
Corso di Laurea Magistrale in Automotive Engineering

TESI DI LAUREA MAGISTRALE

**Evaluation of alternative approach for suspension corner
damping by the use of hydraulic top mounts**

Candidato:

Salvatore Marco Cubisino

Matricola 242577

Relatore:

Ch.mo Prof. Andrea Tonoli

Correlatore:

Ch.mo Prof. Nicola Amati

Sommario

Nell'ambito del progetto "Evaluation of alternative approach for suspension corner damping by the use of hydraulic top mounts" si analizzano i benefici dati dall'impiego di supporti idraulici come testa duomo per un sistema di sospensione automobilistica. L'intero progetto si basa su simulazioni numeriche realizzate via MATLAB[®]/Simulink[®]. Pertanto, la modellazione della testa duomo idraulica per mezzo di un sistema di molle, smorzatori e masse è stata il punto di partenza del progetto.

Successivamente, la suddetta testa duomo idraulica è stata inserita in un modello "quarter car" e la sua performance è stata paragonata con un equivalente modello "quarter car", in cui, a differenza del precedente, una comune testa duomo in gomma è stata inserita. Di conseguenza, il modello "quarter car" con la testa duomo in gomma costituisce il modello di riferimento per la valutazione della performance della nuova testa duomo idraulica. In particolare, sono stati sviluppati sia modelli lineari che nonlineari, il primo è stato utilizzato per verificare la robustezza del modello stesso, mentre il secondo è stato utilizzato per valutare la performance rispetto ai modelli di riferimento. Per simulare i modelli lineari sono stati utilizzati dei segnali "chirp", mentre dei profili stradali casuali sono stati usati per completare la simulazione dei modelli nonlineari.

Inoltre, al fine di valutare ulteriori miglioramenti che possano essere raggiunti per mezzo dell'impiego di una testa duomo idraulica, una diversa disposizione della testa duomo rispetto all'ammortizzatore nel modello "quarter car" è stata realizzata e poi verificata. Un leggero miglioramento della performance è stato registrato nel caso dei modelli equipaggiati di testa duomo idraulica.

Infine, per una migliore comprensione delle caratteristiche della testa duomo idraulica un piano di esperimenti (Design of Experiments (DOE)) che considerasse i parametri idraulici della testa duomo idraulica è stato messo a punto. Questa metodologia ha permesso di identificare i parametri più significativi per la performance del modello "quarter car". Inoltre, l'analisi dei risultati ottenuti per mezzo del DOE è stata il punto di partenza per un tentativo preliminare di ottimizzazione della testa duomo idraulica.

Le simulazioni portate a termine impiegando la testa duomo ottimizzata hanno mostrato un importante miglioramento rispetto alla testa duomo in gomma. In più, è stato mostrato che la seconda disposizione per la testa duomo rispetto allo smorzatore può risultare in migliori performance rispetto alla disposizione originale.

Abstract

The scope of “Evaluation of alternative approach for suspension corner damping by the use of hydraulic top mounts” is the analysis of the benefit given by the implementation of a hydraulic mount as the top mount for a vehicle suspension system. The whole project is based on numerical simulations performed by means of MATLAB®/Simulink®. Therefore, the modelling of the selected hydraulic top mount by means of a system of springs, dampers and masses was the starting point of the project.

Afterwards, the aforementioned hydraulic top mount model was inserted into a quarter car model and its performance was compared to that of an equivalent quarter car model employing a rubber top mount, instead. Therefore, the quarter car model with the rubber top mount represented the reference model to assess the performance of the new hydraulic top mount. In particular, both linear and nonlinear quarter car models were developed, the former were used to check the robustness of the model itself and the latter were used to carry out all the comparisons with the reference models. Different chirp signals were used as input for all the linear models, while random road and single asperity signals were employed as inputs for the nonlinear models.

Furthermore, in order to explore the potential improvements that could be achieved by implementing the hydraulic top mount, a second arrangement for the relative position of the hydraulic top mount and the shock absorbed in the quarter car model was modelled and, then, tested. A slight better performance was recorded in the case of models containing the hydraulic top mount.

Finally, for a better understanding of the characteristics of the hydraulic top mount, a Design of Experiments (DOE) that takes into account the parameters of the mount hydraulic components was carried out; DOE methodology allowed one to identify the most influential factors in the quarter car model performance. Additionally, the analysis of DOE results was employed as a starting point to perform a first optimization of the hydraulic top mount.

The simulation carried out employing the optimized top mount showed a relevant improvement with respect to the base hydraulic top mount and, a fortiori, with respect to the rubber top mount case. Moreover, it was shown that the second arrangement for the hydraulic top mount in the quarter car model could give even better performance than the model with the standard arrangement.

For my family
Alla mia famiglia

Contents

Sommario	iii
Abstract	iv
List of Figures	ix
List of Tables	xvii
List of Appendices	xx
List of Symbols	xxi
Nomenclature	xxiv
1 Introduction	1
1.1 The Role of Suspension System and Top Mount	1
1.2 Rubber Mounts Structure	2
1.3 Hydraulic Mounts Structure	2
1.4 Objectives of the Research	5
2 Literature Review	6
2.1 Ride Comfort Background	6
2.2 Suspension Settings	8
2.3 Top Mount Influence	8
2.4 Hydraulic Mount Modelling	11
2.5 Applications: Engine Suspension	13
2.6 Hydraulic Bushings and Mounts in Different Chassis Applications	15
3 Theory	17
3.1 The Effect of Vibration on Human Body	17
3.2 Relevant Quantities for Comfort Performance	19
3.3 Linear Models	20
3.3.1 Hydraulic Top Mount Mathematical Model	20
3.3.2 Quarter Car Model with Hydraulic Top Mount	23
3.3.3 Traditional Rubber top Mount	26
3.3.4 Quarter Car Model with Traditional Top Mount	27

3.4	Nonlinear Models	28
3.4.1	Quarter Car Model with Hydraulic Top Mount	28
3.4.2	Quarter Car Model with Rubber Top Mount	29
3.4.3	A Different Arrangement for the Hydraulic Top Mount	30
4	Simulation Models	32
4.1	Simulink® Models	32
4.1.1	Linear Model for the Hydraulic Top Mount	32
4.1.2	Linear Model for the Rubber Top Mount	33
4.1.3	Simulink® Linear Quarter car Model with the Hydraulic Top Mount	34
4.1.4	Simulink® Nonlinear Quarter car Model with the Hydraulic Top Mount	35
4.1.5	Quarter car models with traditional mount	35
4.2	Simulink® Nonlinear Quarter car Model with the Hydraulic Top Mount in Series with the Strut	35
4.3	Choice of Model Parameters	37
4.3.1	Rubber and Hydraulic Top Mounts	37
4.3.2	Linear Quarter Car Models	39
4.3.3	Nonlinear Quarter Car Models	42
5	Simulation Results	44
5.1	Linear Models	44
5.1.1	Hydraulic Top Mount	44
5.1.2	Rubber Top Mount	47
5.1.3	Quarter Car Model with the Hydraulic Top Mount	49
5.1.4	Quarter Car Model with the Rubber Top Mount	53
5.2	Nonlinear Models	55
5.2.1	Input Signals	57
5.2.2	Quarter Car Model with the Hydraulic Top Mount	59
5.2.3	Quarter Car Model with the Rubber Top Mount	64
5.2.4	Quarter Car Model with the Hydraulic Top Mount in Series with the Suspension Strut	73
5.3	Concluding Remarks	80
6	Design of Experiments and Sensitivity Analysis	81
6.1	Design of Experiments Methodology	81
6.2	Analysis of Variances and Percentages of Contribution	82
6.3	ANOVA and Percentages of Contribution Results	85
7	Top Mount Dynamic Stiffness Influence on Performance	96
7.1	The Role of the Hydraulic Top Mount Dynamic Stiffness on the Sprung Mass Acceleration	96
7.2	The Physical Characteristics of the Hydraulic Top Mount Dynamic Stiffness	100

7.3	First Attempt of Hydraulic Top Mount Parameters Optimization	101
7.4	The Role Top Mount Dynamic Stiffness on the Unsprung Mass Acceleration	105
7.5	Hydraulic Top Mount in Series with the Suspension Strut	106
8	Conclusions and Recommendations	109
	Bibliography	112
A	Summary of Linear Differential Equations and Transfer Functions	115
B	Bounce and Hop Mode	117
B.1	Bounce and Wheel Hop Frequencies	117
B.2	Frequency response	119
B.2.1	Disabled Hydraulic Mount	119
B.2.2	Enabled Hydraulic mount	120
C	Quarter Car Model Plots	123
C.1	Linear Quarter Car Models with the Hydraulic Top Mount	123
C.1.1	Time Simulation	123
C.1.2	Bode Diagrams	125
C.2	Linear Quarter Car Models with the Rubber Top Mount	128
C.2.1	Time Simulation	128
C.2.2	Bode Diagrams	129
C.3	Nonlinear Quarter Car Models with the Hydraulic Top Mount	132
C.3.1	Time Histories	132
C.4	Nonlinear Quarter Car Model with the Rubber Top Mount	134
C.4.1	Time Histories	134
C.5	Nonlinear Quarter Car Models with the Hydraulic Top Mount in Series with Suspension Strut	135
C.5.1	Time Histories	135
	Vita Auctoris	137

List of Figures

1.1	McPherson suspension strut comprising of coil spring, hydraulic shock absorber and Rubber Top Mount [1].	2
1.2	3D model of a suspension elastomeric top mount showing the steel sleeve and its rubber insert in section [4].	3
1.3	3D Model of an actual hydraulic mount employed in engine suspension. Inertia track and decoupler are visible [5].	4
1.4	Sketch of a common hydraulic mount employed of engine suspension application [6].	4
2.1	Sketch of the quarter car model used by Kaldas et al [11].	9
2.2	Sketch of the damper top mount model used by Kaldas et. al in their researches [11], [12].	10
2.3	Sketch of the actual hydraulic mount (a) and of the lumped parameter model (b) for the hydraulic mount studied by Golnaraghi et al.[7]	12
2.4	Sketch of the nonlinear model for the hydraulic mounts used in [20]	16
3.1	Tolerance limit curves of human body to vibrations at different exposure times according to ISO – 2631 [8].	18
3.2	Bode plot of the transfer function H_{2631} employed to filter the data of sprung mass acceleration coming from the simulations.	19
3.3	Section of the hydraulic top mount analyzed in this study [26]. (a) Primary Rubber, (b) Inertia Track, (c) Secondary Rubber, (d) Oil	20
3.4	Sketch of the lumped parameter model for the hydraulic top mount.	21
3.5	Hydraulic part of the top mount model.	22
3.6	Sketch of the quarter car model integrated with the hydraulic top mount, which works in series with the damper.	24
3.7	Sketch of the model employed for the traditional rubber top mount.	26
3.8	Sketch of the quarter car model with a traditional rubber mount in series to the suspension damper.	27
3.9	Sketch of the nonlinear quarter car model with the hydraulic top mount.	29
3.10	Sketch of the nonlinear quarter car model with the rubber top mount.	30
3.11	Sketch of the quarter car model with the hydraulic top mount in series with the whole suspension strut.	31

4.1	Block diagram for the main system of the hydraulic top mount.	33
4.2	Block diagram for the subsystem for the hydraulic mount.	33
4.3	Block diagram for the rubber top mount model.	34
4.4	Block diagram for the quarter car model with the hydraulic top mount built with Simulink®.	36
4.5	Block diagram for the subsystem composed by the series of damper and hydraulic mount in quarter car model built with Simulink®.	37
4.6	Block diagram for the nonlinear quarter car model with the hydraulic top mount built with Simulink®.	38
4.7	Block diagram for the subsystem of the nonlinear quarter car model with the hydraulic top mount.	39
4.8	Block diagram for the nonlinear quarter car model with the hydraulic top mount in series with the strut.	40
4.9	Block diagram for the subsystem of the nonlinear quarter car model with the hydraulic top mount in series with the strut.	41
4.10	Sketch of the suspension assembly in front view.	42
4.11	Damper characteristic curves: component level (blue) and wheel centre (red)	43
5.1	Input displacement for the hydraulic top mount time simulation.	45
5.2	Variation in time of the force exerted by the hydraulic top mount due to the chirp signal used as input.	46
5.3	Variation of the hydraulic top mount dynamic stiffness in Laplace domain.	46
5.4	Comparison between the analytic Bode diagram and the numerical one for the hydraulic top mount model.	47
5.5	Variation in time of the force f'_t generated by the rubber top mount due to a chirp input displacement.	48
5.6	Dynamic stiffness variation in function of frequency for the rubber top mount.	49
5.7	Comparison between numerical and analytic transfer function for the rubber top mount.	50
5.8	Time history of the sprung mass displacement in the linear quarter car model with the hydraulic top mount.	51
5.9	Time history of the unsprung mass displacement in the linear quarter car model with the hydraulic top mount.	51
5.10	Bode diagram for amplitude and phase for the transfer function between the sprung mass displacement and the input displacement in the case of the quarter car model with the hydraulic top mount.	52
5.11	Bode diagram for amplitude and phase for the transfer function between the unsprung mass displacement and the input displacement in the case of the quarter car model with the hydraulic top mount.	53
5.12	Comparison between analytic and estimated amplitude Bode diagrams of the transfer function I of the quarter car model with the hydraulic top mount.	53

5.13	Sprung mass displacement in function of time for the quarter car model with rubber the rubber top mount.	54
5.14	Unsprung mass displacement in function of time for the quarter car model with rubber the rubber top mount.	54
5.15	Bode diagram for amplitude and phase of the transfer function I between the sprung mass displacement and the input signal in the case of the quarter car with the rubber top mount.	56
5.16	Bode diagram for amplitude and phase of the transfer function K between the unsprung mass displacement and the input signal in the case of the quarter car model with the rubber top mount.	56
5.17	Comparison between the analytic and estimated amplitude bode diagram of the transfer function I for the quarter car model with the rubber top mount.	57
5.18	Input road signal employed to run the simulation of the nonlinear quarter car models.	58
5.19	Input road signals in time domain employed to run the simulation of the nonlinear quarter car models.	58
5.20	Profile of the single asperity signal in function of the travelled distance and input signal in function of time.	59
5.21	Sprung mass displacement in function of time for the quarter car model with the hydraulic top mount in the case of A-class road input (a) and D-class road input (b).	60
5.22	Unsprung mass displacement in function of time for the quarter car model with the hydraulic top mount in the case of A-class road input (a) and D-class road input (b).	60
5.23	Displacement of the sprung mass due to single asperity input for the quarter car model with the hydraulic top mount.	61
5.24	Displacement of the unsprung mass due to single asperity input for the quarter car model with the hydraulic top mount.	62
5.25	Fast Fourier Transform of the sprung mass displacement for the nonlinear quarter car model with hydraulic mount.	63
5.26	Fast Fourier Transform of the unsprung mass displacement for the nonlinear quarter car model with hydraulic mount.	64
5.27	Fast Fourier Transform of the sprung mass acceleration for the nonlinear quarter car model with hydraulic mount.	64
5.28	Fast Fourier Transform of the unsprung mass acceleration for the nonlinear quarter car model with hydraulic mount.	65
5.29	FFT plots of the sprung and unsprung mass displacement for the nonlinear quarter car model with the hydraulic mount due to single asperity input signal.	65

5.30	FFT plots of the sprung and unsprung mass acceleration for the nonlinear quarter car model with the hydraulic mount due to single asperity input signal.	66
5.31	Sprung Mass Displacement in function of time for the quarter car model with the rubber top mount in the case of A-class road input (a) and D-class road input (b).	66
5.32	Unsprung Mass Displacement in function of time for the quarter car model with the rubber top mount in the case of A-class road input (a) and D-class road input (b).	68
5.33	Displacement of the sprung mass due to single asperity input for the quarter car model with the rubber top mount.	68
5.34	Displacement of the unsprung mass due to single asperity input for the quarter car model with the rubber top mount.	69
5.35	Fast Fourier Transform of the sprung mass displacement for the nonlinear quarter car model with the rubber top mount.	70
5.36	Fast Fourier Transform of the unsprung mass displacement for the nonlinear quarter car model with the rubber top mount.	70
5.37	Fast Fourier Transform of the sprung mass acceleration for the nonlinear quarter car model with the rubber top mount.	71
5.38	Fast Fourier Transform of the unsprung mass acceleration for the nonlinear quarter car model with the rubber top mount.	71
5.39	Fast Fourier Transform of sprung and unsprung mass displacement for the nonlinear quarter car model with the rubber top mount.	72
5.40	Fast Fourier Transform of sprung and unsprung mass displacement for the nonlinear quarter car model with the rubber top mount.	72
5.41	Sprung mass displacement in function of time for the quarter car model with the hydraulic top mount in series with the strut in the case of A-class road input (a) and D-class road input (b).	73
5.42	Unsprung mass displacement in function of time for the quarter car model with the hydraulic top mount in series with the strut in the case of A-class road input (a) and D-class road input (b).	74
5.43	Displacement of the sprung mass due to single asperity input for the quarter car model with the hydraulic top mount in series with the strut.	75
5.44	Displacement of the unsprung mass due to single asperity input for the quarter car model with the hydraulic top mount in series with the strut.	75
5.45	Fast Fourier Transform of the sprung mass displacement for the nonlinear quarter car model with hydraulic mount in series with the suspension strut.	77
5.46	Fast Fourier Transform of the unsprung mass displacement for the nonlinear quarter car model with hydraulic mount in series with the suspension strut.	77
5.47	Fast Fourier Transform of the sprung mass acceleration for the nonlinear quarter car model with hydraulic mount in series with the suspension strut.	78

5.48	Fast Fourier Transform of the unsprung mass acceleration for the nonlinear quarter car model with hydraulic mount in series with the suspension strut.	78
5.49	Fast Fourier Transform of sprung and unsprung mass displacement for the nonlinear quarter car model with hydraulic mount in series with the suspension strut.	79
5.50	Fast Fourier Transform of sprung and unsprung mass acceleration for the nonlinear quarter car model with hydraulic mount in series with the suspension strut.	79
6.1	Effect of factor c_2 on the variation of $\ddot{x}_{u,RMS}$ and $\ddot{x}_{s,RMS}$	86
6.2	Effect of factor k_2 on the variation of $\ddot{x}_{u,RMS}$ and $\ddot{x}_{s,RMS}$	86
6.3	Effect of factor c_3 on the variation of $\ddot{x}_{u,RMS}$ and $\ddot{x}_{s,RMS}$	89
6.4	Effect of factor m_3 on the variation of $\ddot{x}_{u,RMS}$ and $\ddot{x}_{s,RMS}$	89
6.5	$c_2 - k_2$ interaction plots for $\ddot{x}_{u,RMS}$ and $\ddot{x}_{s,RMS}$	90
6.6	$c_2 - c_3$ interaction plots for $\ddot{x}_{u,RMS}$ and $\ddot{x}_{s,RMS}$	90
6.7	$c_2 - m_3$ interaction plots for $\ddot{x}_{u,RMS}$ and $\ddot{x}_{s,RMS}$	91
6.8	$k_2 - c_3$ interaction plots for $\ddot{x}_{u,RMS}$ and $\ddot{x}_{s,RMS}$	91
6.9	$k_2 - m_3$ interaction plots for $\ddot{x}_{u,RMS}$ and $\ddot{x}_{s,RMS}$	92
6.10	$c_3 - m_3$ interaction plots for $\ddot{x}_{u,RMS}$ and $\ddot{x}_{s,RMS}$	92
6.11	Bar chart for the contribution of the significant factors and interactions for the unsprung mass acceleration.	94
6.12	Bar chart for the contribution of the significant factors and interactions for the sprung mass acceleration.	95
7.1	Variation of the dynamic stiffness amplitude according to the variation of the secondary rubber stiffness k_2	97
7.2	Variation of the dynamic stiffness phase according to the variation of the secondary rubber stiffness k_2	97
7.3	Variation of the dynamic stiffness amplitude according to the variation of the fluid viscosity c_3	98
7.4	Variation of the dynamic stiffness phase according to the variation of the fluid viscosity c_3	98
7.5	Variation of the dynamic stiffness according to the variation of the fluid inertia m_3	99
7.6	Variation of the dynamic stiffness phase according to the variation of the fluid inertia m_3	99
7.7	Dynamic stiffness Bode Plot in case of the tuned parameters.	103
7.8	Comparison between the FFT of the sprung mass acceleration for quarter car model with the hydraulic top mount before and after the tuning and for the quarter car model with the rubber top mount.	103

7.9	Comparison between the FFT of the sprung mass displacement for quarter car model with the hydraulic top mount before and after the tuning.	104
7.10	Comparison between the Road Holding Index time histories for the two different set of parameters for the Hydraulic Top Mount	104
7.11	Variation of RMS values of the sprung mass acceleration due to the variation of the wheel stiffness (k_w) in the case of the reference hydraulic top mount (blue), tuned hydraulic top mount (red) and rubber top mount (yellow). . .	105
7.12	FFT of the sprung mass acceleration for the two configurations of the quarter car model with the hydraulic top mount and for the quarter car model with the rubber top mount.	107
7.13	Sensitivity of the two different configurations for the hydraulic top mount to the variation of tire stiffness.	108
B.1	Fast Fourier Transform for the displacement of the sprung mass.	119
B.2	Fast Fourier Transform for the displacement of the unsprung mass.	120
B.3	Fast Fourier Transform of the sprung mass displacement with the enabled hydraulic top mount.	121
B.4	Fast Fourier Transform of the unsprung mass displacement with the enabled hydraulic top mount.	121
B.5	Comparison between Fast Fourier Transform of the sprung mass displacement for the two different cases.	122
B.6	Comparison between Fast Fourier Transform of the unsprung mass displacement for two different cases.	122
C.1	Input signal for the linear quarter car models.	123
C.2	Time history of the sprung mass acceleration in the linear quarter car model with the hydraulic top mount.	124
C.3	Time history of the unsprung mass acceleration in the linear quarter car model with the hydraulic top mount.	124
C.4	Bode diagram for amplitude and phase for the transfer function between sprung mass acceleration and input displacement in case of quarter car model with the hydraulic top mount.	125
C.5	Bode diagram for amplitude and phase for the transfer function between unsprung mass acceleration and input displacement in case of quarter car model with the hydraulic top mount.	125
C.6	Bode diagram for the transfer function K between the acceleration of the sprung mass and the input signal for the quarter car model with the hydraulic top mount.	126
C.7	Bode diagram for the transfer function K between the displacement of the unsprung mass and the input signal for the quarter car model with the hydraulic top mount.	126

C.8	Comparison between the analytic and estimated amplitude Bode diagram of the transfer function L for the quarter car model with the hydraulic top mount.	127
C.9	Sprung mass acceleration in function of time for the quarter car model with the rubber top mount.	128
C.10	Unsprung mass acceleration in function of time for the quarter car model with the rubber top mount.	128
C.11	Bode diagram for amplitude and phase of the transfer function J between the sprung mass acceleration and the input signal in case of quarter car with the rubber top mount.	129
C.12	Bode diagram for amplitude and phase of the transfer function L between the unsprung mass acceleration and the input signal in case of quarter car with the rubber top mount.	129
C.13	Comparison between the analytic and estimated amplitude Bode diagram of the transfer function J for the quarter car model with the rubber top mount.	130
C.14	Comparison between the analytic and estimated amplitude Bode diagram of the transfer function K for the quarter car model with the rubber top mount.	130
C.15	Comparison between the analytic and estimated amplitude Bode diagram of the transfer function L for the quarter car model with the rubber top mount.	131
C.16	Sprung mass acceleration in function of time for the quarter car model with the hydraulic top mount in case of A-class road input (a) and D-class road input (b).	132
C.17	Unsprung mass acceleration in function of time for the quarter car model with the hydraulic top mount in case of A-class road input (a) and D-class road input (b).	132
C.18	Sprung and unsprung mass acceleration in function of time for the quarter car model with the hydraulic top mount in case of single asperity input signal.	133
C.19	Sprung mass acceleration in function of time for the quarter car model with the rubber top mount in case of A-class road input (a) and D-class road input (b).	134
C.20	Unsprung mass acceleration in function of time for the quarter car model with the rubber top mount in case of A-class road input (a) and D-class road input (b).	134
C.21	Sprung and unsprung mass acceleration in function of time for the quarter car model with the hydraulic top mount in case of single asperity input. . .	135
C.22	Sprung mass acceleration in function of time for the quarter car model with the hydraulic top mount in case of A-class road input (a) and D-class road input (b).	135

C.23	Unsprung mass acceleration in function of time for the quarter car model with the hydraulic top mount in case of A-class road input (a) and D-class road input (b).	136
C.24	Sprung and unsprung mass acceleration in function of time for the quarter car model with the hydraulic top mount in case of single asperity input signal.	136

List of Tables

4.1	Values of the parameters for the hydraulic top mount model.	39
4.2	Values of stiffness and damping of suspension component and sprung mass value.	41
4.3	Parameters values for the quarter car model.	42
5.1	Parameters values for the chirp signal employed as input of the simulation for the hydraulic top mount.	45
5.2	Parameters values for the chirp signal employed as simulation input for the linear quarter car models.	49
5.3	Values of RMS acceleration and range for sprung and unsprung mass in the quarter car model with hydraulic mount.	50
5.4	Values of the peak magnitude in dB of sprung and unsprung mass displacements for the quarter car with the rubber top mount.	52
5.5	RMS values of acceleration and range for sprung and unsprung mass in the quarter car model with the rubber top mount.	55
5.6	Values of the peak magnitude in dB of sprung and unsprung mass displacements for the quarter car model with the rubber top mount.	55
5.7	RMS values and range of sprung and unsprung mass accelerations for the quarter car model with the hydraulic top mount.	60
5.8	Components of RMS acceleration values of sprung and unsprung mass accelerations for primary and secondary ride in the case of the quarter car model with and random road inputs.	61
5.9	RMS and range values for the acceleration of sprung and unsprung mass in the case of the nonlinear quarter car model with the hydraulic top mount due to a single asperity signal.	62
5.10	Components of RMS acceleration values of sprung and unsprung mass acceleration for the primary ride and the secondary ride in the case of the quarter car model with the hydraulic top mount and a single asperity input.	62
5.11	RMS values and range of sprung and unsprung mass acceleration for the quarter car model with rubber top mount. Values in parentheses refer to the hydraulic top mount.	67

5.12	Primary and secondary ride components of RMS sprung and unsprung mass acceleration for the quarter car model with the rubber top mount. Values in parentheses refers to the hydraulic top mount.	67
5.13	RMS and range values for the acceleration of sprung and unsprung mass in the case of the nonlinear quarter car model with the rubber top mount due to a single asperity signal. Values in parentheses refer to the hydraulic top mount	69
5.14	Primary and secondary ride components of RMS sprung and unsprung mass acceleration of the quarter car model with the rubber top mount for single asperity input. Values in parentheses refer to the hydraulic top mount. . . .	70
5.15	RMS values and range of sprung and unsprung mass acceleration for the quarter car model with the hydraulic top mount in series with the strut. Values in parentheses refer to standard configuration.	74
5.16	RMS components of sprung and unsprung mass acceleration for the quarter car model with the hydraulic top mount in series with suspension strut. Values in parentheses refer to standard configuration.	74
5.17	RMS and range values for the acceleration of sprung and unsprung mass in the case of the nonlinear quarter car model with the hydraulic top mount in series with the strut due to a single asperity signal.	76
5.18	Primary and secondary ride components of RMS of sprung and unsprung mass acceleration for the quarter car model with the hydraulic top mount in series with the strut. Values in parentheses refer to standard configuration.	76
6.1	Values of each Factor at different levels in the DOE plan.	82
6.2	Factors and interactions limit value for the F-Ratios at 95% confidence level.	84
6.3	ANOVA summary table for $\ddot{x}'_{u,RMS}$	87
6.4	ANOVA summary table for $\ddot{x}'_{s,RMS}$	88
6.5	Sums of Squares and their corrected values for $\ddot{x}_{u,RMS}$	94
6.6	Sum of Squares and their corrected values for $\ddot{x}_{s,RMS}$	95
7.1	New values of RMS acceleration for the sprung mass after the variation of m_3 , k_2 , and c_3 to have a phase peak in secondary ride frequency range. . . .	102
7.2	RMS values of sprung mass acceleration and road holding index for the quarter car model with optimized h. top mount in series with the strut. . . .	107
8.1	Summary of the improvement obtained through the implementation of the hydraulic top mount in the quarter car model in terms or RMS of sprung mass acceleration with respect to the rubber top mount configuration. . . .	110
A.1	Table containing Linear Differential Equation (LDE) and Transfer Function (TF) of the two different types of mounts presented in Chapter 3.	115

A.2	Table containing Linear Differential Equation (LDE) and Transfer Function (TF) for the two different linear quarter car models presented in Chapter 3.	116
B.1	Values of the quarter car model parameters at component level.	118
B.2	Values of quarter car model parameters at the centre of the wheel.	118
B.3	Theoretical values for ride and wheel hop frequencies.	118

List of Appendices

Linear Differential Equations and Transfer Function Summary	115
Bounce and Hop Mode	117
Quarter Car Model Plots	123

List of Symbols

c'_1	Damping of the traditional rubber top mount
k'_1	Stiffness of the traditional rubber top mount
η_{rh}	Road Holding Index
\hat{Q}_y	Corrected Sum of Squares of the factor/interaction y
\hat{Q}_{err}	Corrected Sum of Squares of the error
ν_{bounce}	Bounce Frequency
ν_{hop}	Wheel Hop Frequency
Φ	Transfer Function Phase
$\sigma^2_{t_{err}}$	Error Variance in the DOE plan after Pooling
σ_y^2	Variance of the factor/interaction y
σ^2_{err}	Error Variance in the DOE plan
φ_y	F-Ratio of the factor/interaction y
$\varphi_{f,lim}$	F-Ratio limit for factors at chosen confidence level
$\varphi_{f,lim}$	F-Ratio limit for interactions at chosen confidence level
$c(\omega)$	Equivalent Damping of the top mount in function of frequency
c_1	Damping of the Hydraulic Top Mount Main Rubber
c_2	Damping of the Hydraulic Top Mount Secondary Rubber
c_3	Damping of the Hydraulic Top Mount Oil
c_s	Damping of the suspension strut damper
c_{damper}	Damping of the linear shock absorber in the actual suspension
d_a	Distance of strut from LCA Rotation centre

d_b	Distance of wheel from LCA Rotation centre
d_s	Spring suspension travel in the actual suspension
d_w	Wheel travel in the actual suspension
df'_{err}	Degrees of Freedom of the error after pooling
df_y	Degrees of Freedom of the factor/interaction y
df_{err}	Degrees of Freedom of the error
F'_t	Force generated by the traditional rubber top mount in frequency domain
f'_t	Force generated by the traditional rubber top mount
f_d	Force generated by the damper
F_t	Force generated by the Top Mount in frequency domain
k	Number of levels of each DOE factor
$k(\omega)$	Equivalent Stiffness of the top mount in function of frequency
k_1	Stiffness of the Hydraulic Top Mount Main Rubber
k_2	Stiffness of the Hydraulic Top Mount Secondary Rubber
k_w	Stiffness of the spring modelling the quarter car wheel
k_{spring}	Stiffness of the spring in the actual suspension
m_3	Inertia of the oil inside the inertia track
$m_{s,actual}$	Actual corner sprung mass on the suspension strut
MR	Motion Ratio
n	Number of factors in the DOE
Q'_{err}	Sum of squares of the error after pooling
Q_y	Sum of Squares of the factor/interaction y
RR	Ride Rate
u	Input Displacement of the quarter car model
v_d	Damper stem velocity
$\ddot{x}''_{s,RMS}$	Secondary Ride component of sprung mass acceleration RMS value.
$\ddot{x}''_{u,RMS}$	Secondary Ride component of unsprung mass acceleration RMS value.

$\ddot{x}'_{s,RMS}$	Primary Ride component of sprung mass acceleration RMS value.
$\ddot{x}'_{u,RMS}$	Primary Ride component of unsprung mass acceleration RMS value.
$\ddot{x}_{s,range}$	Range the Vertical Acceleration
$\ddot{x}_{s,RMS}$	Root Mean Square of the Vertical Acceleration
\ddot{x}_s	Sprung Mass Vertical Acceleration
\ddot{x}_u	Unsprung Mass Vertical Acceleration
\dot{x}'_s	Velocity of the damper stem tip
\dot{X}'_t	Rate of Displacement of the parallel system $m_3 - c_3$ in frequency domain
\dot{x}'_t	Rate of Displacement of the parallel system $m_3 - c_3$
\dot{x}_s	Sprung Mass Vertical Velocity
\dot{X}_t	Top Mount Rate of Displacement
\dot{x}_t	Top Mount Rate of Displacement
\dot{x}_u	Unsprung Mass Vertical Velocity
ν_{ref}	Reference frequency to evaluate c'_1
$f_{hydraulic}$	Force exerted by the hydraulic part of the top mount
f_t	Force Generated by the Top Mount
$k_{dyn,t}$	Dynamic Stiffness of the Hydraulic top mount
k_s	Stiffness of the spring in the quarter car model
m_s	Sprung mass of the quarter car model
m_u	Unsprung mass of the quarter car model
x'_s	Position of the damper stem tip
X'_t	Displacement of the parallel system $m_3 - c_3$ in frequency domain
x'_t	Displacement of the parallel system $m_3 - c_3$
x_s	Sprung Mass Vertical Displacement
X_t	Top Mount Displacement in frequency domain
x_t	Top Mount Displacement
x_u	Unsprung Mass Vertical Displacement

Nomenclature

ANOVA Analysis of Variances

DOE Design of Experiments

DoF Degree of Freedom

FEM Finite Element Method

FFT Fast Fourier Transform

LCA Lower Control Arm

LDE Linear Differential Equation

NVH Noise Vibration Harshness

PSD Power Spectral Density

RMS Root Mean Square

TF Transfer Function

CHAPTER 1

Introduction

The top mount in a vehicle suspension assembly connects the strut of the suspension itself to the chassis of the vehicle. This element is commonly a steel and rubber element with a visco-elastic behaviour. Throughout this project the possibility to switch to a visco-elastic hydraulic mount, comprising of two different chambers across which a fluid can travel, has been explored.

1.1 The Role of Suspension System and Top Mount

The suspension system of a vehicle fulfills many essential functions to reach the best performance in terms of handling and ride comfort. The absorption of the loads coming due to profile irregularities is one of the main task that has to be accomplished by the suspension system thanks to its elastic and damping properties, constituting a sort of filter between the road and the vehicle body [1].

Many different suspension system designs are available in the market, but all of them include different linkages to connect the wheels and the body, primary elastic members, which usually comprises of a coil spring and a shock absorber (even though different designs are available), and secondary elastic members, whose characteristics can be exploited to meet the desired comfort and handling performance [1]. The hydraulic to mount taken into account in this project belongs to this last category; it constitutes the interface between the suspension system of the vehicle and the body itself.

In Figure 1.1, the strut a McPherson suspension system is presented. On top of the shock absorber, the top mount is interfaced with the vehicle body, while on the other side it is connected to the strut [1].

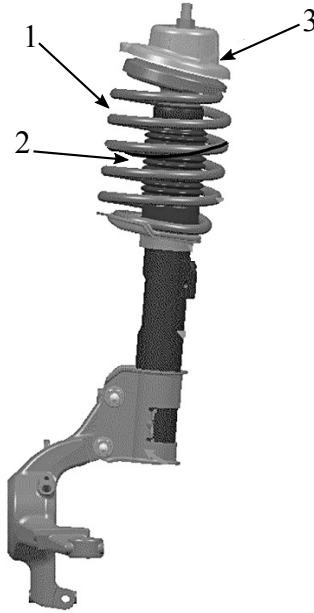


Figure 1.1: McPherson suspension strut comprising of coil spring, hydraulic shock absorber and Rubber Top Mount [1].

1.2 Rubber Mounts Structure

The most common type of top mount employed in passenger cars is elastomeric, it is composed of a steel external structure, that is filled with rubber. The task of absorbing vibration and dissipating energy is, therefore, that of the rubber; however, in many applications, the rubber alone is not able to fulfill all the damping requirements since a linear mount has a quasi linear dynamic stiffness, that obliges to a trade-off between the requirements at low frequency and those at high frequency. An improvement of the damping can be obtained by making its dynamic stiffness nonlinear, usually this task is achieved properly shaping the mount and in particular its elastomeric element: nonlinear mounts have an increased capability in meeting comfort requirements [2], [3].

In order to be able to compare the performance obtained with the hydraulic mounts, in the present project linear elastomeric mount are taken into account. This type of mounts is usually modelled by means of the “Voigt Model”, therefore, through a parallel of a damper and a spring [3]. In Figure 1.2 a 3D model of an actual elastomeric mount is presented; the section view shows the rubber inside the steel sleeve.

1.3 Hydraulic Mounts Structure

Many different types of hydraulic mounts can be found with characteristics as on their applications. Nowadays, the most common application of hydraulic mounts is as engine suspension. A 3D model of a hydraulic mount employed for engine suspension is presented



Figure 1.2: 3D model of a suspension elastomeric top mount showing the steel sleeve and its rubber insert in section [4].

in Figure 1.3. As the rubber mount, it is composed of a steel sleeve with a rubber insert, however, in this case the rubber forms two different chambers that are separated by an inertia track and sometimes also by a decoupler through which a high viscosity fluid can travel.

Figure 1.4, which shows a half-section technical drawing of the mount, allows one to better understand how a hydraulic mount works. The mount shown in Figure 1.4 comprises both an inertia track and a decoupler.

The primary rubber is very stiff and mainly acts to absorb the static load and partially provides some damping; moreover it can be seen as a pump moving the fluid to the other chamber. The secondary rubber is instead meant to accommodate the motion of the fluid and it is usually less stiff than primary one. The Inertia track and the decoupler, instead, have an important role in the damping of vibrations; the former is a spiral pipe which separates the two chambers, while the latter is a plate whose motion is limited by a sleeve and can be seen as a mechanical switch between the two chambers [6].

The inertia track is able to provide a consistent amount of damping and inertia to the fluid at high amplitude excitation for the engine mount, while the decoupler acts at low amplitude excitation: when it is not in contact with its sleeve, it offers a low resistance passage to the fluid, otherwise, at low frequencies, it is in contact with the sleeve and the fluid is obliged to pass through the inertia track. [6], [7].

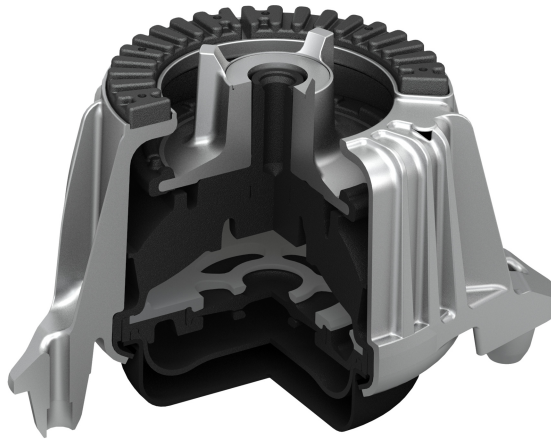


Figure 1.3: 3D Model of an actual hydraulic mount employed in engine suspension. Inertia track and decoupler are visible [5].

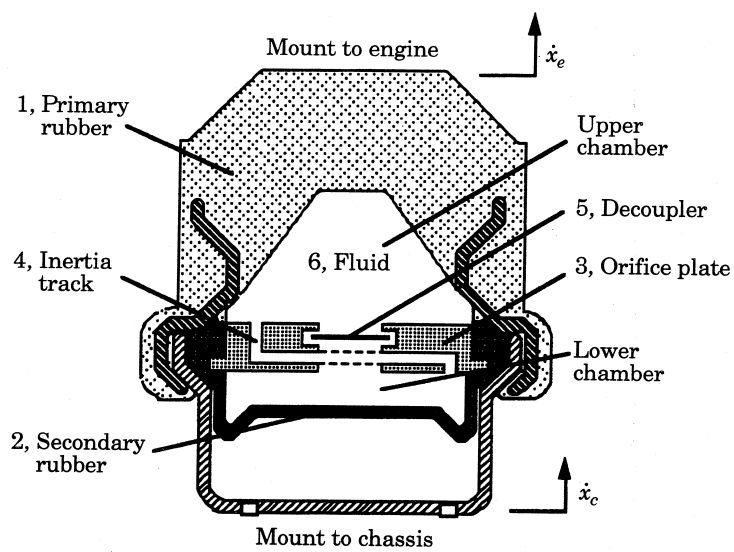


Figure 1.4: Sketch of a common hydraulic mount employed of engine suspension application [6].

1.4 Objectives of the Research

The objective of this research is to explore the potential benefits on ride comfort in terms of vertical acceleration deriving from the implementation of hydraulic top mounts in place of conventional rubber top mount. In order to accomplish this task, different mathematical models have been developed, as shown in Chapter 3. In particular, mathematical models for two type of mounts have been created and then they have been inserted as black-boxes into quarter car models to analyze and compare their influence on ride comfort. All these mathematical models have been implemented on MATLAB[®]/Simulink[®] as shown in Chapter 4, while the results of the performed simulations are given in Chapter 5.

Once each model had been created and checked, the sensitivity of ride comfort performances to the parameters constituting the model and to their interactions was explored through statistical methods like Design of Experiments (DOE) and Analysis of Variances (ANOVA) in Chapter 6. The results coming out from these analyses gave the possibility to understand the best suited dynamic stiffness shape for the ride comfort problem. Moreover, a first attempt of optimization was carried out and the solution has been proposed in Chapter 7. Finally, an unconventional arrangement for the top mount and the shock absorber was tested in order to check the possibility of obtaining further improvements. Other than the baseline mount, also the tuned hydraulic top mount has been used with this different arrangement.

CHAPTER 2

Literature Review

The main focus of this work is the improvement of the Noise Vibration Harshness (NVH) performance of a passenger vehicle by means of the substitution of a suspension assembly rubber top mount with a hydraulic one in order to gain performance in the shake and harshness frequency range.

Before the characteristics of hydraulic mounts will be analyzed, a background on vehicle ride comfort is exposed and then the influence of the suspension top mount on it will be analyzed. The application of a hydraulic mount in a suspension system has not been very widespread as the relatively scarce literature about this topic proves; however hydraulic mounts have been employed widely in powertrain suspension, so a review of the solutions adopted in this field is provided to help in the understanding of the main characteristics of these devices.

Beside the characteristics of the hydraulic mounts, the different mathematical models developed in literature are also analyzed. The peculiarity of these devices is their frequency dependent behaviour: at low frequency their dynamic stiffness is not very different from a traditional mount, since primary stiffness and damping are dominant factors; nevertheless, when the excitation frequency becomes higher, the inertia of the fluid contained into it starts to play a role and then the damping becomes very high, increasing the dynamic stiffness of the mount.

2.1 Ride Comfort Background

In the last years the problem of ride comfort is becoming more and more important for many different factors like the advance in new technologies that made customers more demanding from this point view: comfort performance of a vehicle can make the difference against market competitors.

One of the most important sources of discomfort for a passenger in a vehicle is the

unevenness of the road and the most important filter for this source of vibrations is the suspension system of the vehicle. Obviously, not only the road input has to be filtered out to improve ride comfort, but also the other source of excitation like those coming from powertrain, tires and aerodynamic noise.

All these vibration phenomena can be classified according to their frequency range, as it is exposed in [2]. According to the frequency of excitation, it is possible to discern among ride, shake, vibration, harshness and noise, from here the acronym NVH is used to address the vibration problem. The frequency ranges for each type are:

- Ride (from 0 Hz to 5 Hz): excitation due to vehicle accelerations and maneuvers
- Shake (from 5 Hz to 25 Hz): it is linked to the resonance of engine suspensions, unsprung mass or tires;
- Harshness (from 25 Hz to 100 Hz): it is due to the resonances of the vehicle body;
- Noise (more than 100 Hz): excitation sources perceived as noise.

It is also possible to define primary ride which coincides with ride mode and secondary ride which coincides with shake and part of the range of harshness.

The most common model in order to address ride comfort is the quarter car model, while a widely used physical quantity to address ride comfort problem is the vertical acceleration of the vehicle body in time and its frequency response. Quarter car models represent the corner of a vehicle, they can have different number of degrees of freedom (DoF) according to the level of details of the model itself; it is possible to insert only one mass in the model, together with main stiffness and damping of the suspension, or, as is more common, to distinguish among sprung and unsprung mass and to employ a linear spring in order to take into account the compliance of the wheel. The former model has only one DOF, while the latter has two DoF. In case of a secondary suspension system it is possible to use a three degrees of freedom model; this model is usually employed in case of body-on-frame architectures, in which a further stage of suspension is present since body and frame are not connected through rigid elements [8].

Another common model is the half car model, which is called in this way since the body is modelled as a beam; it also comprises two systems of spring and damper modelling suspensions. It is possible to have models with more than two DoF as well, which represents the base case. In case of a model with four DoF the compliance of the tire is also taken into account. When a model like this one is employed it is possible to consider heave and pitch mode in order to evaluate the ride comfort [8].

Furthermore, whenever an analysis on NVH is carried out, it is always important to not overlook the speed factor. In [9], for example, the effect of the speed on the Root Mean Acceleration Response (RMSAR) of the vehicle was analyzed through the half car model. However, if the effect of the speed was intuitive, the same does not hold for another parameter that was analyzed: the wheelbase. It was found that a higher wheelbase is able

to reduce the RMSAR of the vehicle. Therefore, NVH analysis must be carried on looking at many different parameters, although they can appear unrelated to the specific problem.

2.2 Suspension Settings

In the literature, many different studies about the optimization of suspension characteristics have been carried out in order to improve NVH performance of vehicles.

In [9] the optimization of suspension settings was also carried out. The aim of this study was the minimization of RMSAR to achieve better ride comfort performance, in particular to find the optimum values spring stiffness and viscous damping. They were found for a constant speed and using the actual road excitation as input signal. It was discovered that that higher values of the rear stiffness and damping with respect to the front ones would give a lower RMSAR.

A later work by Uys et al. is focused on the ride comfort of off-road vehicles [10]; also in this case an optimization process was applied, but the simulation was performed on a full vehicle model by means of MSC.ADAMS. The aim of this research was to find the optimum suspension settings assuring the best ride comfort at different speed and for different type of roads. The optimization process led to many important results: in fact the following items were discovered:

- When increasing the speed, lower values of front damping were needed and the same for rear damping to have a better comfort. For suspension stiffness, lower speed required lower stiffness while at higher speeds higher stiffness were necessary.
- The tuning of suspension on a particular road and speed leads is also beneficial for the same road at different speed with respect to baseline case.
- The most important setting for discomfort is the one related to rear stiffness while front damping is the least influential parameter,

It is possible to notice that different values of stiffness are needed according to the speed of the vehicle. As a result, it would be advisable to have a system able to change its stiffness according to the vehicle speed and, especially, to the excitation frequency. Therefore, there is the opportunity to replace traditional rubber top mount to enhance the ride comfort capability of modern vehicles.

2.3 Top Mount Influence

Most passenger vehicle top mounts are now made of rubber; therefore, there is no possibility to change their characteristic according to the frequency of excitation and it is not possible to use them to vary the overall stiffness and the damping of the suspension system.

The influence of this element has been studied by Kaldas et al. in two different research papers [11], [12]. Initially, they analyzed the impact of top mount characteristics on NVH performance, then they tried to optimize those parameters to get the best performance.

In the first research study, a damper top mount model was inserted into a generic quarter car vehicle model with 2 DoF and two different input signals were used; a road profile taken from IAE database and a triangle road cleat.

A nonlinear damper top mount was modelled as a parallel of a Coulomb friction element, a nonlinear spring and a series of a nonlinear damper and a linear spring. According to this model, it is characterized by frequency dependent parameters (stiffness of the linear spring K_d and damping force F_d) and amplitude parameters (stiffness of the nonlinear spring K_{e1} , K_{e2} , K_{e3} and maximum friction Force F_{frmax}). Finally, the damper mount was employed in series to the nonlinear damper of the suspension strut, therefore damper top mount and nonlinear damper had the same force applied at their nodes but a different displacement. A sketch of the quarter car model developed in the scope of that research is shown in Figure 2.1, while in Figure 2.2 a sketch of the damper top mount model is shown.

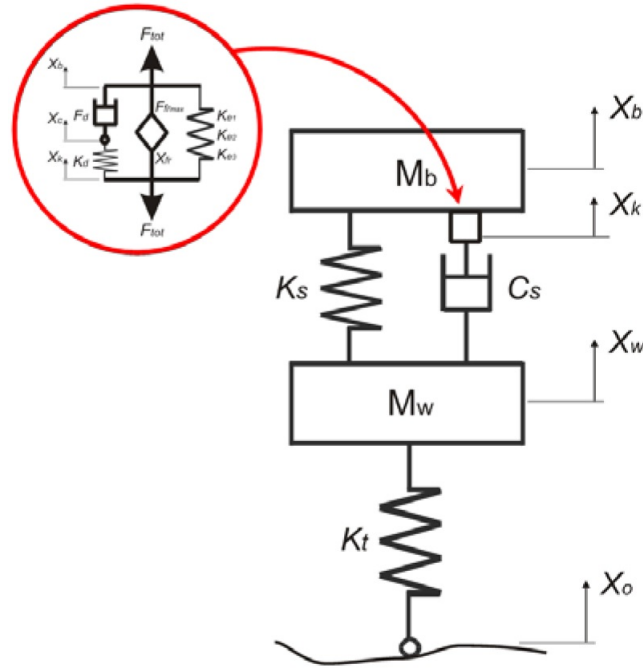


Figure 2.1: Sketch of the quarter car model used by Kaldas et al [11].

Once the model had been developed, an identification process was carried out in order to define all these parameters. The evaluation of ride comfort and harshness gave the following results:

- The increase of the spring stiffness K_{e1} in the top mount model brought significant advantages in the zone of ride comfort and shake (0 - 20 Hz), but the behaviour in the harshness frequency range was degraded with respect to lower stiffness values.

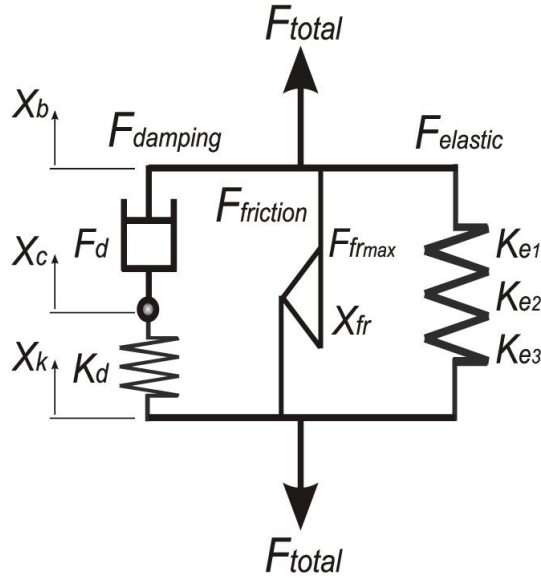


Figure 2.2: Sketch of the damper top mount model used by Kaldas et. al in their researches [11], [12].

- In relation to the variation of damping force F_d , the effect was less marked than in case of stiffness in ride comfort and shake range. In the harshness range, instead, the effect was more noticeable: a lower acceleration was obtained for a lower damping force, while a higher viscous force resulted in a decreased deformation of the damper top mount.
- By varying the maximum friction force only and maintaining fixed the other parameters a reduction of the vertical acceleration around body resonance was obtained. At the wheel resonance frequency, instead, the effect given by friction force was not noticeable.

In the second mentioned research paper, the optimization of the parameters found in the previous study was performed, in order to assure the best performance in terms of ride comfort and harshness of a vehicle.

The optimization process was carried on a quarter car vehicle model; the objective function is the linear combination of two different cost functions: the ride and harshness cost function and the impact harshness one. The former considered both ride comfort and harshness frequency ranges, the second one referred to the impact harshness characteristics. The model used was the same quarter car model used in the previous research paper. Optimization gave the following results:

- Ride comfort optimum gave a very high dynamic stiffness with respect to harshness optimum. The reference case resulted that with the lowest dynamic stiffness.
- The solution with combined optimum for both ride comfort and harshness gave a dynamic stiffness trend very close to harshness and impact harshness ones even if the weights of the optimization process were the same. This result was obtained since

only one cost function was related to ride comfort while three ones were related to harshness, this choice was driven by the fact that top mount has to deal mostly with harshness and impact harshness performances, but it was necessary to add this term to be sure that is element does not deteriorate ride comfort performance of the suspension system.

- Power Spectral Density (PSD) of body acceleration in the ride comfort, harshness, impact harshness and standard case were very close with the ride comfort one especially in the resonance part. The opposite for higher range of frequencies.

Nevertheless, all the investigated parameters resulted to have an influence on the NVH performance, in particular stiffness was found to be the most important parameter in ride comfort frequency range, while damping took the lead in harshness range.

2.4 Hydraulic Mount Modelling

In the literature, many different models for hydraulic mounts can be found: many attempts to have a reliable model for this type of devices have been made. The first attempts made to build a mathematical model dates back to 1985 in which Flower developed a linear model using masses, springs and dampers [13]. The structure of the model developed by Flower is very similar to the model analyzed by Golnaraghi et al. in [7]; however, in this last paper nonlinearities are also added to the former linear model.

The hydraulic mount taken into account in these studies had both a decoupler and an inertia track similar to the mount described in Chapter 1. For very low frequencies the static stiffness of the mount is equal to the stiffness of the upper rubber part because of the high compliance of rubber lower chamber, as the frequency rises the inertia track causes a much higher damping, causing an increase of the dynamic stiffness [7].

The sketch of a common hydraulic mount and of the lumped parameter model are presented in Figure 2.3a and Figure 2.3b. As it is shown, the mount is modelled by means of a parallel of spring and damper with stiffness k_r and damping coefficient b_r , respectively. Fluid properties are modelled through a hydraulic piston with two compliant chambers (modelled through parameters C_1 and C_2) separated by the decoupler, whose inertia and resistance are denoted by I_d and R_d , and the inertia track, which is an orifice with effective inertia I_i and resistance R_i .

Once the linear model had been developed, the nonlinear one was built step by step by adding nonlinearities to each parameter shown before. Initially, spring stiffness and damper coefficient were made dependent on frequency, amplitude and preload. The inertia parameter I_i of the inertia track was considered constant as in the experiments, while the resistance could not be constant since laminar and turbulent flows should have been considered. Therefore, resistance was split into two different components, one turbulent and one laminar, while the decoupler was treated similarly to the inertia track: it was assumed

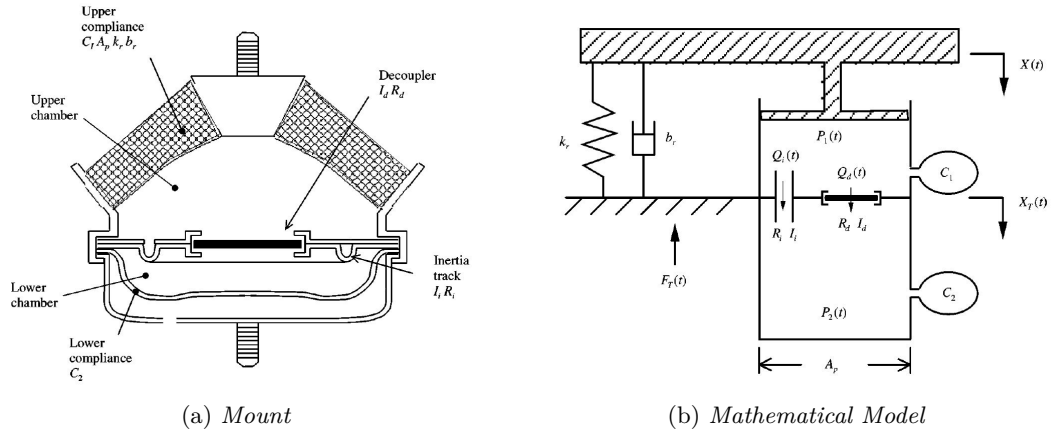


Figure 2.3: Sketch of the actual hydraulic mount (a) and of the lumped parameter model (b) for the hydraulic mount studied by Golnaraghi et al.[7]

that resistance was not constant, and that it was dependent on the flow characteristics of the fluid.

Finally, transmitted force and leak flow were also modelled. The first one was considered as dependent on the decoupler position; in fact, it was described by two different equations according to the opening or closing status of the decoupler. Moreover, the decoupler area was considered not constant but dependent on the decoupler position and pressure differential.

Leakages were taken into account, since, even though the decoupler is closed, it is always possible that a small volume of fluid passes from one chamber to the other; in order to consider this phenomenon, a variable resistance orifice, which opens only when the decoupler is in contact with the cage, was added to the model.

Decoupler volume, inertia track volume and upper chamber pressure were evaluated in function of time through simulations and then also dynamic stiffness and phase lag in frequency were evaluated in order to verify the functionality of this model. Experiments were used to verify the agreement with simulation and then its reliability.

In other two studies by Christopherson et al. [14], [15], the behaviour of hydraulic mounts was studied, at first from a mathematical point of view then with the Finite Element Method (FEM). The mathematical method was applied to both linear and nonlinear models; in both cases the differential equations were solved in the frequency domain. In particular, the models developed by two authors were similar to the ones developed in the aforementioned research studies; the important advance of this study was the application of FEM to evaluate the dynamic behaviour.

The complexity of these devices arises from the heterogeneity of materials which hydraulic mounts are made of, in fact this obliges one to use different models to characterize the single elements.

Nevertheless, results obtained with FEM were really close those obtained with mathematical method; as a result, the application of FEM is deemed as an acceptable way to

characterize the dynamic behaviour of hydraulic mounts.

As far as modelling the hydraulic mounts, there are many different studies proposing many different solutions. Even though a nonlinear model would precisely capture in a very precise way the dynamics of these devices, in this thesis, only a linear model will be employed to evaluate the benefit of the application in a suspension system of a hydraulic top mounts since this is only a very early stage of the design. Moreover, in order to simplify the problem, a hydraulic mounts without decoupler will be employed. Only the inertia track will give additional damping at relatively high frequency, but the switchable properties of the hydraulic mounts can be sacrificed in this first phases of the application study.

2.5 Applications: Engine Suspension

Hydraulic mounts are currently used in many vehicles; however their most important application is not on the main suspension system but on the engine suspension. For this reason it could be beneficial to give a look to the technologies applied in this field.

The engine is the main power source of the vehicle; it delivers torque to the driveline, thanks to the cyclic motion of the pistons. However, the crankshaft and the alternating masses exert inertia forces and centrifugal forces that are transmitted the engine block and then transferred to vehicle body. Even though the inertia forces can be compensated simply by phasing the cylinder layout in the appropriate way, a perfect balancing is not always possible and, in addition, it is necessary to consider the torque perpendicular to the axis of the crankshaft that can be generated by the same inertia and centrifugal forces.

Another source of vibration is the pressure variation in the cylinder, due to the thermodynamic cycle that each piston experiences in order to deliver power to the crankshaft. The frequency range of engine excitation depends on the number of cylinder on the rotational speed of the crankshaft, of the engine itself. A bigger engine with many cylinders has a frequency range wider than that of smaller engines [2], [16].

All automotive engines under consideration are four stroke engines, therefore there is a power stroke each two revolutions of the crankshaft. Hence, for a four cylinder, four stroke engine the excitation frequency corresponds to twice the rotational speed of the engine, i.e. for the range of speed 900 rpm to 6000 rpm, the excitation frequency ranges from 30 Hz to 200 Hz, while for a six cylinder with the same speed range, excitation frequency ranges from 45 Hz to 300 Hz. The higher the number of cylinders the higher excitation frequency range is [2].

Vibrations are then transmitted to the vehicle body through engine mounts which has a dual purpose; in fact, the role of an engine mounting system is to absorb high frequency vibrations coming from the engine, but at the same time to support the engine at low frequency in order to avoid engine vibrations. Because of this dual behaviour, the traditional rubber mounts were not capable of performing this task efficiently. Thus, the need for frequency dependent mounts capable of switching their damping capabilities

arose and led to the widespread use of hydraulic mounts, which were the focus of studies in relation to engine the suspension in the last decades [17].

At high frequencies it is desirable to have a low stiffness and damping mount at high frequency in order to absorb vibrations and high stiffness and high damping at low frequency to minimize the displacement of the engine itself. Therefore, frequency dependent characteristics of the engine mounts are necessary [3].

Moreover, the trend for front wheel drive vehicles with lightweight engines made the use of hydraulic mounts a necessity. Even though technical specifications may vary, the design of most hydraulic mounts is very similar. Nevertheless, it was found that these devices are very sensitive on design and structural parameters; the most common design in the powertrain field is the one with an inertia track and a decoupler with functionality as explained in Section 2.4 [3].

Many different research papers address the characterization of this type of mounts, with the scope of determining the frequency response and time response of the system with the engine mount but also the characterization of inertia track and decoupler. All these studies address both linear and nonlinear models and usually confirm that hydraulic mounts outperform traditional mounts.

It has been shown that in the case of engine suspension, it is convenient to have a frequency dependent damping; the amount of damping influences the transmissibility of the mount in different ways according to the frequency. The advantage of the hydraulic mount was recognized in the higher flexibility in tuning the amount of damping thanks to the hydraulic circuit; in other words, these type of mounts permit more customizable dynamic stiffness. [2].

However, passive hydraulic mounts were not able to solve all the issues linked to engine suspension, for this reason semi-active and active mounts were also developed; these mounts allow the variation of some parameters of the mounts to adapt the vehicle response, as in case of semi-active mounts, or it is possible to use an external source of energy to suppress the of the disturbance force acting on the vehicle, as in active devices.

Even though the structure of these engine mounts is very similar to those that have been studied throughout this research, there are some crucial differences that makes engine mounts unsuitable to be employed as top mounts. First of all, the range of frequencies in which they work is much wider with respect to that which top mounts are used to work with: in this last case the excitation frequency coming from the road is much lower. In this particular case, the target frequency is between 5 Hz and 30 Hz, which corresponds to the secondary ride frequency range and it is much lower than that of to engine excitation; this main difference makes it that the structure of the mount should be modified to fit in a suspension system, i. e. the decoupler can be removed in case of suspension top mount.

2.6 Hydraulic Bushings and Mounts in Different Chassis Applications

The advances made in this field are the result of many years of research, which dates back to the beginning of the 1960's as the previously discussed literature shows; contrarily, the development and the implementation of hydraulic bushings on vehicle suspension it is only at the early stages. In the following some applications of hydraulic bushings and mounts are analyzed.

Application of hydraulic mounts and bushings in the suspension system is made necessary by the requirements of NVH of the new automotive market. The technologies used for rubber mounts were reviewed by Piquet et al [18]; they analyzed the possibility to insert rubber bushings in rear axle suspensions in order to improve their handling and ride comfort capability similarly to more expensive multi-link suspensions.

Moreover, hydraulic bushings are becoming more and more important because the customer, sometimes, would like to be able to switch the behaviour of the car from luxury, comfortable riding to sport riding. For this reason, it is not possible to offer only traditional rubber bushing: there is the need to have tunable devices that allow for switching and offering the best performance in all different situations. Authors not only analyzed the possibility to insert passive hydraulic bushings but also magnetorheological bushings.

Another SAE paper by Sauer and Guy [19], analyzed the possibility to replace all the traditional suspension bushings with hydraulic passive bushings in order to improve the NVH performance of the vehicle. They individuated the following possible applications of hydraulic bushings: control arm bushing to eliminate steering wheel judder to the front wheel, sub-frame mounts, rear axle twist beam bushings and finally top mounts, even if they posed the problem of cost.

The author also presented two examples of hydro-bushings benefit on steering wheel vibration due to brake judder and tire and wheel unbalance, in case it is employed on the lower control arm. These applications however do not specifically address the top mounts, which is the primary objective of this research. This is the confirmation that this type of application is new in the suspension field.

Another application of hydraulic mounts could be the suspension of the cab of light duty trucks as analyzed in [20]. In this paper, the authors try to accurately build a model for this type of device. The model used to analyze the hydraulic mounts is shown in Figure 2.4, it is not very different from the one exposed in Figure 2.3a, but it is possible to notice that the decoupler is not present. The only element presents are the rubber parts, which are represented by the main rubber stiffness and the chamber stiffness (respectively c_r and c_b) and the orifice or inertia track, which gives the additional damping (whose area is A_k).

The equations for the model were evaluated separately for the elastomer and the fluid, and then the simulation is run on MSC.ADAMS. The results were compared with the experimental values in order to give a value to each parameter of the model. After pa-

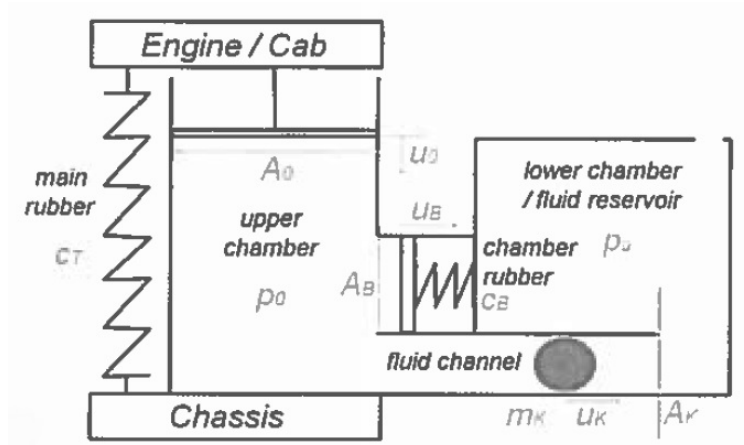


Figure 2.4: Sketch of the nonlinear model for the hydraulic mounts used in [20]

parameter identification, dynamic and static characteristics of the hydraulic mounts were analyzed through the model. The authors concluded that, in order to accurately model and simulate the behaviour of these devices, it was essential to identify amplitude and frequency dependent parameters of the mount itself.

The type of mount used in that study is close to the one that will be used in this study because of the absence of the decoupler. In fact, the lower frequencies with which the suspension top mount has to deal with makes the decoupler characteristics less important with respect to the additional damping given by the inertia track.

The literature review just developed shows the different characteristics of the hydraulic mounts and the different models that can be used in order to determine their dynamics and their most common applications in the automotive field. As it has been shown, whether the implementation of hydraulic bushings in the suspension system is becoming common, the use of hydraulic top mounts in place of traditional rubber ones is a new development area.

Therefore, the scope of this research is the analysis of the possible benefit coming from the application of a hydraulic mount as the top mount for a vehicle suspension assembly. In particular, the main focus is the improvement of the vehicle behaviour in the secondary ride frequency range. Traditional mounts lead to a compromise between the primary and secondary ride behaviour; instead, the particular characteristics of the hydraulic top mounts may improve the performance at the higher frequency range, without degrading the performance at the lowest frequency.

CHAPTER 3

Theory

In this chapter, differential equations and frequency response analysis relative to hydraulic mount model and quarter car models is presented after a short introduction about the effect of vibrations on the human body. A summary of the relevant quantities taken into account in this thesis is also included.

3.1 The Effect of Vibration on Human Body

The effect of vibrations on human body is described by ISO – 2631-1 [21], which defines methods to analyze the problem and indexes necessary to address comfort. In this norm, the Root Mean Square (RMS) values of the acceleration are considered to be the most relevant quantities to address the problem after a proper weighting of signals.

In order to evaluate the effect of vibrations on human body, many different studies have been developed. The effect of vibrations can be studied experimentally or through simulations. In the last couple of decades, several attempts have been made to develop different mathematical models. One example can be seen in the research by Muksian and Nash [22], in which a lumped was built. Then, all the different masses are connected through nonlinear springs and dampers, which model the different joints modelling the motion of a human body.

In a later work by Liang and Chiang [23], a review of the different models developed in literature was performed in a systematical way. They realized that lumped parameter models closely fit experimental data even if different applications could require different models.

Beside the attempts taken to build simulation models, there are also examples of experimental studies, like the one carried out by Demic et al.[24].

In the experimental campaigns carried out by the authors, different persons were subjected to vibrations with different frequencies and directions. Finally, the authors con-

cluded that vertical and fore – aft accelerations are the most severe for the human body. In particular, they found that human body is the most sensitive at very low frequencies and the least sensitive above 5 Hz. Instead, the human body was found to have two resonance peaks: one at around 5 Hz and the other at around 14 Hz.

Another important parameter that should always be taken into account is the time of exposure, since it highly affects the sensitivity of the human body to vibrations; this aspect is clearly visible in Figure 3.1, where different limit curves for vertical vibrations are shown according to different exposure times. It is apparent from this diagram that substantial exposure time highly impairs tolerance to vibrations.

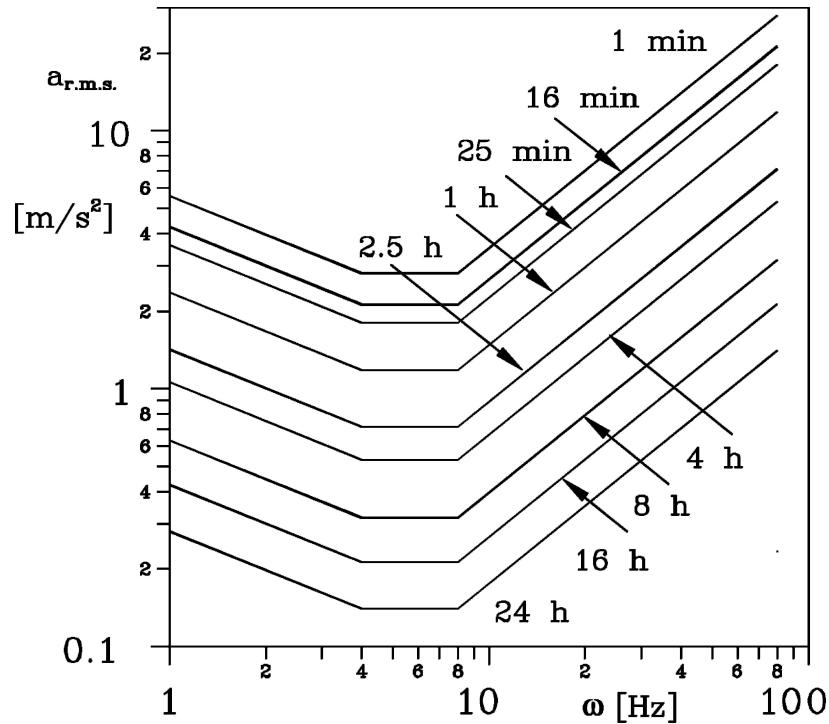


Figure 3.1: Tolerance limit curves of human body to vibrations at different exposure times according to ISO – 2631 [8].

This short summary of the human sensitivity to vibrations allows for better understanding which type of target we should pursue in the present project and also the effectiveness of the solutions proposed in this thesis.

The hydraulic mount taken into account in this study should improve the behaviour of the vehicle in the secondary ride, then for a frequency around 5 Hz and 20 Hz, a range in which, according to Figure 3.1, there is a minimum in the tolerance limit of the human body at any exposure time. Therefore, reducing at minimum the magnitude of acceleration in that frequency range, it could be possible to have a significant advantage in terms of comfort.

In addition, according to the ISO – 2631 standard, the physical quantities relative to the sprung mass are the most important parameters in comfort assessment, since they are directly felt by vehicle occupants. However, it is not possible to consider raw acceleration

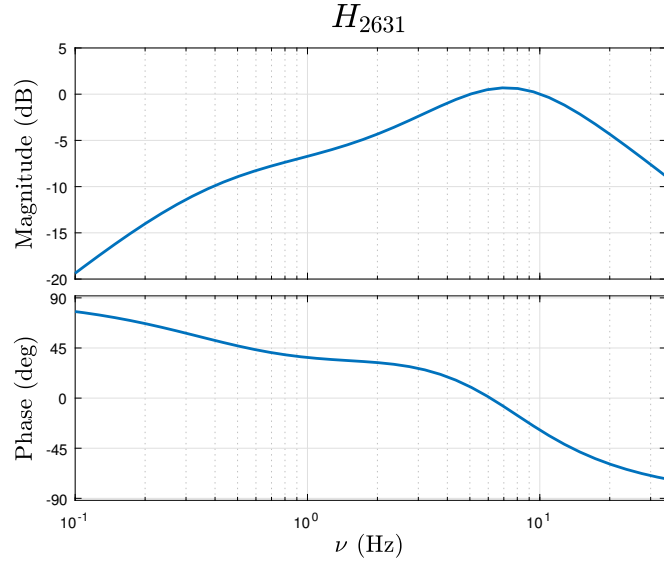


Figure 3.2: Bode plot of the transfer function H_{2631} employed to filter the data of sprung mass acceleration coming from the simulations.

values but it is necessary to evaluate a weighted acceleration in order to take into account the human sensitivity to acceleration [21]. In order to weight the acceleration, the transfer function H_{2631} shown in Equation (3.1) has to be employed to filter raw acceleration data coming from the simulations.

$$H_{2631} = \frac{80.03s^2 + 989s + 0.02108}{s^3 + 78.92s^2 + 2412s + 5614} \quad (3.1)$$

The Bode plot of the transfer function H_{2631} is presented in Figure 3.2. It is possible to notice that in this transfer function, the lowest and the highest frequencies are filtered out, while frequencies around 15 Hz are not filtered by the transfer function following the sensitivity curves shown in Figure 3.1.

3.2 Relevant Quantities for Comfort Performance

The most important quantities that measure the discomfort given due to a vehicle is the acceleration, in particular vertical acceleration, ν , since the reference model of this project is the quarter car model.

In order to compare the time histories of the quarter model after the implementation of the hydraulic mount with those of the quarter car with the traditional configuration, some short indexes have been defined like the root mean square value of the vertical sprung mass ($\ddot{x}_{s,RMS}$) and its range ($\ddot{x}_{s,range}$).

In order to evaluate results obtain in Laplace domain, instead, the transfer functions between the sprung and unsprung mass accelerations (\ddot{x}_s , \ddot{x}_u) and input displacement (u) and those between sprung and unsprung mass displacements (x_s , x_u) and input displacement will be considered.

Finally, another important figure is the road holding index η_{rh} ; its formula is shown in Equation (3.2), where k_w is the stiffness of the spring modelling the tire, u is the road displacement input, g is the gravitational acceleration, while m_s and m_u are namely sprung and unsprung mass.

$$\eta_{rh} = \frac{k_w(x_u - u)}{(m_s + m_u)g} \quad (3.2)$$

The Road Hoding Index (η_{rh}) is the ratio between the vertical force exerted by the tire and the weight of the sprung mass and unsprung mass together; therefore whether η_{rh} is equal to or higher than unity, the tire would exert a higher force than the overall weight, making the tire detach from the road [25].

3.3 Linear Models

3.3.1 Hydraulic Top Mount Mathematical Model

Linear Differential Equations

The hydraulic top mount chosen for this application can be seen in Figure 3.3; it is comprised of two chambers, which are surrounded by a primary rubber (a) and by a secondary rubber (c); primary rubber is usually stiffer than the secondary one. The two chambers are separated by an inertia track (b) providing an additional amount of damping at high excitation frequencies since high viscosity oil (d) has to travel across it when the mount is excited from the outside.

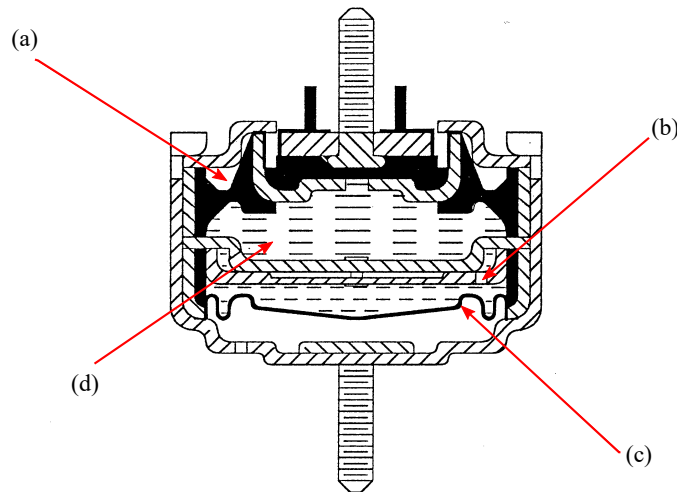


Figure 3.3: Section of the hydraulic top mount analyzed in this study [26]. (a) Primary Rubber, (b) Inertia Track, (c) Secondary Rubber, (d) Oil

The mathematical model chosen to simulate the behaviour of the hydraulic top mount is a linear model with lumped parameters. Since the application of hydraulic mounts in this field is quite new, as the literature review developed in Chapter 2 showed, we have

decided to start analyzing the characteristics of the mount with a relatively simple model and then to add nonlinearities only once the behaviour of the element had become clearer. A sketch of the lumped parameter model for the hydraulic top mount is shown in Figure 3.4.

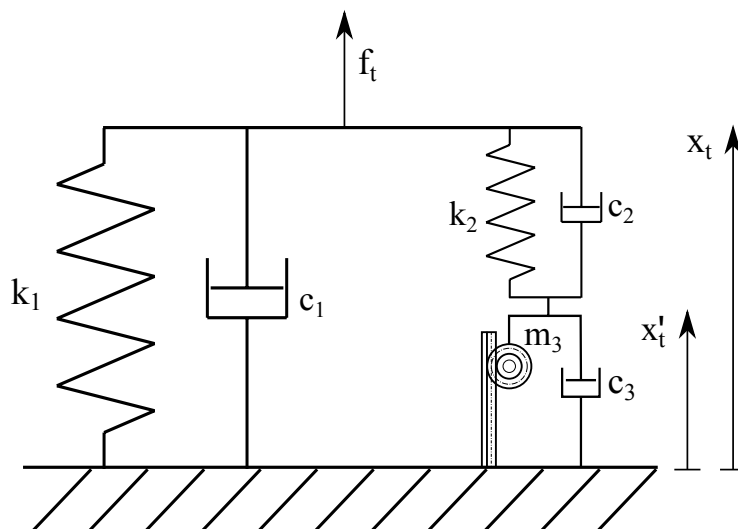


Figure 3.4: Sketch of the lumped parameter model for the hydraulic top mount.

The model comprises two different parts: on the left side there is a parallel between a spring (k_1) and a damper (c_1), which models the elastic and dissipative behaviours of the primary rubber. At low excitation frequencies, the dynamic stiffness of the mount corresponds to that of the primary rubber, while at higher frequencies, the secondary rubber and the fluid contribute to the dynamic stiffness too. The behaviour of the secondary rubber is modelled by the spring k_2 in parallel with the damper c_2 , while the fluid inside the inertia track is modelled by means of the mass (m_3) in parallel with the damper (c_3). The mass (m_3) is represented by means of a rack-pinion system to underline that it is only an object modelling the inertia of the fluid and it is not directly connected to the ground; despite this representation, it is treated as a mass in the differential equations.

In addition, it is possible to notice in Figure 3.4 that two parallel systems, modelling the secondary rubber and the hydraulic component of the mount, work in series, while the whole series system works in parallel with the primary rubber model.

The linear differential equations for the linear model with lumped parameters in Figure 3.4 were obtained manually. The starting point to accomplish this task is Equation (3.3), which links the force exerted by the mount (f_t) with the visco-elastic properties (k_1 and c_1) of the primary rubber and the hydraulic components of the mount ($f_{hydraulic}$); x_t and \dot{x}_t are, instead, the displacement and the displacement rate of the hydraulic top mount.

$$f_t = k_1 x_t + c_1 \dot{x}_t + f_{hydraulic} \quad (3.3)$$

The relation for $f_{hydraulic}$ was found by taking the series system apart from the rest

of the model and solving it. By means of this subsystem it was also possible to write the linear differential equations necessary to evaluate the displacement (x'_t), the speed (\dot{x}'_t) and the acceleration (\ddot{x}'_t) of the parallel system comprising of the mass (m_3) and the damper (c_3). The subsystem solved to obtain the relationship for $f_{hydraulic}$ is presented in Figure 3.5.

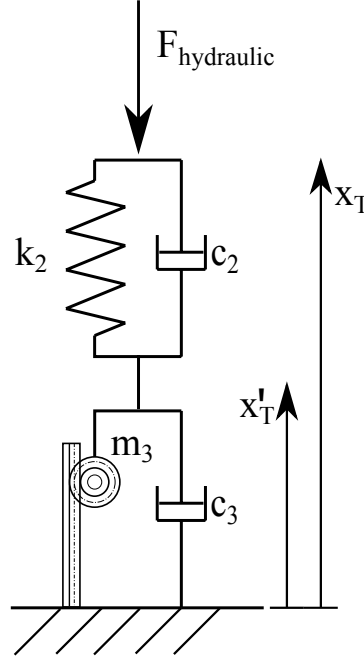


Figure 3.5: Hydraulic part of the top mount model.

The relationship between $f_{hydraulic}$, x'_t and \dot{x}'_t is shown in Equation (3.4), while in (3.5), it is possible to see the linear differential equation for x'_t which was obtained by rearranging the right-hand side of Equation (3.4).

$$f_{hydraulic} = k_2(x_t - x'_t) + c_2(\dot{x}_t - \dot{x}'_t) = m_3\ddot{x}'_t + c_3\dot{x}'_t \quad (3.4)$$

$$\ddot{x}'_t = \frac{-c_3\dot{x}'_t + k_2(x_t - x'_t) + c_2(\dot{x}_t - \dot{x}'_t)}{m_3} \quad (3.5)$$

Combining Equation (3.4) with the Equation (3.3) for f_t , it is possible to obtain Equation (3.6).

$$f_t = k_1x_t + c_1\dot{x}_t + m_3\ddot{x}'_t + c_3\dot{x}'_t \quad (3.6)$$

Transfer Function Analysis

Transfer functions were found by applying the Laplace transform to Equations (3.3) and (3.5); relations for f_t , x_t , and x'_t in Laplace domain are shown in Equations (3.7) and

(3.8), where the variables are indicated as in time domain, but with capital letters.

$$F_t = (k_1 + c_1 s)X_t + (m_3 s^2 + c_3 s)X'_t \quad (3.7)$$

$$X'_t = X_t \frac{c_2 s + k_2}{m_3 s^2 + (c_2 + c_3)s + k_2} \quad (3.8)$$

Rearranging Equations (3.7) and (3.8) it is possible to find the transfer function G between the force generated by the hydraulic top mount F_t and its displacement X_t , which is shown in Equation (3.9).

$$G = \frac{F_t}{X_t} = \frac{(c_1 s + k_1)(m_3 s^2 + (c_2 + c_3)s + k_2) + (m_3 s^2 + c_3 s)(c_2 s + k_2)}{m_3 s^2 + (c_2 + c_3)s + k_2} \quad (3.9)$$

When the velocity \dot{X}_t is considered as input, a new transfer function G_v can be defined:

$$G_v = \frac{F_t}{\dot{X}_t} = \frac{(c_1 s + k_1)(m_3 s^2 + (c_2 + c_3)s + k_2) + (m_3 s^2 + c_3 s)(c_2 s + k_2)}{s[m_3 s^2 + (c_2 + c_3)s + k_2]} \quad (3.10)$$

Once the model for the Hydraulic Mount had been developed, the same was integrated to a quarter car model in order to analyze the possible benefit with respect to a traditional suspension assembly.

3.3.2 Quarter Car Model with Hydraulic Top Mount

Linear Differential Equations

The quarter car model is a common tool used to analyze the vertical behaviour of a vehicle. For this thesis, a model with two degrees of freedom (DoFs) has been chosen; the model comprises two masses, m_u and m_s , representing the unsprung mass and the sprung mass of the vehicle, respectively. Then, the unsprung mass is connected to the road by means of the wheel which is modelled through a very rigid spring (k_w), while two masses are connected through the suspension strut and the top mount. The suspension strut is modelled by means of a spring (k_s) and a damper (c_s), while the top mount is hydraulic and works in series with the damper. Here the top mount has been considered as a “black-box”, whose model has been presented in section 3.3.1. Figure 3.6 shows a sketch of the quarter car model used in this study.

Together with the coordinates of sprung and unsprung masses (x_u , x_s), the coordinate of the damper stem tip has also been defined (x'_s), while the input of the system is indicated with u .

Linear differential equations for the quarter car model are presented in Equations (3.11) and (3.12). The equations have been obtained manually in this case as well and, similarly to what had been done for the hydraulic mount, in order to find the equation for x'_s , the

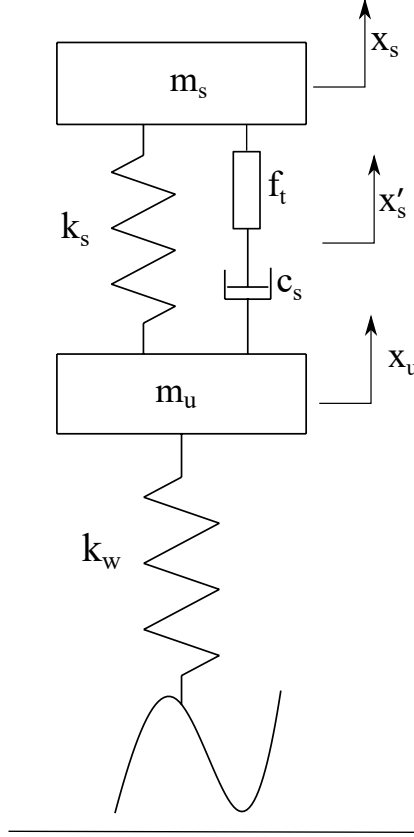


Figure 3.6: Sketch of the quarter car model integrated with the hydraulic top mount, which works in series with the damper.

series system comprising of damper and top mount was taken apart and studied separately and Equation (3.13) was obtained.

$$m_u \ddot{x}_u + k_w(x_u - u) = c_s(\dot{x}'_s - \dot{x}_u) + k_s(x_s - x_u) \quad (3.11)$$

$$m_s \ddot{x}_s + c_s(\dot{x}'_s - \dot{x}_u) + k_s(x_s - x_u) = 0 \quad (3.12)$$

$$f_t(\dot{x}'_s, \dot{x}_s, \dot{x}'_s, x_s) = c_s(\dot{x}'_s - \dot{x}_u) \quad (3.13)$$

In Equations (3.14), (3.15) and (3.16) the linear differential equations above have been rearranged in order to make them suited for the implementation on Simulink®.

$$\ddot{x}_u = -\frac{k_w}{m_u}(x_u - u) + \frac{c_s}{m_u}(\dot{x}'_s - \dot{x}_u) + \frac{k_s}{m_u}(x_s - x_u) \quad (3.14)$$

$$\ddot{x}_s = -\frac{c_s}{m_s}(\dot{x}'_s - \dot{x}_u) + \frac{k_s}{m_s}(x_s - x_u) \quad (3.15)$$

$$\dot{x}'_s = \frac{f_t(\dot{x}'_s, \dot{x}_s, x'_s, x_s)}{c_s} + \dot{x}_u \quad (3.16)$$

Transfer Function analysis

Transfer functions for Equations (3.11), (3.12) and (3.13) were obtained by means of Laplace transform as they were for the Hydraulic Top Mounts equations in Section 3.3.1.

In order to proceed with the analysis of frequency response, it is worth noting that the hydraulic top mount is subjected to the relative displacement between the sprung mass and the tip of the damper stem ($x_s - x'_s$), when inserted in the quarter car model; therefore, the relation between the force F_t and the input displacement, in Laplace domain, becomes:

$$F_t = GX_s - GX'_s \quad (3.17)$$

When the velocity ($\dot{x}_s - \dot{x}'_s$) is considered, it is possible to obtain:

$$F_t = G_v \dot{X}_s - G_v \dot{X}'_s \quad (3.18)$$

Transforming all equations in Laplace domain, it is possible to obtain the following transfer functions: $H = \frac{X_u}{X_s}$, $I = \frac{X_s}{U}$, $J = \frac{\ddot{X}_s}{U}$, $K = \frac{X_u}{U}$ and $L = \frac{\ddot{X}_u}{U}$.

The expressions for H , J , K and L are shown in Equations (3.19), (3.20), (3.21), (3.22) and (3.23). It is possible to notice that, since the hydraulic mount has been treated as a black-box, its effect on the transfer functions is only determined by its transfer function G .

$$H = \frac{(c_s s + G)(m_s s^2 + k_s) + c_s G s}{(c_s s + k_s)(c_s s + G) - c_s^2 s^2} \quad (3.19)$$

$$I = \frac{(c_s s + G)k_w}{(c_s s + G)(m_u s^2 + c_s s + k_w + k_s)H - (c_s s + G)k_s - c_s G s - c_s^2 H s^2} \quad (3.20)$$

$$J = s^2 I \quad (3.21)$$

$$K = I \cdot H \quad (3.22)$$

$$L = s^2 K \quad (3.23)$$

3.3.3 Traditional Rubber top Mount

Linear Differential Equations

The traditional linear rubber mount was modelled through a linear spring and a linear damper in parallel. A sketch for this top mount model is shown in Figure 3.7.

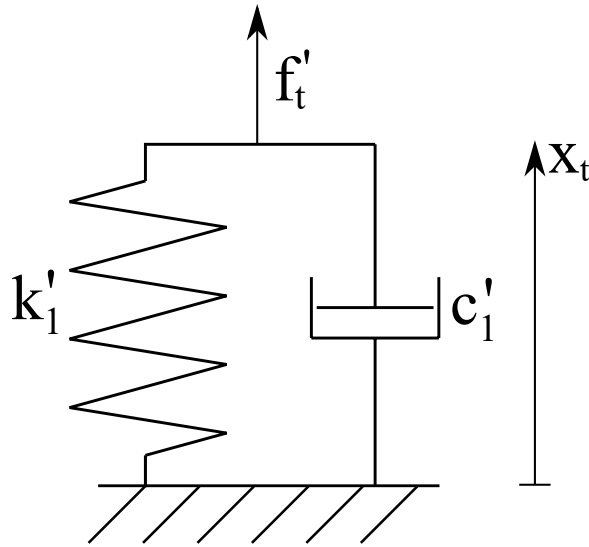


Figure 3.7: Sketch of the model employed for the traditional rubber top mount.

The relationship between the force generated by this mount (f'_t) is quite straightforward and it is shown in Equation (3.24).

$$f'_t = k'_1 x_t + c'_1 \dot{x}_t \quad (3.24)$$

Transfer Function Analysis

The simplicity of the model also leads to a very simple transfer function (G'), which was obtained, as usual, by applying the Laplace Transform to the corresponding linear differential equation. The result is shown in (3.25).

$$G' = \frac{F'_t}{X_t} = k_1 + c_1 s \quad (3.25)$$

When the first derivative of the displacement is considered as input, it is possible to obtain Equation (3.26).

$$G'_v = \frac{F'_t}{\dot{X}_t} = \frac{k_1 + c_1 s}{s} \quad (3.26)$$

3.3.4 Quarter Car Model with Traditional Top Mount

Linear Differential Equations

A quarter car model with the traditional rubber top mount model was developed in order to have a reference baseline for the evaluation of the results obtained using the set-up with the hydraulic mount.

As in case of the hydraulic top mount, the rubber top mount has also been inserted in series with the suspension damper. A sketch of the quarter car model integrated with a traditional rubber mount is shown in Figure 3.8.

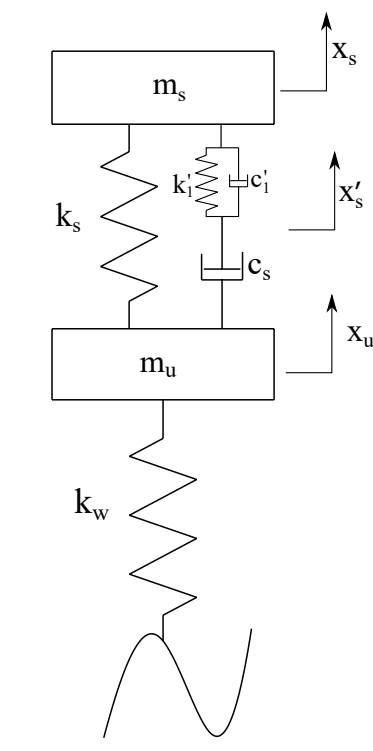


Figure 3.8: Sketch of the quarter car model with a traditional rubber mount in series to the suspension damper.

Linear differential equations for sprung and unsprung mass in this configuration are the same as those shown in Section 3.3.2, namely in Equations (3.11) and (3.12)

The only equation that is affected by the different configuration is the one relative to the subsystem damper – top mount, which is shown in (3.27).

$$k_1(x_s - x'_s) + c_1(\dot{x}_s - \dot{x}'_s) = c_s(\dot{x}'_s - \dot{x}_u) \quad (3.27)$$

Although the equations relative to this configuration of quarter car are more manageable than the ones relative to the configuration shown in Section 3.3.2, it is convenient to use the same procedure used for that model, in other words considering the top mount as a black-box only affecting the model through its own transfer function. In this way,

Equation (3.27) reduces to Equation (3.28), similarly to Equation (3.13).

$$f'_t(\dot{x}'_s, \dot{x}_s, x'_s, x_s) = c_s(\dot{x}'_s - \dot{x}_s) \quad (3.28)$$

Transfer Function Analysis

Since the top mount model has been treated as a black-box, the transfer functions H' , I' , J' , K' and L' for this model do not differ from those relative to the model with the hydraulic top mount: only transfer function G' has a different formulation, as shown in Section 3.3.3, because of the different type of mount employed.

All the transfer functions are shown in Equations (3.29), (3.30), (3.31), (3.32) and (3.33).

$$H' = \frac{(c_s s + G')(m_s s^2 + k_s) + c_s G' s}{(c_s s + k_s)(c_s s + G') - c_s^2 s^2} \quad (3.29)$$

$$I' = \frac{(c_s s + G')k_w}{(c_s s + G')(m_u s^2 + c_s s + k_w + k_s)H - (c_s s + G')k_s - c_s G' s - c_s^2 H s^2} \quad (3.30)$$

$$J' = s^2 I' \quad (3.31)$$

$$K' = I' \cdot H' \quad (3.32)$$

$$L' = s^2 K' \quad (3.33)$$

3.4 Nonlinear Models

Beside the linear quarter car models, nonlinear models were created for both configurations with a hydraulic top mount and with a rubber top mount. The nonlinearity of these models lies on the shock absorber: in nonlinear models it is not modelled through a single parameter c_s , but through a map which gives a value of force for each value of speed. Since the model is nonlinear, it was not possible to represent the transfer functions of the model formulaically, which has been numerically estimated from the time simulation by means of MATLAB.

3.4.1 Quarter Car Model with Hydraulic Top Mount

In Figure 3.9 it is possible to appreciate a sketch of the nonlinear quarter car model with the hydraulic top mount in which the damper c_s has been replaced with a generic device generating the force f_d given a certain velocity input.

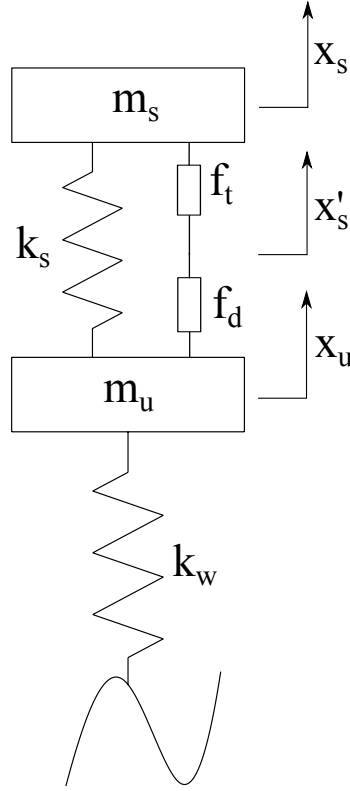


Figure 3.9: Sketch of the nonlinear quarter car model with the hydraulic top mount.

In Equations (3.34), (3.35) and (3.36), differential equations relative to the nonlinear quarter car model are shown. It is clear that the equations are the same as those written for the linear model except for the force exerted by the damper, which is written in closed form.

$$m_u \ddot{x}_u + k_w(x_u - u) = k_s(x'_s - x_u) + f_d(\dot{x}'_s, \dot{x}_u) \quad (3.34)$$

$$m_s \ddot{x}_s + k_s(x'_s - x_u) + f_t(\dot{x}'_s, \dot{x}_u) = 0 \quad (3.35)$$

$$f_t(\dot{x}'_s, \dot{x}_s, \dot{x}'_s, x_s) = f_d(\dot{x}'_s, \dot{x}_u) \quad (3.36)$$

3.4.2 Quarter Car Model with Rubber Top Mount

Figure 3.10 presents a sketch of the nonlinear quarter car model; as above, the only difference with the linear model is represented by the shock absorber.

Differential equations for sprung and unsprung mass are the same as the equations obtained for the configuration with the hydraulic top mount in Equations (3.34), (3.35), with the exception of the equation relative to the series comprising of the shock absorber and the rubber mount. This equation differs because of the relation to evaluate the force

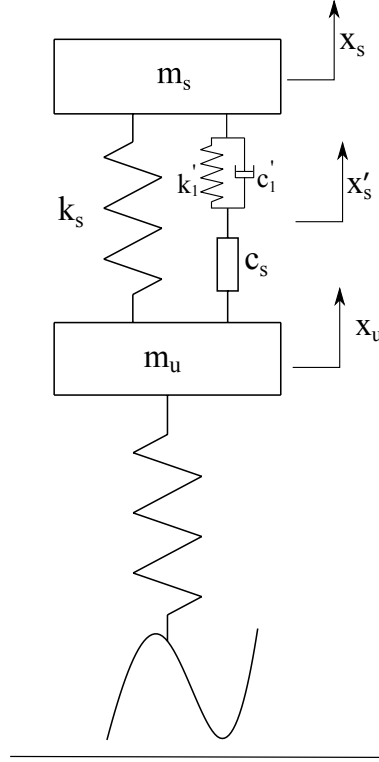


Figure 3.10: Sketch of the nonlinear quarter car model with the rubber top mount.

exerted by the top mount which, in this case, is $f_t(\ddot{x}'_s, \ddot{x}_s, x'_s, x_s)$. This last equation is reported in (3.37).

$$f_t(\ddot{x}'_s, \ddot{x}_s, x'_s, x_s) = f_d(\dot{x}'_s, \dot{x}_u) \quad (3.37)$$

3.4.3 A Different Arrangement for the Hydraulic Top Mount

Together with the traditional arrangement for the hydraulic top mount, a quarter car model with the hydraulic top mount in series with the spring and the nonlinear shock absorber was created. A sketch of the quarter car model in this configuration is presented in Figure 3.11. The equations relative to sprung and unsprung mass are similar to those seen in previous sections, while the equation relative to the series element differs from the equation for the normal configuration since the spring (k_s) is included in it as well.

In Equations (3.41), (3.42) and (3.40), differential equations relative to the new configuration of the model are shown.

$$m_u \ddot{x}_u + k_w(x_u - u) = k_s(x'_s - x_u) + f_d(\dot{x}'_s, \dot{x}_u) \quad (3.38)$$

$$m_s \ddot{x}_s + f_t(\dot{x}'_s, \dot{x}_s, x'_s, x_s) = 0 \quad (3.39)$$

$$f_t(\dot{x}'_s, \dot{x}_s, x'_s, x_s) = k_s(x'_s - x_u) + f_d(\dot{x}'_s, \dot{x}_u) \quad (3.40)$$

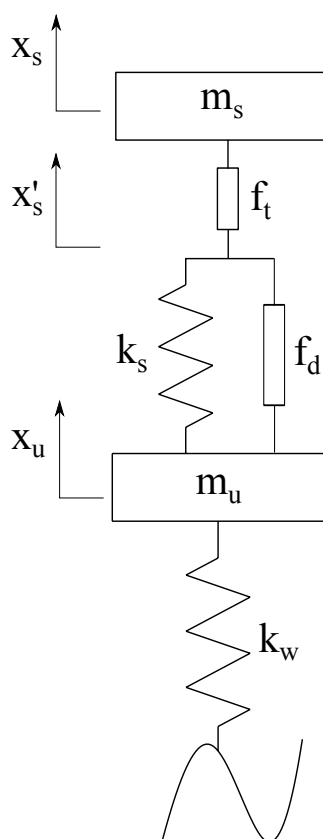


Figure 3.11: Sketch of the quarter car model with the hydraulic top mount in series with the whole suspension strut.

Similarly to the standard configuration case, it is possible to rewrite the equations relative to the sprung and unsprung mass in order to ease the transposition on Simulink[®], as shown in Equations (3.41) and (3.42).

$$\ddot{x}_u = -\frac{k_w}{m_u}(x_u - u) + \frac{k_s}{m_u}(x'_s - x_u) + \frac{f_d(\ddot{x}'_s, \ddot{x}_u)}{m_u} \quad (3.41)$$

$$m_s \ddot{x}_s = -\frac{f'_t(\dot{x}'_s, \dot{x}_s, x'_s, x_s)}{m_s} \quad (3.42)$$

Since the system is nonlinear, it is not possible to obtain represent the transfer functions of the system formulaically, which has been estimated in a numerical way starting from the results of the time simulation.

Differential equations and transfer functions shown in this chapter were used in order to build Simulink[®] models relative to top mounts and quarter car models and to analyze the frequency response of the systems by means of MATLAB[®]. The different steps taken to build various simulation models are presented in Chapter 4, while the results of the simulations are shown in Chapter 5.

CHAPTER 4

Simulation Models

In this chapter the development of simulation models, necessary to evaluate the benefits introduced by the hydraulic top mount implementation, is reported. The models have been built using the equations described in Chapter 3. In particular, two different Simulink[®] models were built for the two different top mounts, then they were combined together with linear and nonlinear quarter car models.

In addition, a MATLAB[®] code was developed in order to evaluate the frequency response of each system and to compare theoretical transfer functions with those estimated starting from Simulink[®] linear models. This step was not feasible for nonlinear models, since a general solution in Laplace domain is not available for these systems and the frequency response was estimated starting from time simulations.

4.1 Simulink[®] Models

4.1.1 Linear Model for the Hydraulic Top Mount

The diagram block for the hydraulic mount built with Simulink[®] is shown in Figure 4.1, the input of the model is represented by the displacement (x_t), while its output is the force f_t generated by the top mount.

The subsystem present in the block is meant to solve the linear differential equations relative to the series composed by the parallel damper (c_2) and spring (k_2) and the parallel mass (m_3) and damper (c_3). The block diagram relative to the subsystem is shown in Figure 4.2; in this case, the inputs are the same as the main system, while the outputs of the system are the displacement and the velocity of the parallel system composed of m_3 and c_3 (x'_t and \dot{x}'_t).

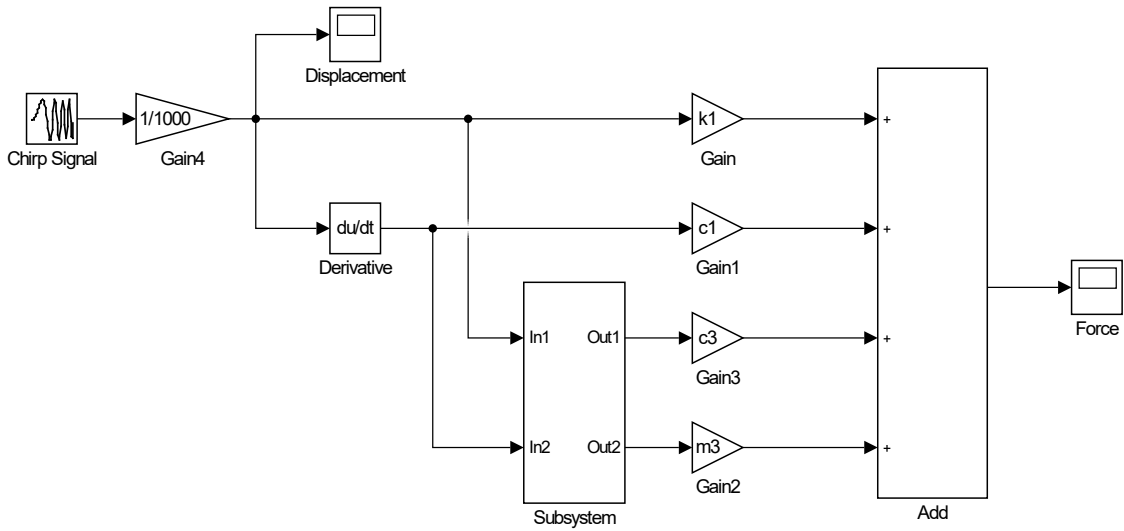


Figure 4.1: Block diagram for the main system of the hydraulic top mount.

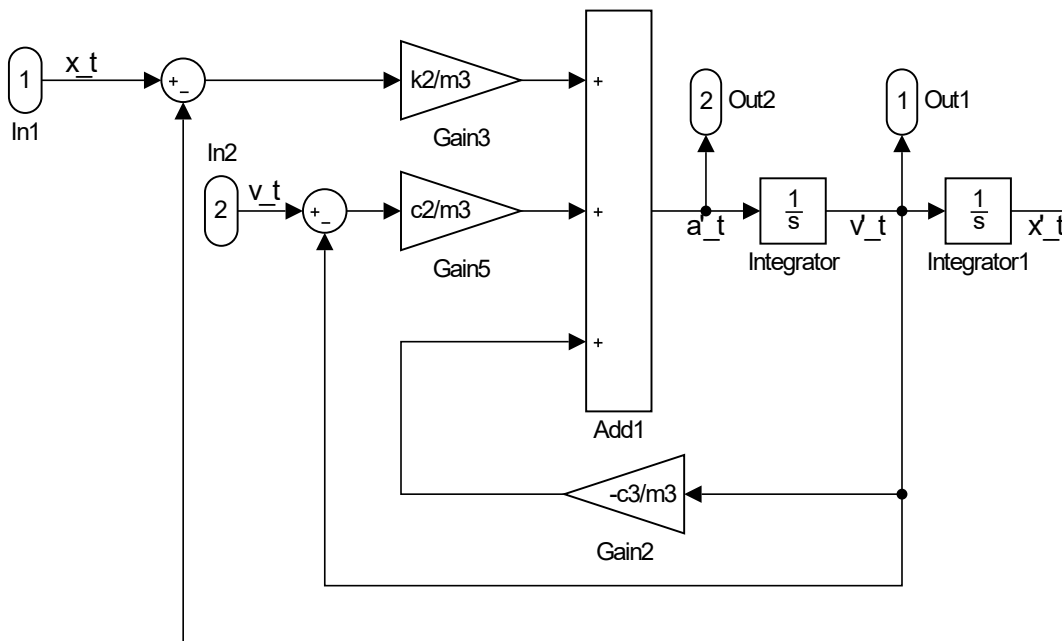


Figure 4.2: Block diagram for the subsystem for the hydraulic mount.

4.1.2 Linear Model for the Rubber Top Mount

Beside the model for the hydraulic mount, a linear model for the rubber top mount was also built in order to have a reference to assess the characteristics of the hydraulic top mount. As it has discussed in Chapter 3, the linear differential equations for this module are quite simple, therefore its Simulink[®] model is likewise simple.

The block diagram for the rubber mount is shown in Figure 4.3. Similar to the block diagram for the hydraulic top mount, the input signals are the displacement (x_t) and the

speed (\dot{x}_t), while the output is the force exerted by the mount (f'_t). The main difference between the models for the two mounts is the absence of the subsystem representing the hydraulic component and the secondary rubber.

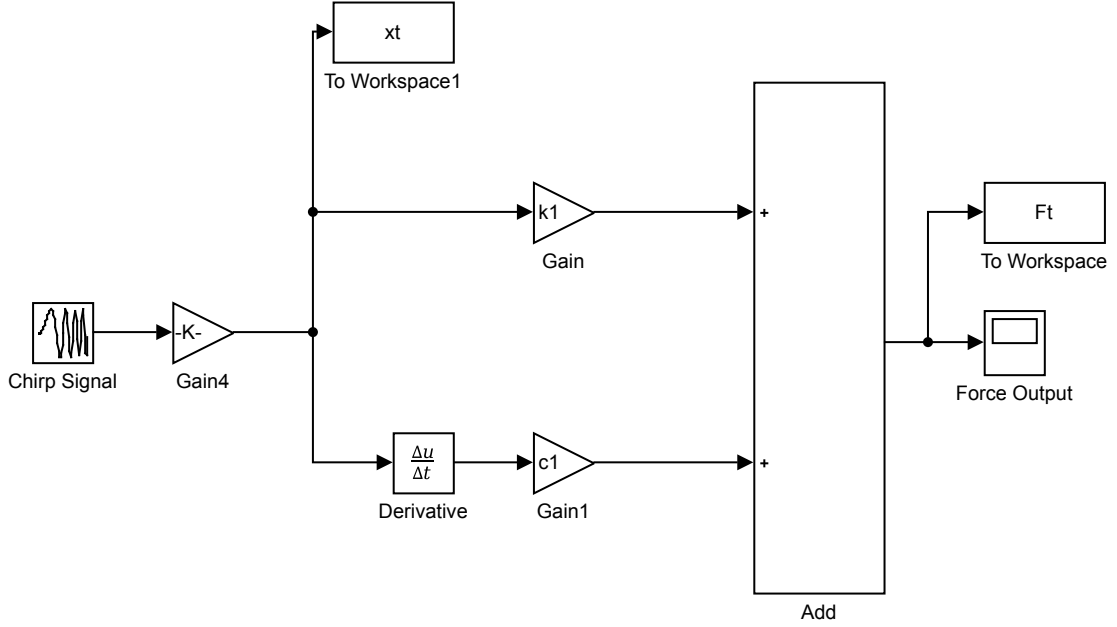


Figure 4.3: Block diagram for the rubber top mount model.

4.1.3 Simulink® Linear Quarter car Model with the Hydraulic Top Mount

The numerical linear model for the quarter car model with the hydraulic top mount has been built according to the Equations (3.14) and (3.15). The block diagram can be seen in Figures 4.4 and 4.5; the former shows the main system, which solves the equations relative to sprung mass and unsprung mass, while the latter shows the subsystem leading to the solution of the equations for the series composed by the suspension damper and the hydraulic mount.

It is important to note that the subsystem was not built following Equation 3.16: in that case an algebraic loop would have been generated since the force exerted by the hydraulic mount directly depends on the velocity of the damper stem tip. Therefore, to avoid modifying the equations relative to the hydraulic top mount, the block diagram was built along with the frequency domain equation relating the damper stem tip, the sprung mass and unsprung mass velocities (\dot{X}'_s , \dot{X}_s and \dot{X}_u), respectively through the top mount transfer function (G_v) and the damping coefficient (c_s) as Equation (4.1) shows.

$$\dot{X}'_s = \frac{G_v}{G_v + c_s} \dot{X}_s + \frac{c_s}{G_v + c_s} \dot{X}_u \quad (4.1)$$

To run the simulation, a chirp signal was chosen as input, as it is shown in Figure 4.4. The upper part of the block diagram for the main system (Figure 4.4) is meant to solve

Equation (3.14) relative to the unsprung mass, while the blocks in the lower part lead to the solution of Equation (3.12) relative to the sprung mass. Both parts of the system employ the output of the subsystem (\dot{x}'_s), to solve the equations; the inputs of the subsystem are, instead, the unsprung mass velocity (\dot{x}_u) and the sprung mass velocity (\dot{x}_s).

4.1.4 Simulink[®] Nonlinear Quarter car Model with the Hydraulic Top Mount

Once the linear model was built, the linear damper of the strut has been replaced with a nonlinear one; in other words, the force exerted by the damper and the speed of the damper stem are no longer related by a constant parameter c_s , but rather by a damping coefficient dependent on the speed of the damper stem.

The difference in the block diagram of the main system is given by the lookup table block that replaces the gain block c_s , while the block diagram of the subsystem was radically changed: since the system is not linear, it was not possible to write its differential equations in Laplace domain.

Therefore, Equation 4.2 was used to develop the model in Simulink.

$$\dot{X}'_s = \dot{X}_s - \frac{F_d}{G_v} \quad (4.2)$$

The block diagram for the main system and the subsystem are shown in Figures 4.6 and 4.7.

4.1.5 Quarter car models with traditional mount

The block diagram for the quarter car model with the traditional rubber mount appears to be the same as the diagram for the quarter car model with the hydraulic top mount. The main difference between the two lies in the transfer function of the top mount whose expression is shown in Equation (3.26).

Apart from the transfer function of the top mount, block diagrams for linear and nonlinear quarter car models with the traditional rubber top mount do not differ from those shown in Figures 4.4, 4.5, 4.6 and 4.7.

4.2 Simulink[®] Nonlinear Quarter car Model with the Hydraulic Top Mount in Series with the Strut

As shown, the last model that was built contains a hydraulic mount, but in a different position: it has been placed in series with the whole suspension strut. In Figures 4.8 and 4.9, the Simulink[®] model leading to the solution of sprung and unsprung mass equations and the subsystem for the solution of the system in series are shown.

The two models reflect the equations reported in Chapter 3, with the subsystem that is more complex because of the presence of the spring k_s inside the series subsystem, while

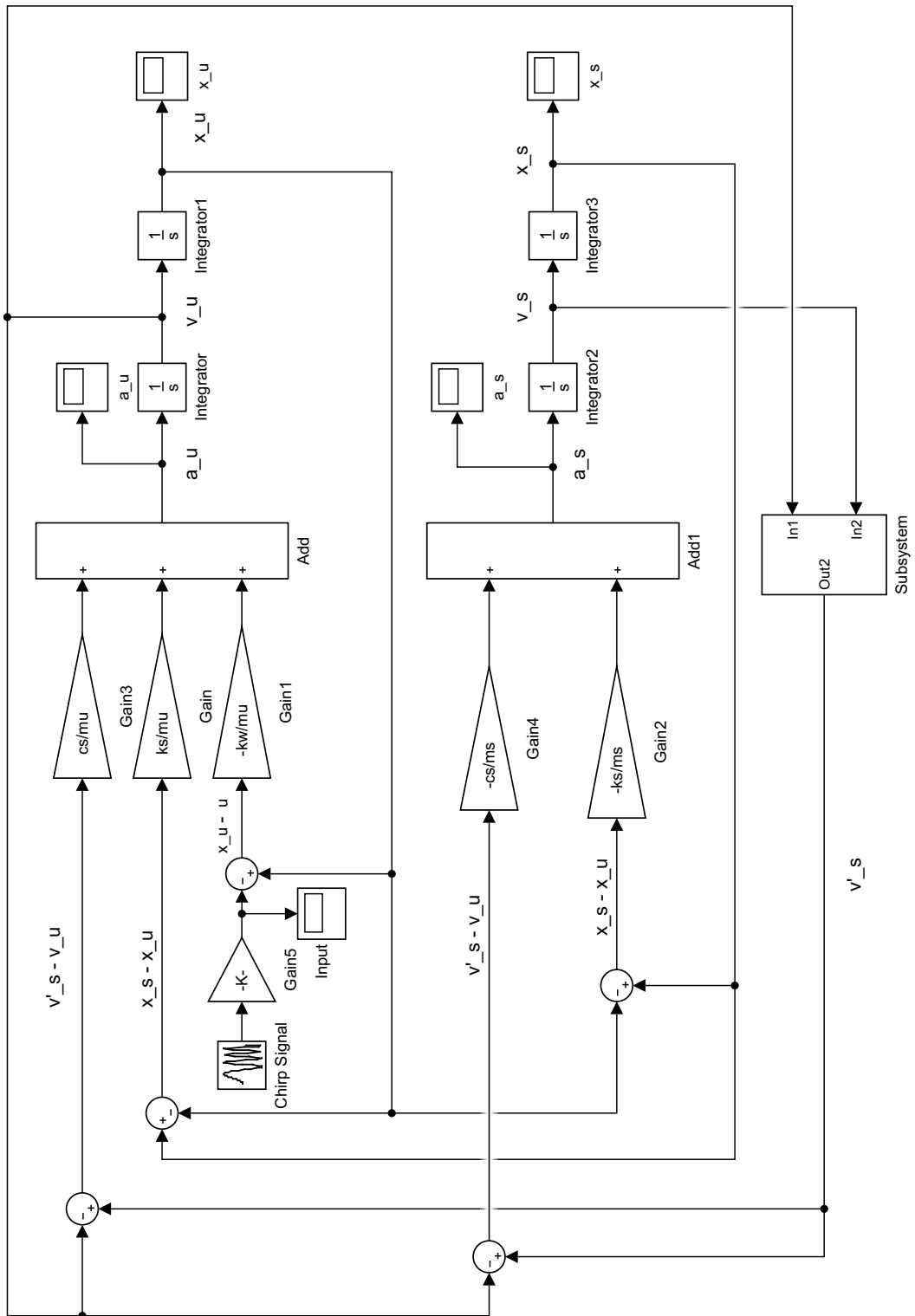


Figure 4.4: Block diagram for the quarter car model with the hydraulic top mount built with Simulink®.

the main system for the sprung and unsprung mass equation is similar to models created for the standard configuration, although it was created to solve the sprung mass equation

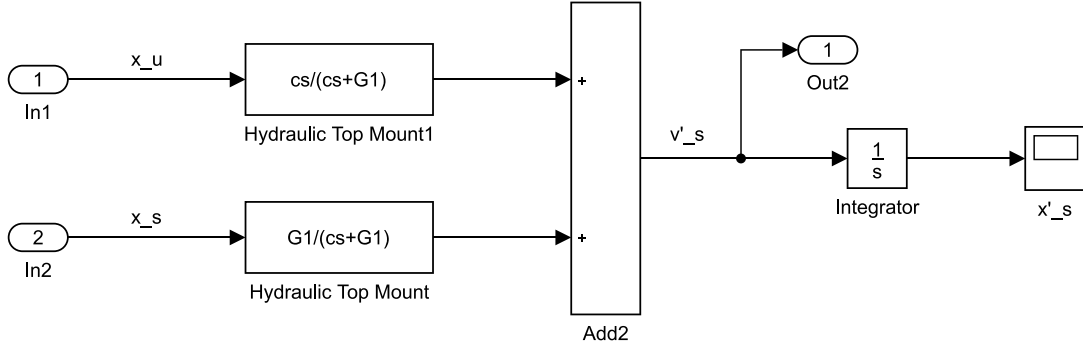


Figure 4.5: Block diagram for the subsystem composed by the series of damper and hydraulic mount in quarter car model built with Simulink®.

by means of the top mount force only.

4.3 Choice of Model Parameters

4.3.1 Rubber and Hydraulic Top Mounts

The parameters for the hydraulic top mount necessary to run the simulation were chosen starting from the parameters for a normal bushing: it has been assumed that the main rubber stiffness and dissipative behaviour of the primary rubber were the same as a traditional rubber top mount.

The values for the other parameters were initially hypothesized with the purpose of finding optimal values once the model were validated. A typical value used for the (k_1) stiffness of rubber top mounts is 800 N/mm, while the damping is usually chosen in relation to the desired phase at the desired frequency (ν_{ref}), which corresponds to the frequency of the vibrations that should be damped by the implementation of the hydraulic top mount – in other words, the wheel hop frequency of the quarter car model. The procedure to evaluate this frequency is shown in Appendix B and, according to the data shown in section 4.3.2, it is equal to 10.2 Hz.

A phase value of 5° was chosen for the phase at the aforementioned frequency. The formula for the evaluation of damping (c_1) is reported in Equation 4.3).

$$c_1 = \frac{K_{dyn}}{2\pi\nu_{ref}} \sin(\Phi_{K_{dyn}}) \quad (4.3)$$

The two parameters for the rubber mount have been set equal to the main rubber stiffness and dissipative behaviour of the hydraulic mount in order to have comparable results between the two different models. Therefore, the stiffness of the rubber mount k'_1 coincides with the dynamic stiffness amplitude of the hydraulic top mount in ride frequency range (0 – 5 Hz), while the damping value is set according to the desired value

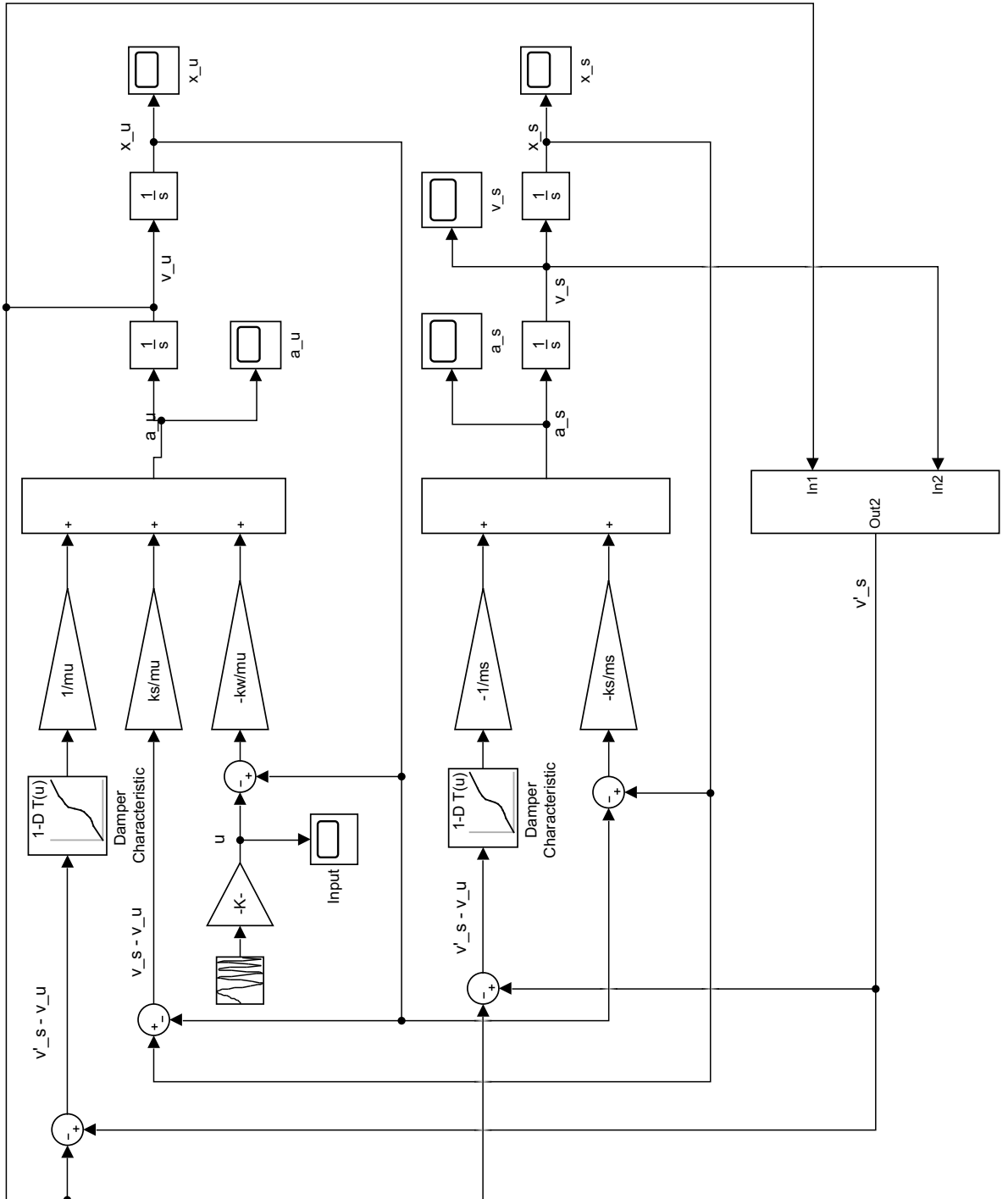


Figure 4.6: Block diagram for the nonlinear quarter car model with the hydraulic top mount built with Simulink®.

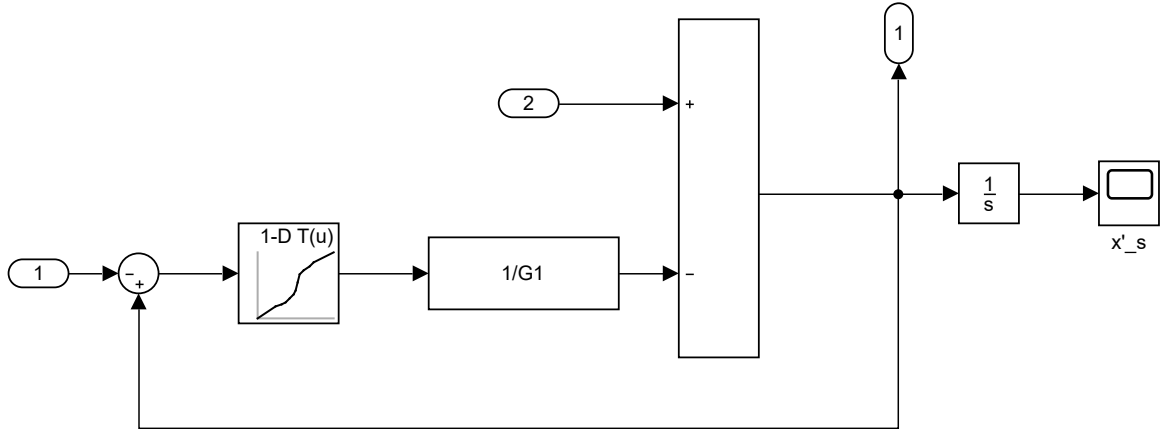


Figure 4.7: Block diagram for the subsystem of the nonlinear quarter car model with the hydraulic top mount.

of the dynamic stiffness phase. The values for the rubber top mount and the hydraulic top mount are shown in Table 4.1.

Table 4.1: Values of the parameters for the hydraulic top mount model.

Rubber Top Mount		Hydraulic Top Mount					
k'_1	c'_1	k_1	c_1	k_2	c_2	c_3	m_3
(N/mm)	(Ns/mm)	(N/mm)	(Ns/mm)	(N/mm)	(Ns/mm)	(N/mm)	(kg)
800	2.18	800	2.18	200	0.2	1.2	10

4.3.2 Linear Quarter Car Models

The values for the linear quarter car model were defined starting from the parameters for an actual suspension system. However, when considering a quarter car, it is not possible to use raw component values, rather it is necessary to transport their characteristics to the centre of the wheel. The value of stiffness and damping for the suspension assembly analyzed and the sprung mass are listed in Table 4.2.

In an actual suspension system, spring, damper, top mount and sprung mass are not placed exactly on top of the wheel like in the simplified quarter car model; therefore, the forces acting on these elements and also the value of the “sprung mass” seen by the strut in the actual configuration are different from the values in the simple configuration of the quarter car model.

In order to have reasonable data in the quarter car model and to transport all the

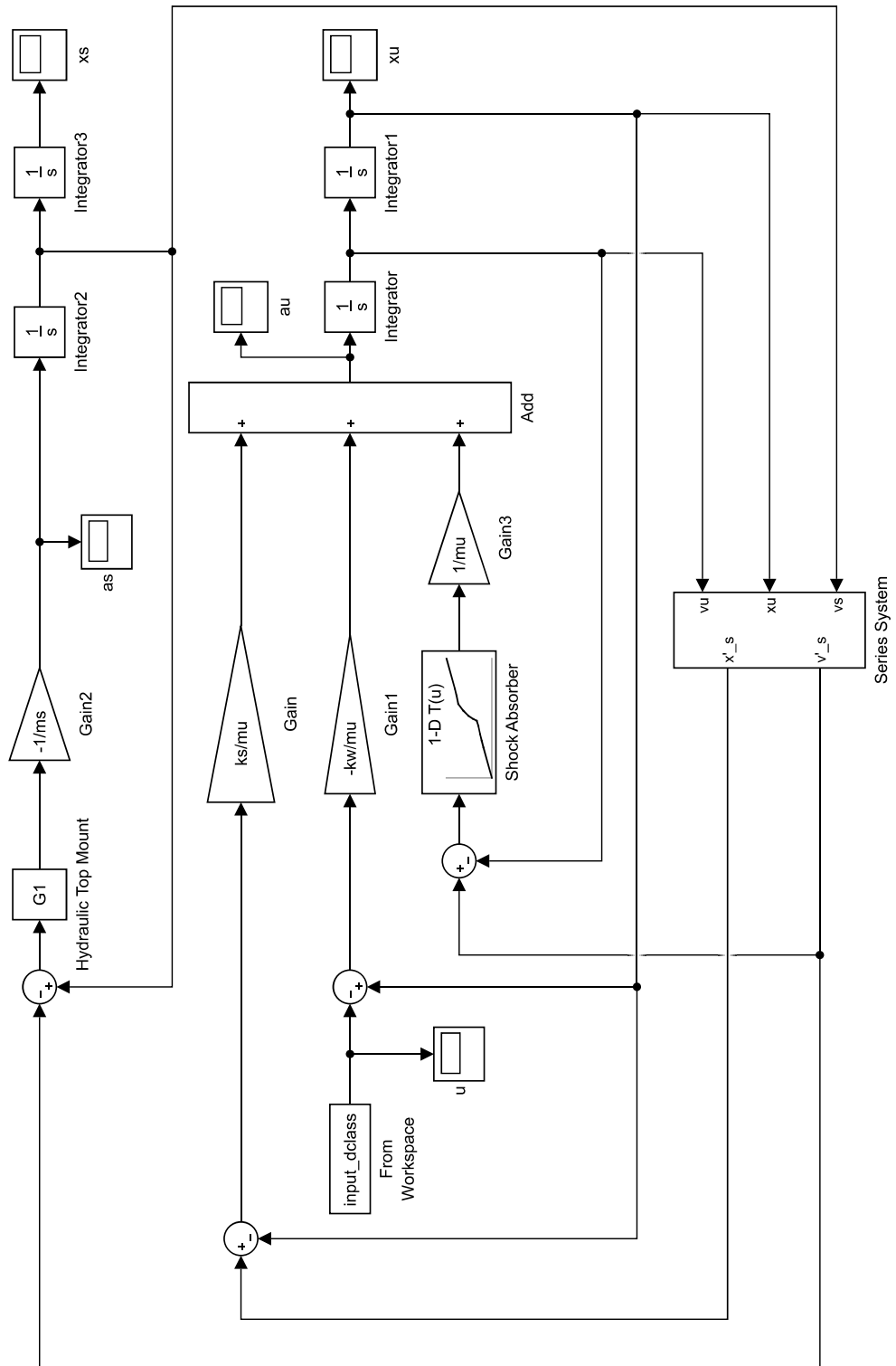


Figure 4.8: Block diagram for the nonlinear quarter car model with the hydraulic top mount in series with the strut.

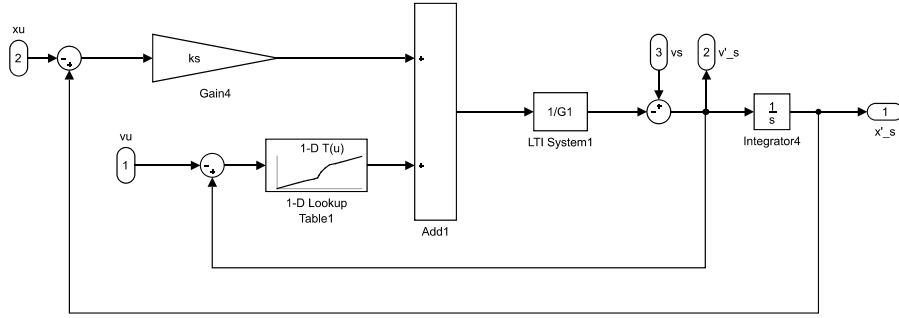


Figure 4.9: Block diagram for the subsystem of the nonlinear quarter car model with the hydraulic top mount in series with the strut.

Table 4.2: Values of stiffness and damping of suspension component and sprung mass value.

k_{spring}	c_{damper}	$m_{s,actual}$
(N/mm)	(Ns/mm)	(kg)
40	6	635.6

forces to the centre of the wheel, it was necessary to introduce the concept of motion ratio (MR). This parameter only depends on the geometry of the suspension system, which is defined as the ratio between the wheel centre travel and the spring displacement, given a certain load at wheel level. As it is possible to note in the sketch in Figure 4.10, the displacement of the spring is much smaller than that of that of wheel. One of the formulas to evaluate motion ratio MR is presented in Equation (4.4). Studying the equilibrium with respect to the rotation centre of the Lower Control Arm (LCA), it is possible to calculate the ratio between the force at the spring location and at the wheel location. This results in a value equal to the aforementioned motion ratio and to the ratio between the distances of the spring and of the wheel centre from the LCA rotation centre.

$$MR = \frac{d_s}{d_w} = \frac{d_a}{d_b} \quad (4.4)$$

The same concept of motion ratio holds for the shock absorber; since it is usually placed inside the coil spring, the damper and spring motion ratios are equal. In the suspension analyzed in this project, the motion ratio is equal to 0.93.

The procedure to calculate the stiffness parameter to use in the quarter car model is shown in Equation (4.5). Moving the spring from its location to wheel centre, the force decreases, while the displacement increases by means of the motion ratio.

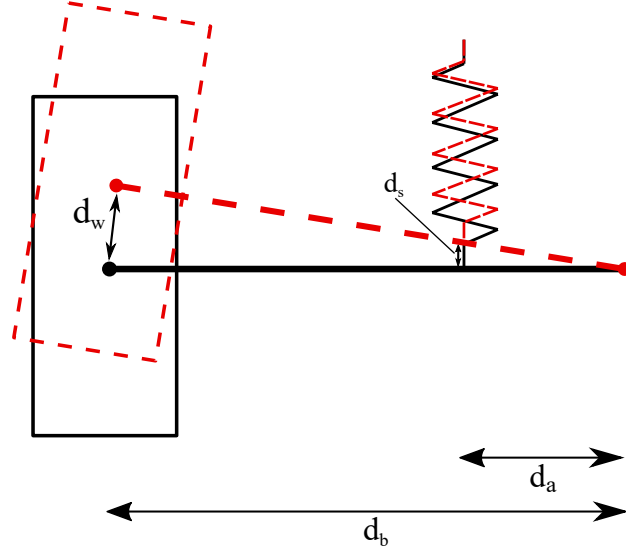


Figure 4.10: Sketch of the suspension assembly in front view.

Table 4.3: Parameters values for the quarter car model.

k_s	c_s	m_s	m_u	k_w
(N/mm)	(Ns/mm)	(kg)	(kg)	(N/mm)
34.30	5.15	545.0	80	294.7

$$k_s = \frac{f_w}{d_w} = \frac{MR \cdot f_s}{\frac{d_s}{MR}} = \frac{f_s}{d_s} = k_{spring} \cdot MR^2 \quad (4.5)$$

A similar procedure can be applied to the other parameters of the suspension assembly. Therefore, to transport the characteristics of the components to the wheel centre, it is sufficient to multiply their numerical values by the square of the motion ratio (MR^2). In Table 4.3, all the parameters used for the quarter car simulation are listed. The quantity that resembles the tire vertical stiffness (k_w) is also presented; it not only depends on the considered type of tire but also on its inflation pressure. The tire considered in this project is a 265/40 R18 97 V inflated at 248 kPa, which approximately corresponds to 35 psi.

4.3.3 Nonlinear Quarter Car Models

The difference between linear and the nonlinear quarter car models used in this project is the damper, which, in the latter model, is a nonlinear device with an asymmetric characteristic. Therefore, the force exerted by the damper and the speed of the stem are linked by a variable damping coefficient.

The curve describing the relationship between force (f_d) and velocity (v_d) refers to the

actual component, therefore it is necessary to transport its characteristic at wheel centre as well in order to have reasonable results.

In Figure 4.11 it is possible to see the actual characteristic of the damper and the same characteristic once transported to the wheel centre. Similar to the other parameters, this characteristic was also moved to the wheel centre by means of the motion ratio; in particular, speed values were divided by MR , while force values were multiplied by the same MR .

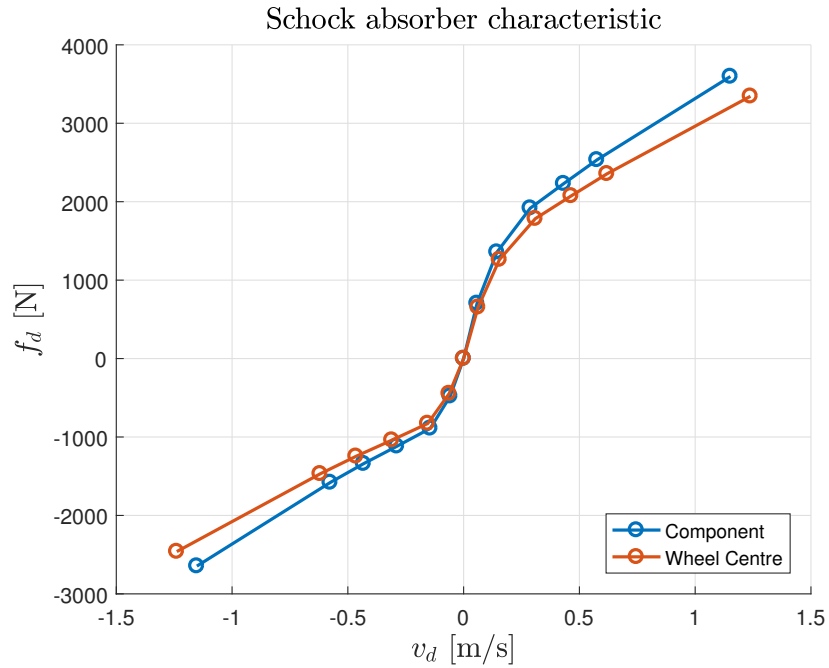


Figure 4.11: Damper characteristic curves: component level (blue) and wheel centre (red)

The results obtained through the numerical simulation for the model shown in this chapter are presented in Chapter 5.

In particular, results obtained from linear models are mostly used in order to validate the model itself through the comparison between time and Laplace domain simulation, while nonlinear models are employed to assess the benefits given by the implementation of the hydraulic top mount.

CHAPTER 5

Simulation Results

In this chapter, the most relevant results obtained by the simulation of the models presented in Chapter 4 are presented. All those plots not shown can be found in Appendix C.

First, results for the linear models are presented, which have been mainly used in order to validate different models: a comparison between analytic and numerical frequency response has been made to this extent.

In the second part of the chapter, results coming from nonlinear simulations are shown. Because of their nonlinearity, it was not possible to analytically evaluate the frequency response; therefore, only time simulation was carried out and then the Fast Fourier Transform (FFT) for the relevant output signals were estimated using MATLAB®.

5.1 Linear Models

The results coming from the simulations performed for linear models were mainly used to validate Simulink® models.

It was possible to achieve this task for linear models since its transfer function was first determined analytically, and thus could be compared with the estimated transfer function.

5.1.1 Hydraulic Top Mount

Time simulation

The time simulation for the hydraulic top mount was performed employing a chirp signal as the input displacement signal (u): a sinusoidal signal whose frequency increases linearly.

The parameter values were chosen in order to have a sufficiently slow input and a standard amplitude of 1 mm. Input signal parameters are shown in Table 5.1, while its variation in time is shown in Figure 5.1.

Table 5.1: Parameters values for the chirp signal employed as input of the simulation for the hydraulic top mount.

Initial Frequency	Target Time	Frequency at Target time	Amplitude
(Hz)	(s)	(Hz)	(mm)
0	1	1	1

In Figure 5.2, the variation of the force f_t in time is shown. At low excitation frequencies, force amplitude is relatively small and it tends to increase at high frequencies. In particular, a rather high step can be seen around 20 – 25 s, which corresponds to the frequency range of 20 – 25 Hz according to the parameters of the input signal.

Nevertheless, the variation of the force according to the excitation frequency is clearly shown by the transfer function.

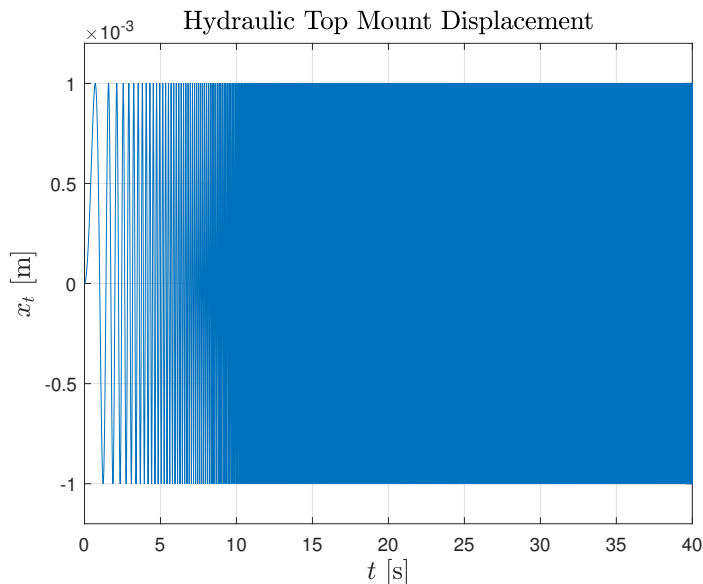


Figure 5.1: Input displacement for the hydraulic top mount time simulation.

Transfer Function Analysis

The transfer function analysis was performed by building the Bode diagrams of the hydraulic top mount transfer function (G), whose analytic expression was presented in Chapter 3. In particular, this transfer function represents the variation of the hydraulic mount dynamic stiffness according to frequency.

Since the frequency range of interest is located in the low frequency range and because said range is very narrow, all the transfer functions is represented with a linear frequency axis differently from common practice for Bode diagrams. In addition, the transfer function relative to the hydraulic mount is represented with absolute scale for the magnitude axis as well. The dynamic stiffness of the hydraulic mount is shown in Figure 5.3.

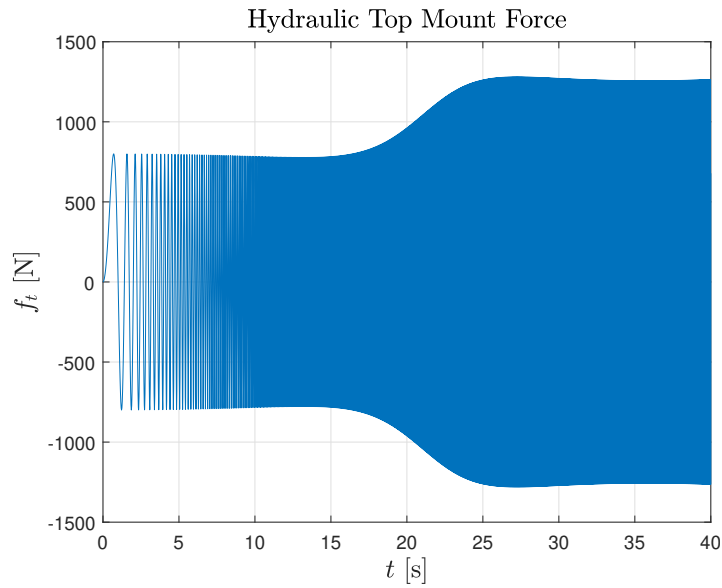


Figure 5.2: Variation in time of the force exerted by the hydraulic top mount due to the chirp signal used as input.

The Bode diagram for dynamic stiffness reflects the variation in time of force f_t ; an apparent increase in the magnitude of the force is displayed in the frequency range between 20 Hz and 25 Hz, while a flat curve, resembling a nearly constant value of the force at higher frequencies, is present above 25 Hz. Moreover, the same value of the force (f_t) can be obtained by multiplying the input displacement by the value of the dynamic stiffness amplitude for any frequency value.

The sudden increase in dynamic stiffness at high frequencies, together with its consequent flattening, is due to the hydraulic component of the top mount, which, as expected, provides an increased amount of damping beyond a certain excitation frequency. The be-

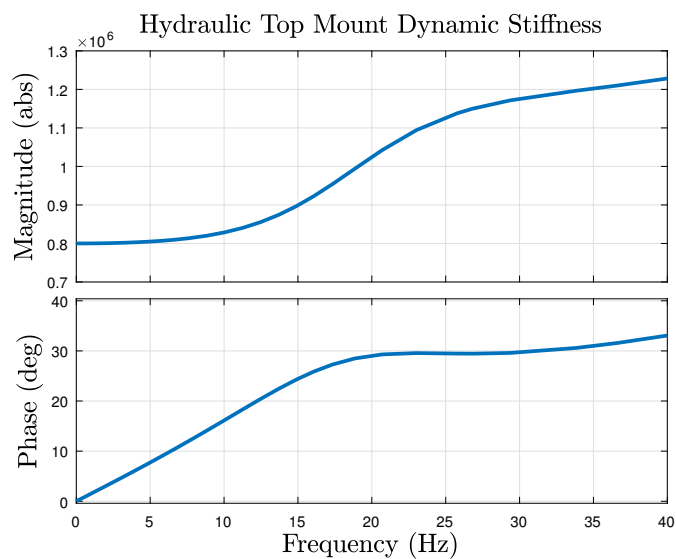


Figure 5.3: Variation of the hydraulic top mount dynamic stiffness in Laplace domain.

haviour of this type of mount is completely different from a traditional mount as explained in Section 5.1.2.

Once the analysis of frequency response had been completed, it was decided to verify that the Simulink[®] model, meant to solve differential equations, were correct.

In order to perform this comparison, the MATLAB[®] function “`tfestimate`” was employed. This allows one to evaluate a transfer function starting from the numerical values of input and output signal in the time domain. Therefore, input and output signals evaluated through the time simulation were used as the argument for this function and the resulting Bode diagram has been superimposed to the analytic one.

The superimposition between the two Bode diagrams can be seen in Figure 5.4. It is apparent that the Bode diagrams for both magnitude and phase are perfectly superimposed except for some very small deviations, which are probably due to numerical inaccuracies. This result further confirms that the block diagram developed for the hydraulic top mount is able to provide reliable results.

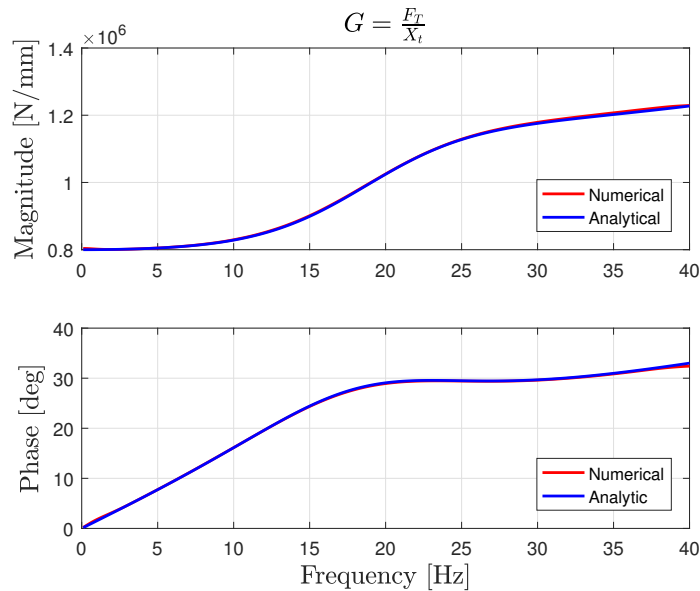


Figure 5.4: Comparison between the analytic Bode diagram and the numerical one for the hydraulic top mount model.

5.1.2 Rubber Top Mount

Time Simulation

The time simulation of the rubber top mount model was performed using the same input signal used for the hydraulic top mount. Also in this case, the time history for the force generated by the top mount f'_t and the dynamic stiffness in the time domain was evaluated.

In Figure 5.5 the variation in time of the force generated by the top mount is shown. It is possible to note that, in this case, a sudden increase of the force is not present as in the case of the hydraulic mount, but rather the force increases almost steadily in time.

From this time history, it is possible to expect a nearly linear dynamic stiffness.

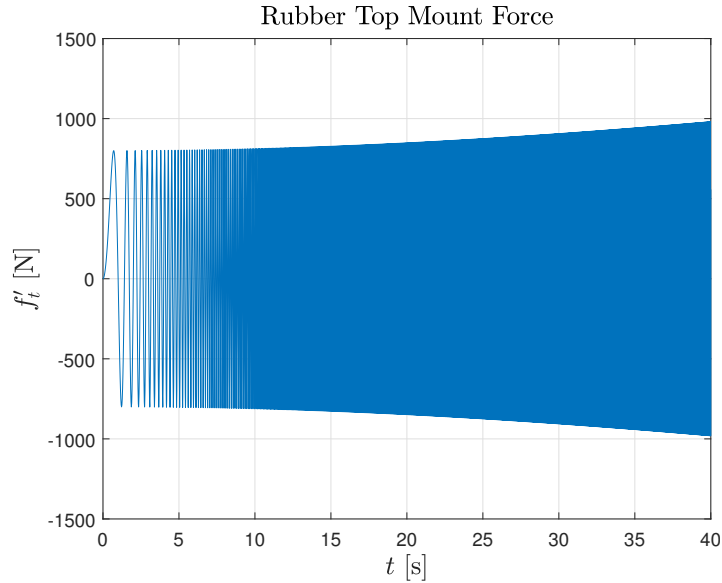


Figure 5.5: Variation in time of the force f'_t generated by the rubber top mount due to a chirp input displacement.

Transfer Function Analysis

The transfer functions of this system were analyzed in a similar manner to those of the hydraulic top mount. The Bode diagrams for amplitude and phase are presented in Figure 5.6.

As expected, the dynamic stiffness monotonically increases according to the frequency: at the lowest frequencies it is comparable to the dynamic stiffness of the hydraulic top mount, while at the highest frequencies it results to be lower than that of the hydraulic top mount.

The difference with the hydraulic top mount dynamic stiffness is apparent. In the case of the hydraulic top mount, it is constantly increasing throughout the whole frequency range differently from the step-wise shape of the hydraulic top mount. Similarly, the phase does not present the “plateau” beyond the frequency at which the mount is tuned.

Moreover, in the case of the rubber top mount the range of dynamic stiffness amplitude is much smaller than hydraulic mount one, confirming the difficulties in tuning the device at different frequency ranges to accomplish the different requirements.

Moreover, in the case of the rubber top mount, Bode diagrams obtained analytically have been compared to those evaluated through the time simulation. One of the plots resulting from the superposition of the two Bode diagrams has been presented in Figure 5.7. Also for this system, the two transfer functions coincide, confirming the accuracy of the numerical model.

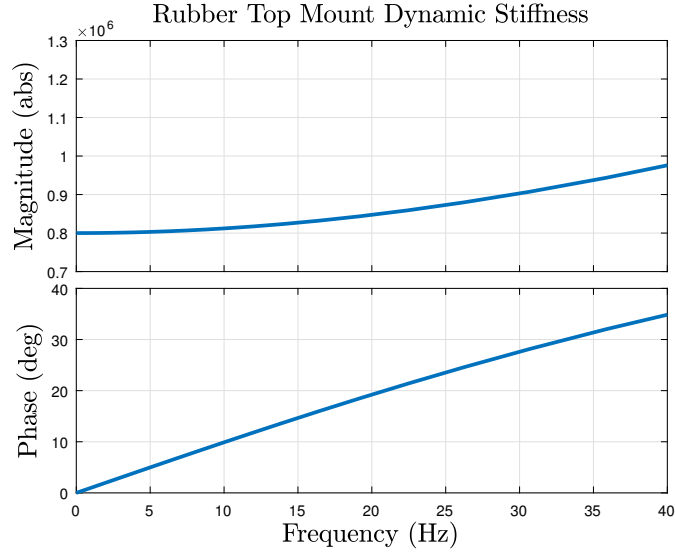


Figure 5.6: Dynamic stiffness variation in function of frequency for the rubber top mount.

5.1.3 Quarter Car Model with the Hydraulic Top Mount

Time Simulation

The most relevant plots for the time simulation of the linear quarter car models are the displacement and the acceleration of both sprung and unsprung mass. Moreover, as anticipated in Chapter 3, other important figures like Root Mean Square (RMS) values of the acceleration and its range have been evaluated for both sprung and unsprung mass.

The parameters chosen for the input signal are shown in Table 5.2. The amplitude value chosen is common among automotive manufacturers for this kind of simulation, while the frequency values have been selected in order to have a sufficiently slow increase in frequency to run the simulation.

The input signal time history is very similar to the input signal used for the two top mounts. For the sake of brevity, this time history, as well as the time histories of sprung and unsprung mass accelerations, can be found in Appendix C. Instead, in Figures 5.8 and 5.9, the sprung and unsprung mass displacement time histories are shown.

The displacement of the sprung mass in Figure 5.8 presents a very sharp peak around $t = 10$ s corresponding to a frequency around 1 Hz: it coincides with the bounce mode of the vehicle. Then, the displacement is quickly damped until a second small peak is encountered around $t = 100$ s, which, instead, corresponds with a frequency of about

Table 5.2: Parameters values for the chirp signal employed as simulation input for the linear quarter car models.

Initial Frequency (Hz)	Target Time (s)	Frequency at Target time (Hz)	Amplitude (mm)
0.1	10	1	3.82

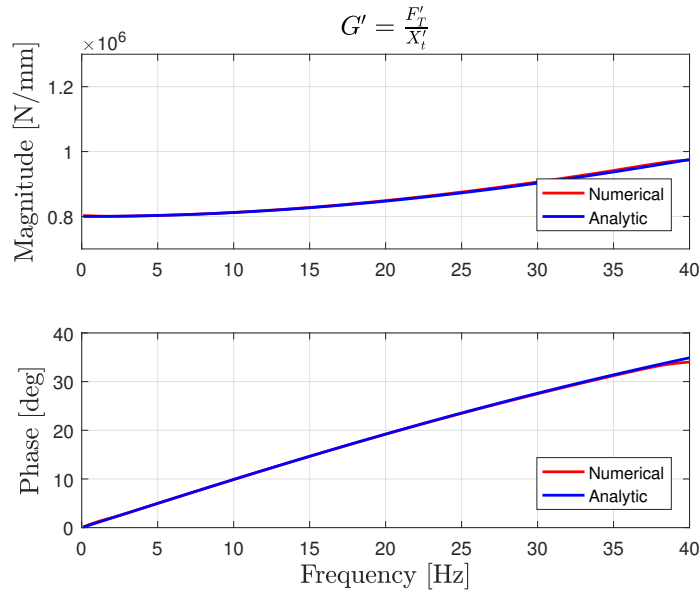


Figure 5.7: Comparison between numerical and analytic transfer function for the rubber top mount.

10 Hz. This second peak should represent the wheel hop mode of the vehicle. The same two peaks can be also noticed in the time history for the unsprung mass displacement, but in this case the second one is more pronounced.

Finally, in Table 5.3, Root Mean Square (RMS) values of acceleration and its range for sprung and unsprung mass are shown.

Table 5.3: Values of RMS acceleration and range for sprung and unsprung mass in the quarter car model with hydraulic mount.

$\ddot{x}_{s,RMS}$ (m/s ²)	$\ddot{x}_{u,RMS}$ (m/s ²)	$\ddot{x}_{s,range}$ (m/s ²)	$\ddot{x}_{u,range}$ (m/s ²)
0.91	11.96	4.48	46.93

Transfer Function Analysis

After the time simulation, the transfer functions presented in Chapter 3 were evaluated. Bode diagrams for amplitude and phase with linear scale for magnitude were generated using a MATLAB[®] code and the most relevant ones are shown in Figures 5.10 and 5.11.

It is possible to note that the shapes of the transfer functions resembles the time histories of the corresponding signals, even though it is necessary to keep in mind that frequency domain graphs have a logarithmic scale on the magnitude axis, while time histories have been represented with a linear scale on the y-axis. In particular, diagrams relative to displacement present the two peaks at bounce and wheel hop frequencies, at 1.18 Hz and at 10.30 Hz, respectively. Relative amplitude values for sprung and unsprung

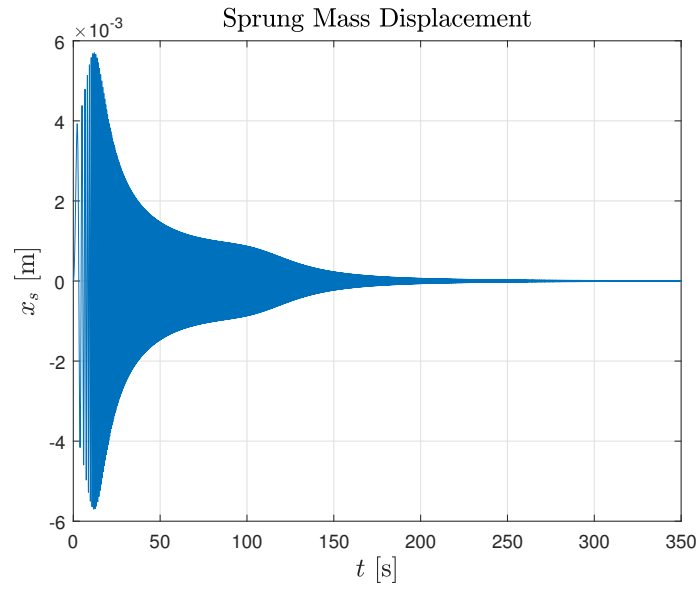


Figure 5.8: Time history of the sprung mass displacement in the linear quarter car model with the hydraulic top mount.

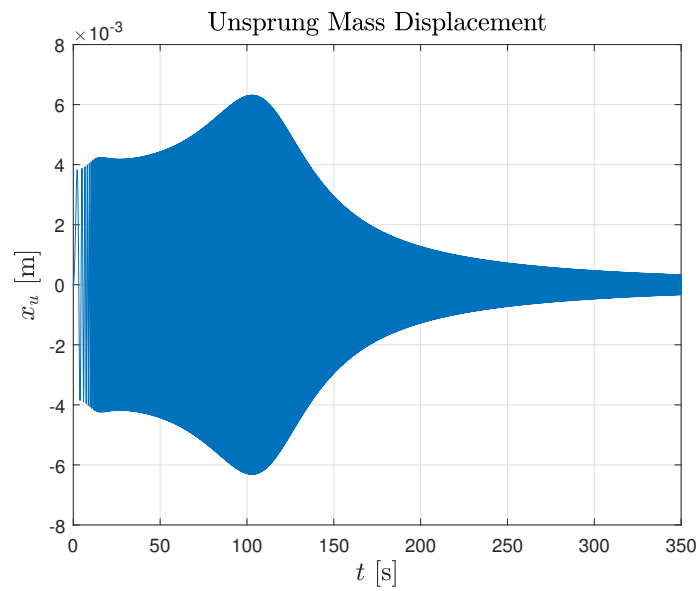


Figure 5.9: Time history of the unsprung mass displacement in the linear quarter car model with the hydraulic top mount.

mass are presented in Table 5.4.

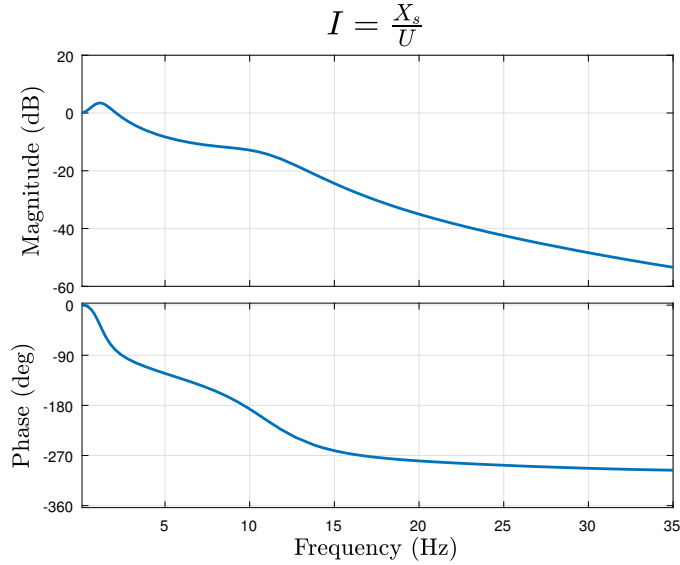


Figure 5.10: Bode diagram for amplitude and phase for the transfer function between the sprung mass displacement and the input displacement in the case of the quarter car model with the hydraulic top mount.

Table 5.4: Values of the peak magnitude in dB of sprung and unsprung mass displacements for the quarter car with the rubber top mount.

	Frequency (Hz)	Magnitude (dB)
Sprung Mass	1.18	3.89
	10.30	-17.12
Unsprung Mass	1.18	1.17
	10.30	0.094

In order to verify the reliability of the Simulink[®] model, Bode diagrams obtained analytically were superimposed to those estimated starting from the time histories. An example of a diagram showing the overlapped transfer function is presented in Figure 5.12.

Once again, all the diagrams generated following this procedure show a nearly perfect superimposition, proving the accuracy of the model. After the verification of the model, it was possible to take a step forward, developing the nonlinear quarter car models, which were employed to compare and to assess the performance of the two different mounts.

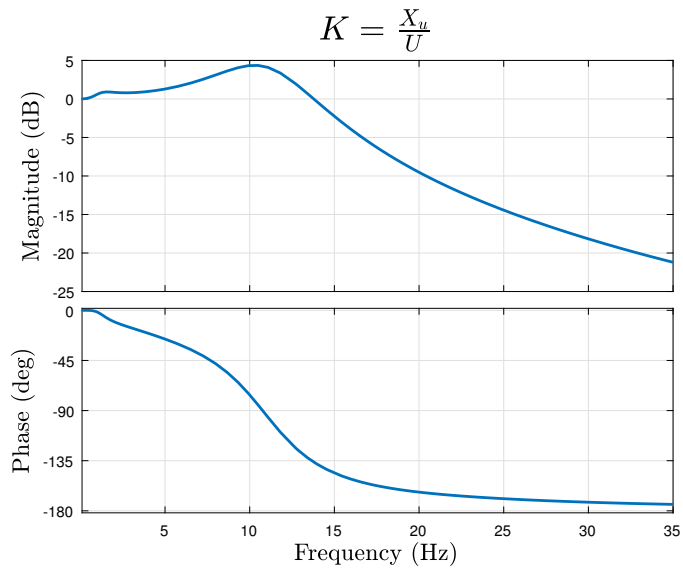


Figure 5.11: Bode diagram for amplitude and phase for the transfer function between the unsprung mass displacement and the input displacement in the case of the quarter car model with the hydraulic top mount.

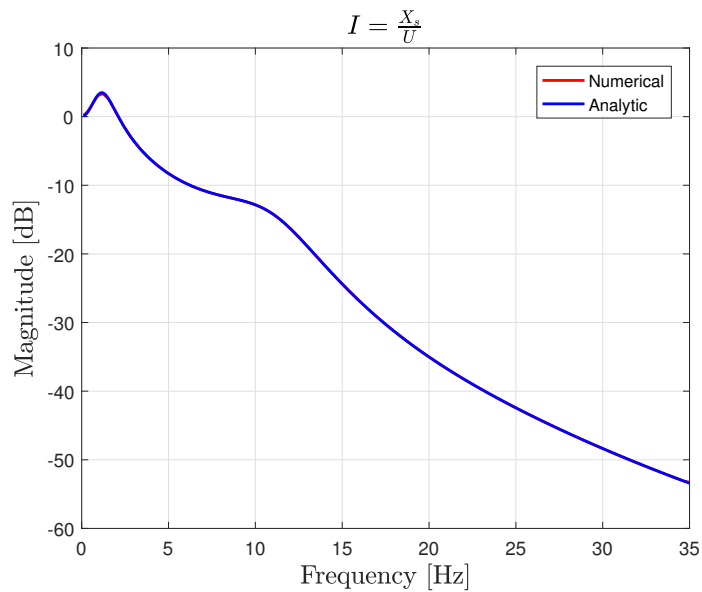


Figure 5.12: Comparison between analytic and estimated amplitude Bode diagrams of the transfer function I of the quarter car model with the hydraulic top mount.

5.1.4 Quarter Car Model with the Rubber Top Mount

Time Simulation

The same plots generated for the quarter car model with the hydraulic top mount have been obtained for the quarter car model with the conventional rubber top mount, namely time histories of sprung and unsprung mass displacement and acceleration. In order to run the simulation, the same input employed for the model with the hydraulic top mount was used.

In Figures 5.13 and 5.14 the time histories of sprung and unsprung mass displacement are shown, while, in Table 5.5, RMS values and range of the acceleration are reported.

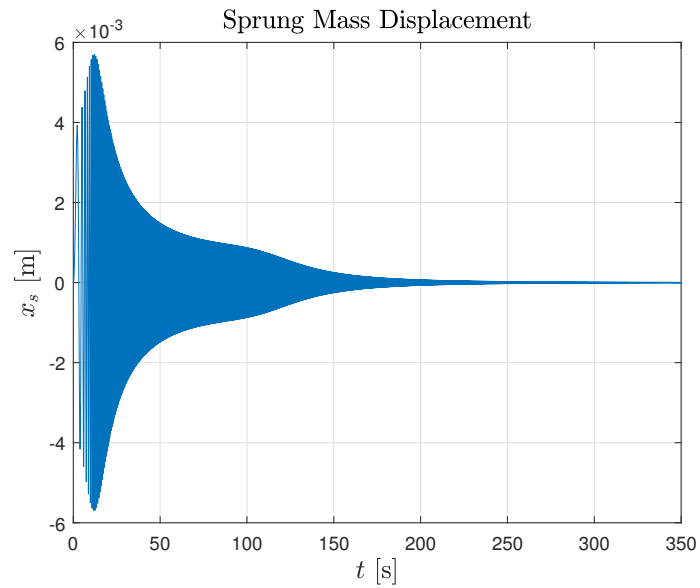


Figure 5.13: Sprung mass displacement in function of time for the quarter car model with rubber the rubber top mount.

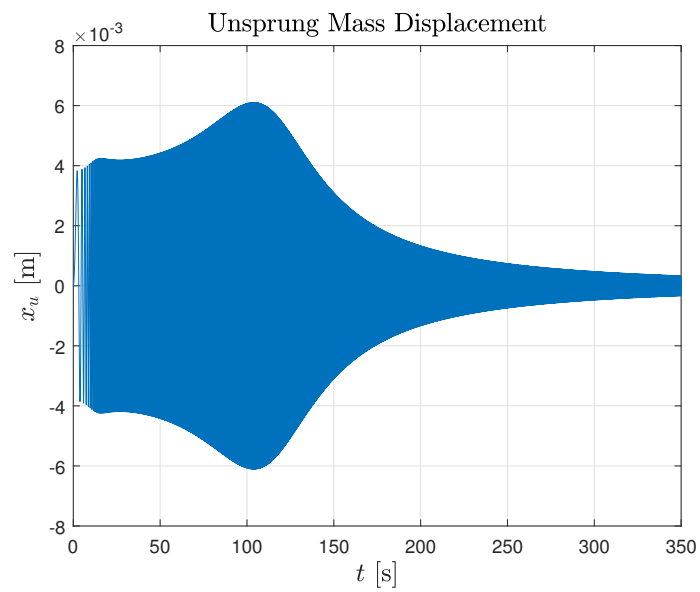


Figure 5.14: Unsprung mass displacement in function of time for the quarter car model with rubber the rubber top mount.

Table 5.5: RMS values of acceleration and range for sprung and unsprung mass in the quarter car model with the rubber top mount.

$\ddot{x}_{s,RMS}$ (m/s ²)	$\ddot{x}_{u,RMS}$ (m/s ²)	$\ddot{x}_{s,range}$ (m/s ²)	$\ddot{x}_{u,range}$ (m/s ²)
0.94	12.38	4.58	49.35

Transfer Function Analysis

As was the case for the previous model, the transfer functions were initially analyzed by simply plotting the Bode diagrams for amplitude and phase. Later, the comparison with the estimated transfer functions were carried out.

Bode diagrams for the transfer functions I and K defined in Chapter 3 have been presented in Figures 5.15 and 5.16. The trend of the magnitude plots is similar to that obtained for the configuration of the quarter car with the hydraulic top mount, with the peaks for bounce and wheel hop in the displacement transfer functions, whose frequency values are 1.17 Hz and 10.03 Hz, respectively. Peak amplitude values for sprung and unsprung mass are reported in Table 5.6.

Applying the same procedure seen for the quarter car model with the hydraulic top mount, analytic amplitude Bode diagrams have been compared to those estimated from time simulation. The plot comparing the analytic transfer function I and its numerical estimate has been shown in Figure 5.17. No differences were found between the superimposed graphs in this case either.

5.2 Nonlinear Models

In this section, the results obtained from the simulation of the nonlinear quarter car models with the hydraulic and the rubber top mounts are presented. For the two different configurations of the quarter car model, results in the time and frequency domains are

Table 5.6: Values of the peak magnitude in dB of sprung and unsprung mass displacements for the quarter car model with the rubber top mount.

	Frequency	Magnitude
	(Hz)	(dB)
Sprung Mass	1.17	3.88
	10.03	-17.1
Unsprung Mass	1.17	1.17
	10.03	-0.22

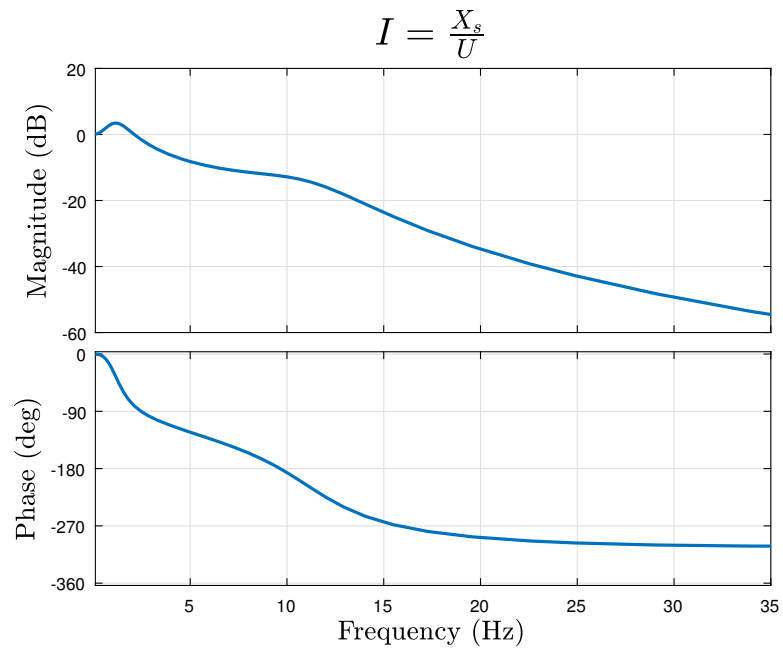


Figure 5.15: Bode diagram for amplitude and phase of the transfer function I between the sprung mass displacement and the input signal in the case of the quarter car with the rubber top mount.

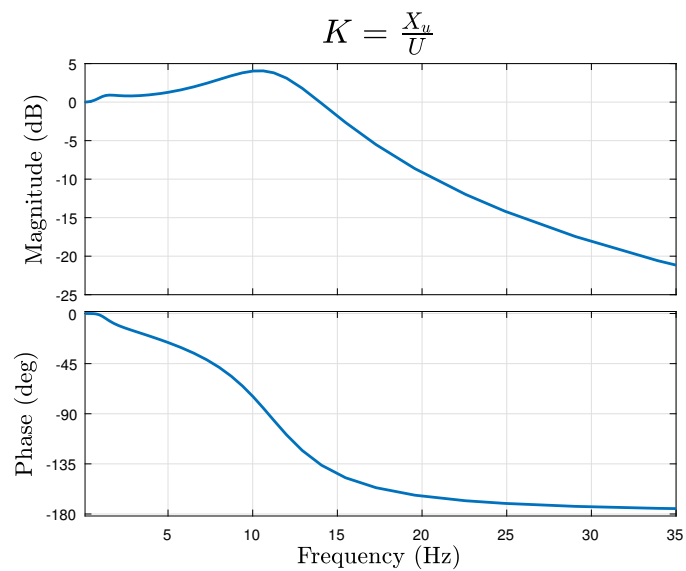


Figure 5.16: Bode diagram for amplitude and phase of the transfer function K between the unsprung mass displacement and the input signal in the case of the quarter car model with the rubber top mount.

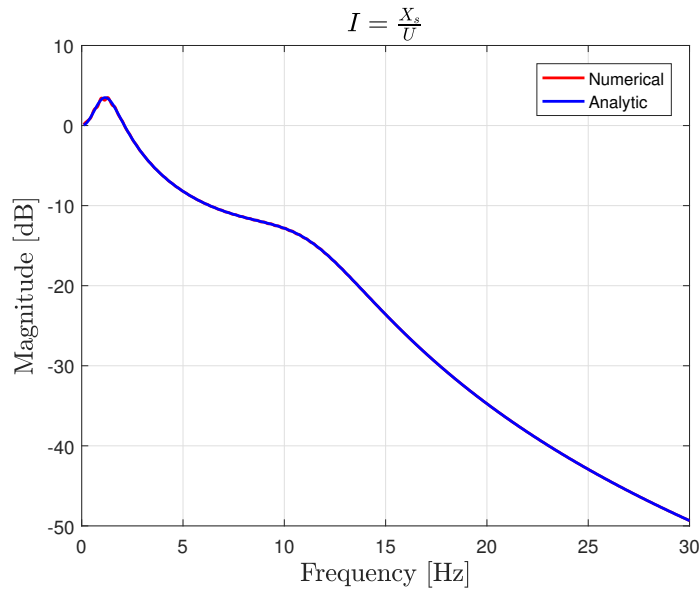


Figure 5.17: Comparison between the analytic and estimated amplitude bode diagram of the transfer function I for the quarter car model with the rubber top mount.

shown. In particular, frequency response is presented in the form of Fast Fourier Transform (FFT) plots for sprung and unsprung mass displacement and acceleration.

5.2.1 Input Signals

Since the results of the nonlinear simulations were used to perform the comparison between the different solutions, more realistic input signals were necessary. Therefore, three different input signals were used to perform the simulations: smooth and rough random roads and a single asperity signal.

Random Road Inputs

Roads are usually classified according to the ISO 8608, which defines road profiles according to their displacements, velocity and acceleration Power Spectral Density (PSD). In this way, eight different classes (from A to H) are identified in order to classify road profiles [27]. The two road profiles considered in this thesis belong to the A and D classes and their profiles are shown in Figures 5.18a and 5.18b.

In order to obtain input signals to run the simulation, it was necessary to express the road profiles as a function of time instead of as function of the “travelled distance”. Time data can be found by dividing the data about the travelled distance by the constant speed v . For the quarter car model in both configurations and for the first two inputs, a speed of 40 km/h was selected. In this way, input signals shown in Figures 5.19a and 5.19b were obtained.

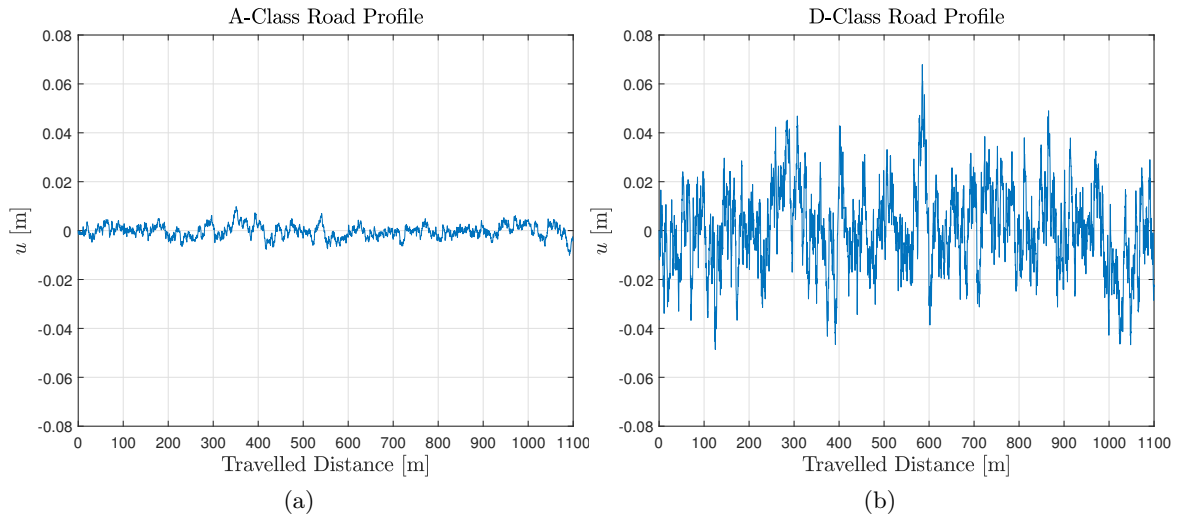


Figure 5.18: Input road signal employed to run the simulation of the nonlinear quarter car models.

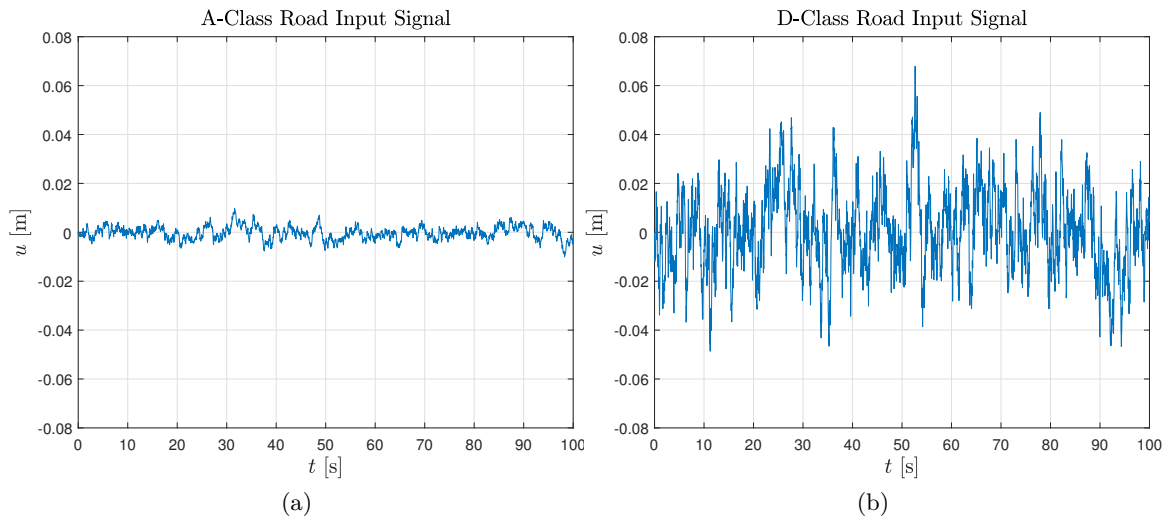


Figure 5.19: Input road signals in time domain employed to run the simulation of the nonlinear quarter car models.

Single Asperity Input

Asperities on actual roads are rather sharp irregularities, but they are enveloped through the physical and geometrical characteristics of tires encountering the asperity itself. Since in quarter car models, the tire contact patch with the ground is a single point, the asperity signal has been modelled as a half sine wave with a 25 mm amplitude and a 150 mm length in order to simulate the actual contact as much as possible .

The asperity profile can be seen in Figure 5.20a, while the corresponding input signal for a speed equal to 30 km/h is shown in Figure 5.20b. Since the wavelength of the time signal is very short, its spectrum in frequency has to be very wide; therefore, the system is excited in a very wide frequency range.

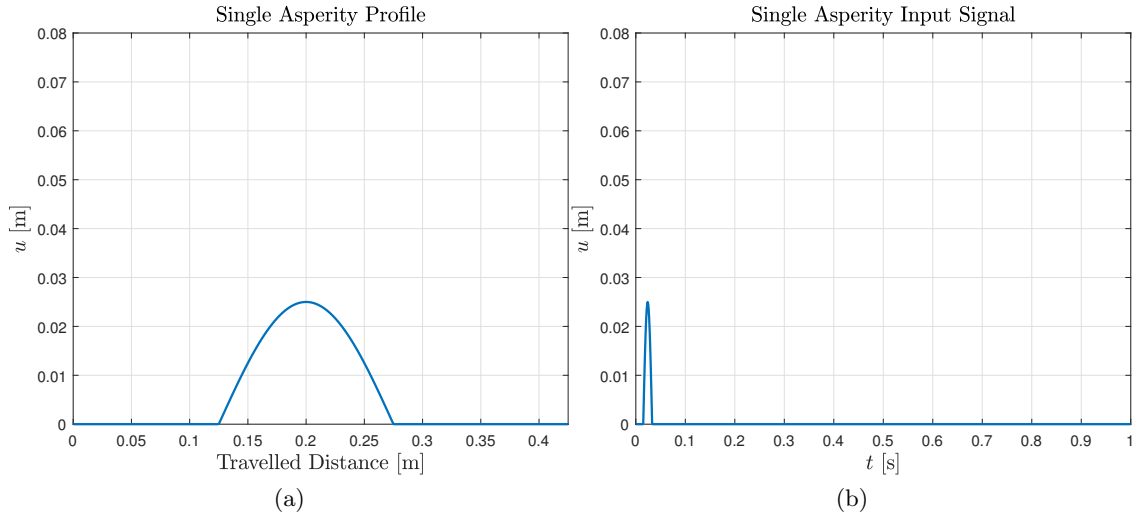


Figure 5.20: Profile of the single asperity signal in function of the travelled distance and input signal in function of time.

5.2.2 Quarter Car Model with the Hydraulic Top Mount

Time Simulation: Random Road Inputs

Time histories resulting from the time simulation for the quarter car model equipped with hydraulic mount are shown in Figures 5.21a, 5.21b, 5.22a and 5.22b, while data about RMS values and range of acceleration for sprung and unsprung mass is shown in Table 5.7. For nonlinear models beside the overall RMS values, the components of RMS acceleration for the primary (\dot{x}'_u and \dot{x}'_s) ride and the secondary ride (\dot{x}''_u and \dot{x}''_s) were evaluated and are presented in Table 5.8. These quantities allow one to better understand which range of frequency is more affected by the top mount. It is possible to notice that for sprung mass the two components are very similar, while for the unsprung mass the component of the secondary ride is very dissimilar from the component of the primary ride. These results can be explained through the frequency response analysis developed in Section 5.2.2.

As expected, data about displacement and acceleration given by the smooth A-class road is one order of magnitude smaller than those of the D-class road. This behaviour can be seen in time history plots as well as in the values of RMS acceleration, acceleration range and RMS of road holding index (η_{rh}).

Time Simulation: Single Asperity Input Signal

The third input signal employed to simulate the quarter car model is the single asperity signal. This type of signal was chosen because it is able to excite the system in a wide frequency range.

In Figures 5.23 and 5.24, the displacement of sprung and unsprung masses are presented. The plots show a sharp peak in correspondence of the asperity, then the sprung mass presents a relevant undershoot, before the displacement slowly goes to 0. By contrast,

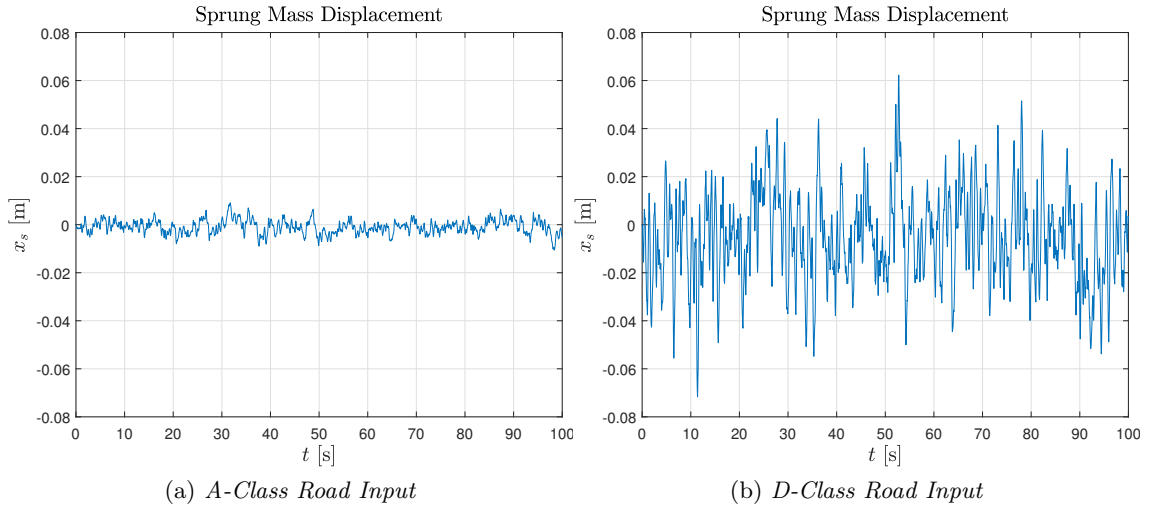


Figure 5.21: Sprung mass displacement in function of time for the quarter car model with the hydraulic top mount in the case of A-class road input (a) and D-class road input (b).

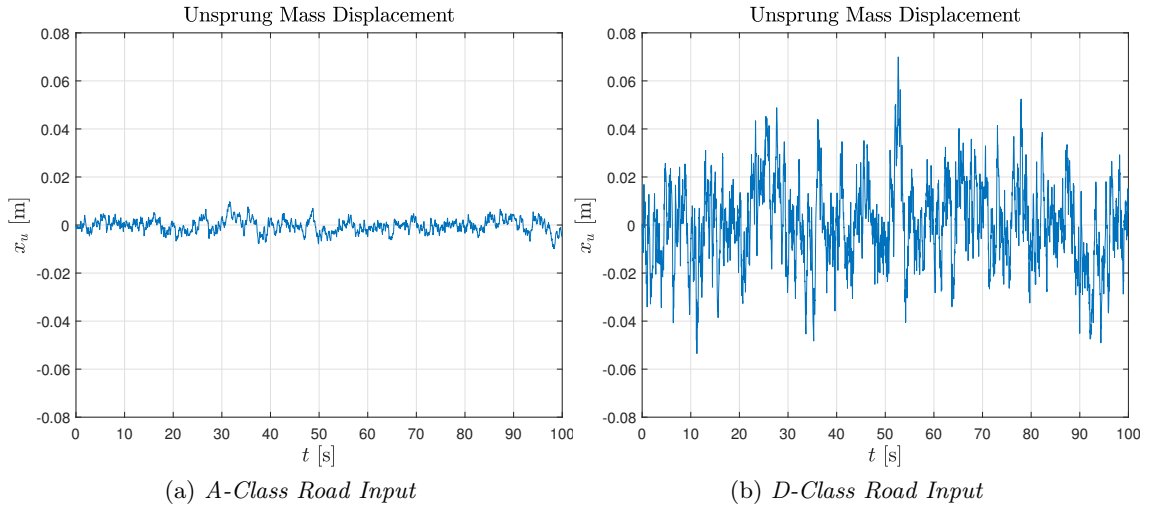


Figure 5.22: Unsprung mass displacement in function of time for the quarter car model with the hydraulic top mount in the case of A-class road input (a) and D-class road input (b).

Table 5.7: RMS values and range of sprung and unsprung mass accelerations for the quarter car model with the hydraulic top mount.

	$\ddot{x}_{s,RMS}$ (m/s ²)	$\ddot{x}_{s,range}$ (m/s ²)	$\ddot{x}_{u,RMS}$ (m/s ²)	$\ddot{x}_{u,range}$ (m/s ²)	$\eta_{rh,RMS}$ (-)
A-Class Input	0.285	2.16	0.922	7.02	0.0266
D-Class Input	1.79	10.65	10.15	104.11	0.183

the unsprung mass appears to oscillate before its displacement is nullified.

Table 5.8: Components of RMS acceleration values of sprung and unsprung mass accelerations for primary and secondary ride in the case of the quarter car model with and random road inputs.

	0 – 5 Hz	5 – 20 Hz	0 – 5 Hz	5 – 20 Hz
	$\ddot{x}'_{s,RMS}$ (m/s ²)	$\ddot{x}'_{s,RMS}$ (m/s ²)	$\ddot{x}'_{u,RMS}$ (m/s ²)	$\ddot{x}''_{u,RMS}$ (m/s ²)
A-Class Input	0.216	0.185	0.272	0.868
D-Class Input	1.21	1.29	2.09	9.65

It is important to underline that the sprung mass is much slower than the unsprung mass in reaching the equilibrium conditions. In fact, at the end of the simulation time, the displacement is not null for the sprung mass.

Performance indexes like RMS acceleration and range were evaluated and they have been presented in Table 5.9 with the component for the RMS values presented in Table 5.10. As opposed to the random road input, both sprung and unsprung mass accelerations are more important in the secondary ride.

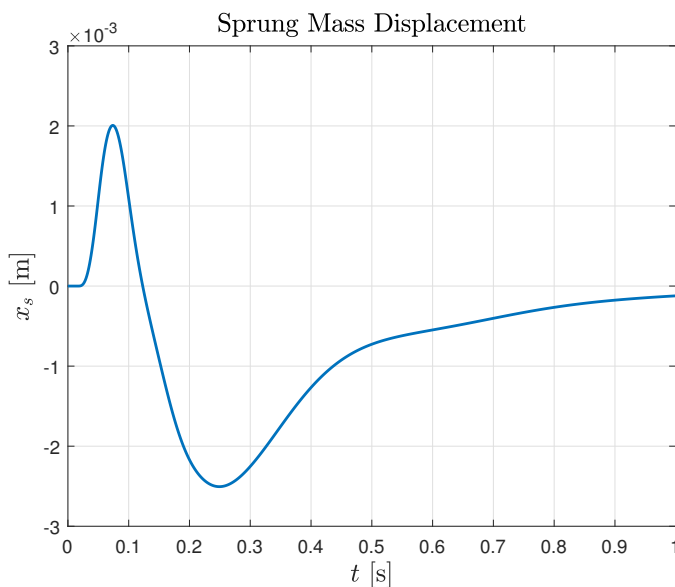


Figure 5.23: Displacement of the sprung mass due to single asperity input for the quarter car model with the hydraulic top mount.

Fast Fourier Transform: Random Road Input Signals

In order to analyze the frequency response of the model, it was necessary to estimate the Fourier Transform of the output time signal through the Fast Fourier Transform (FFT) algorithm implemented on MATLAB[®]. The Fourier Transform of a signal allows to understand which frequencies are contributing the most to the signal itself. FFT plots have

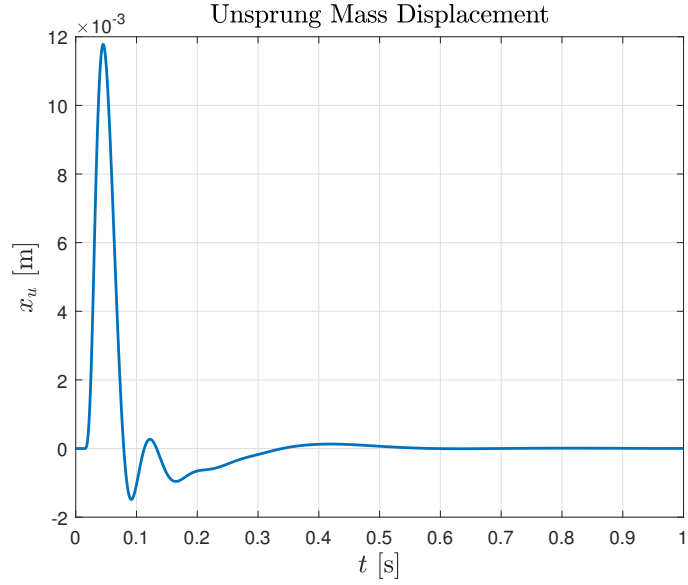


Figure 5.24: Displacement of the unsprung mass due to single asperity input for the quarter car model with the hydraulic top mount.

Table 5.9: RMS and range values for the acceleration of sprung and unsprung mass in the case of the nonlinear quarter car model with the hydraulic top mount due to a single asperity signal.

$\ddot{x}_{s,RMS}$	$\ddot{x}_{u,RMS}$	$\ddot{x}_{s,range}$	$\ddot{x}_{u,range}$	$\eta_{rh,RMS}$
m/s ²	m/s ²	m/s ²	m/s ²	(-)
0.731	10.52	6.62	132.33	0.135

Table 5.10: Components of RMS acceleration values of sprung and unsprung mass acceleration for the primary ride and the secondary ride in the case of the quarter car model with the hydraulic top mount and a single asperity input.

0 – 5 Hz	5 – 20 Hz	0 – 5 Hz	5 – 20 Hz
$\ddot{x}'_{s,RMS}$	$\ddot{x}''_{s,RMS}$	$\ddot{x}'_{u,RMS}$	$\ddot{x}''_{u,RMS}$
(m/s ²)	(m/s ²)	(m/s ²)	(m/s ²)
0.258	0.669	0.657	7.98

been generated for the displacement and the acceleration of sprung and unsprung masses and are shown in Figures 5.25a, 5.25b, 5.26a, 5.26b, 5.27a, 5.27b, 5.28a and 5.28a.

It is noticeable that only a small portion of the frequency spectrum contributes to the output signal and high frequencies are completely filtered by the system. In particular, considering A-class road input signals, acceleration contributions are almost null beyond 15 Hz for both random inputs, while displacement contributions are null at 5 Hz for the

sprung mass and after 10 – 15 Hz for the unsprung mass. In case of D-class road input, frequency contributions beyond this frequency value are really low, but not null: null values are moved slightly forward in these cases.

Moreover, it is notable that two different peaks characterize the acceleration Fourier transform of the sprung mass, the first in the primary ride, while the other in the secondary ride. The Fourier transform, then, explains why the two components of the RMS are not dissimilar. In the case of unsprung mass acceleration, instead, the only peak that can be found is in the secondary ride, which is why the most important component of the RMS acceleration is that of the secondary ride. As in the time simulation, FFT due to D-class road input are also characterized by one order of magnitude higher than the signals relative to the A-Class road input.

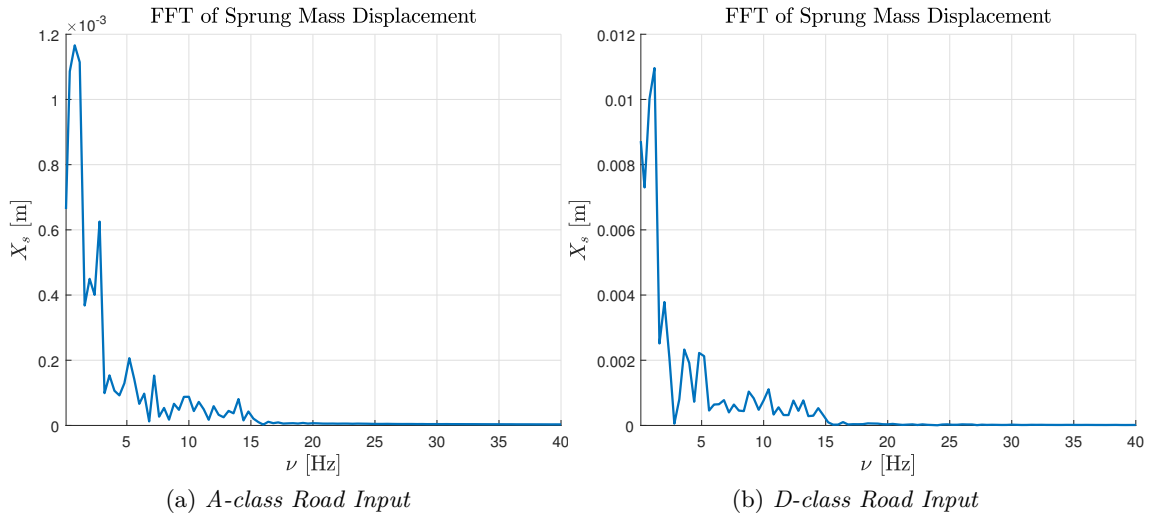


Figure 5.25: Fast Fourier Transform of the sprung mass displacement for the nonlinear quarter car model with hydraulic mount.

Fast Fourier Transform: Single Asperity Input Signals

The results given by the simulation performed with a single asperity as the input were also analyzed in the frequency domain through the FFT.

The first important difference between FFT plots relative to the asperity input signals with frequencies up to 180 Hz. Moreover, in the acceleration plots the range at which frequency contributions are not null is wider than in the case of the displacements. In the case of sprung mass displacement, a clear peak is shown around 1 Hz, while all the other frequencies are almost completely filtered. Looking at the unsprung mass, two peaks are noticeable, but the most important one occurs around 10 Hz.

Plots relative to accelerations show peaks around 11 Hz and 12 Hz, however frequency contributions are not null until 60 Hz and 80 Hz for sprung and unsprung masses, respectively. Since the peaks of acceleration are located in the secondary ride frequency range, the most relevant components of the RMS should be that of the secondary ride as shown

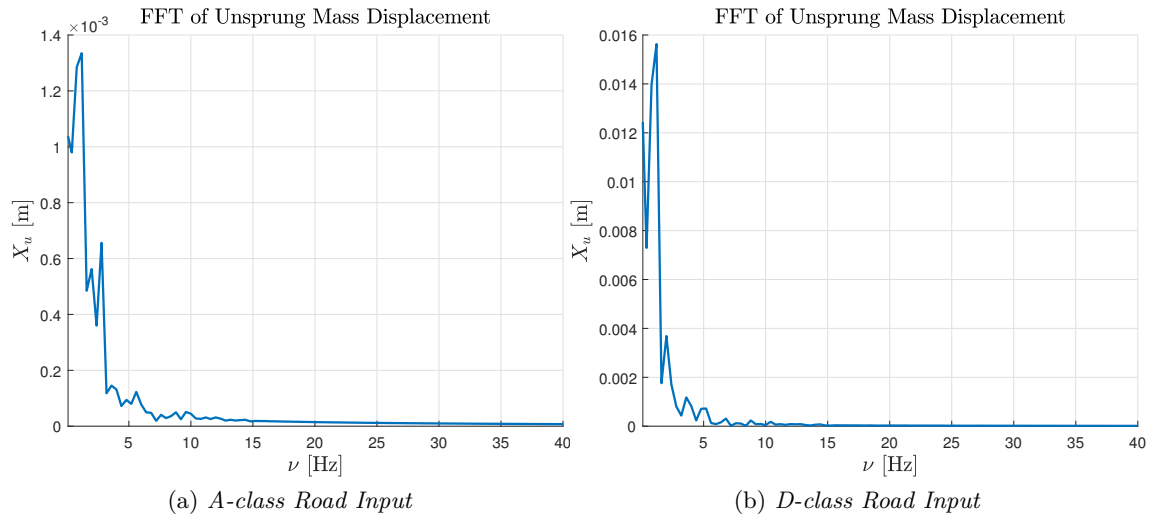


Figure 5.26: Fast Fourier Transform of the unsprung mass displacement for the nonlinear quarter car model with hydraulic mount.

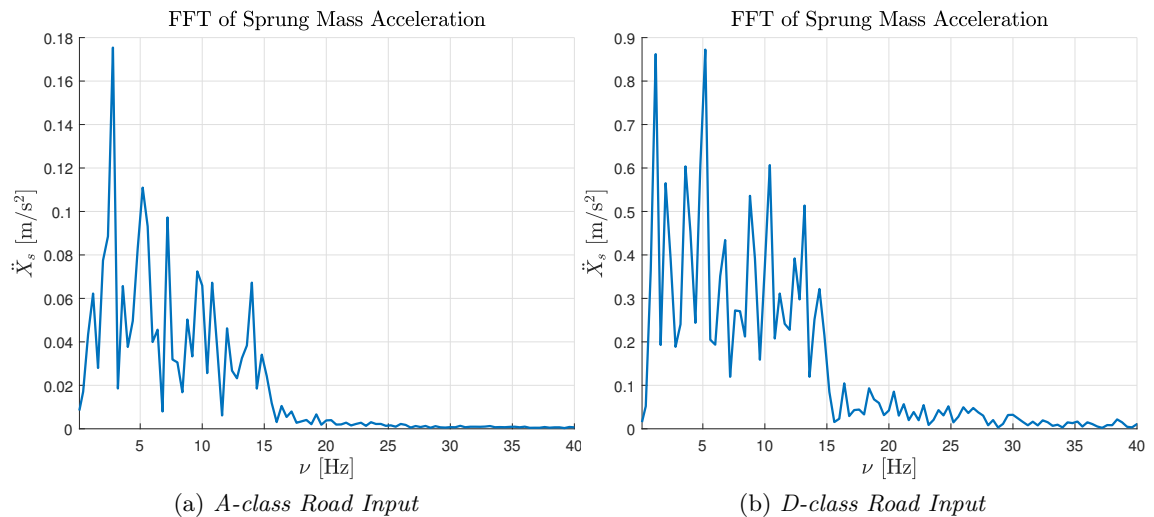


Figure 5.27: Fast Fourier Transform of the sprung mass acceleration for the nonlinear quarter car model with hydraulic mount.

in Table 5.10. In addition, FFT plots are shown in Figures 5.29a, 5.29b, 5.30a and 5.30b.

5.2.3 Quarter Car Model with the Rubber Top Mount

Time Simulation: Random Road Input Signals

The same type of simulation performed for the quarter car model with the hydraulic top mount was also performed for the quarter car with the rubber top mount. The most relevant simulation results are shown in Figures 5.31a, 5.31b, 5.32a and 5.32b. In Table 5.11, RMS acceleration and range are shown.

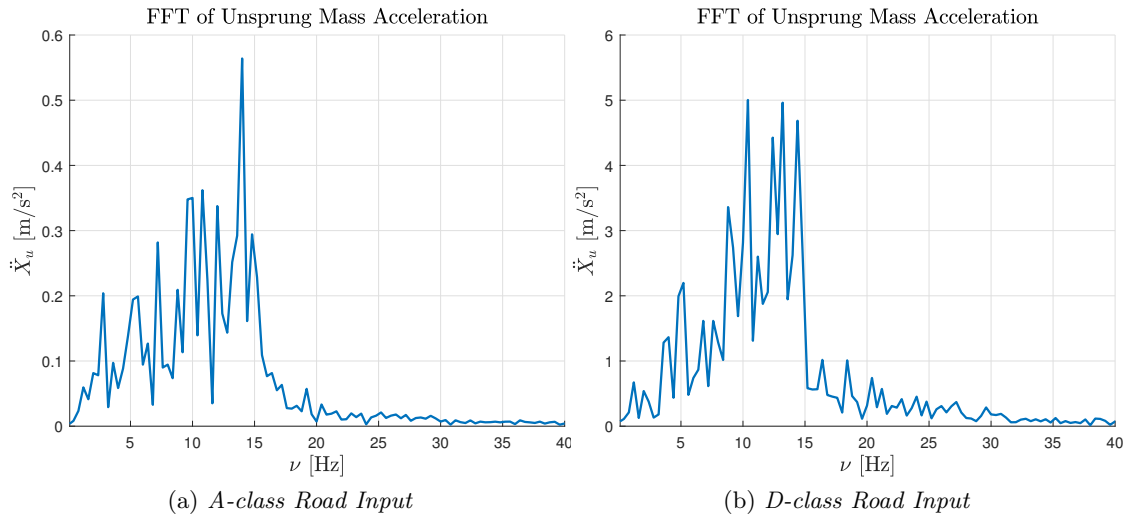


Figure 5.28: Fast Fourier Transform of the unsprung mass acceleration for the nonlinear quarter car model with hydraulic mount.

As in the case of the hydraulic top mount, all the data relative to the D-class input are one order of magnitude higher than in the case of a smooth road. Looking at the data shown in Table 5.7, it is possible to note that all the values are slightly higher than in the case of the quarter car model with the hydraulic top mount. Even though there is a really slight difference between the two models in these first attempts, the improvement is promising since the parameters relative to the hydraulic mount have to be optimized in order to achieve the best performance. In particular it is worth noting that the components of the RMS acceleration for the primary ride shown in Table 5.12 are the same as those relative to the configuration of the quarter car model with the hydraulic mount, while the only noticeable difference is in the secondary ride components. This result proves that the

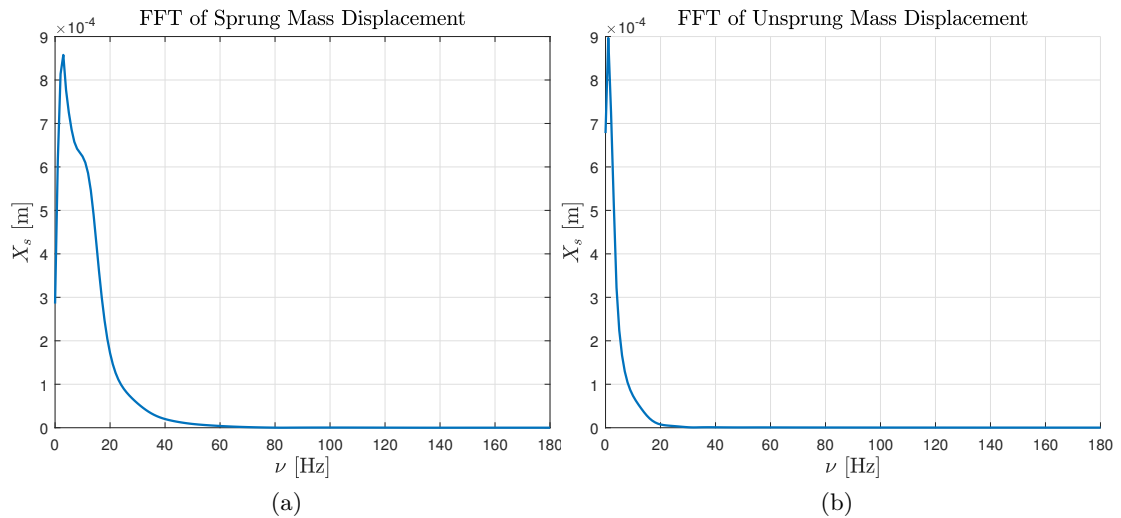


Figure 5.29: FFT plots of the sprung and unsprung mass displacement for the nonlinear quarter car model with the hydraulic mount due to single asperity input signal.

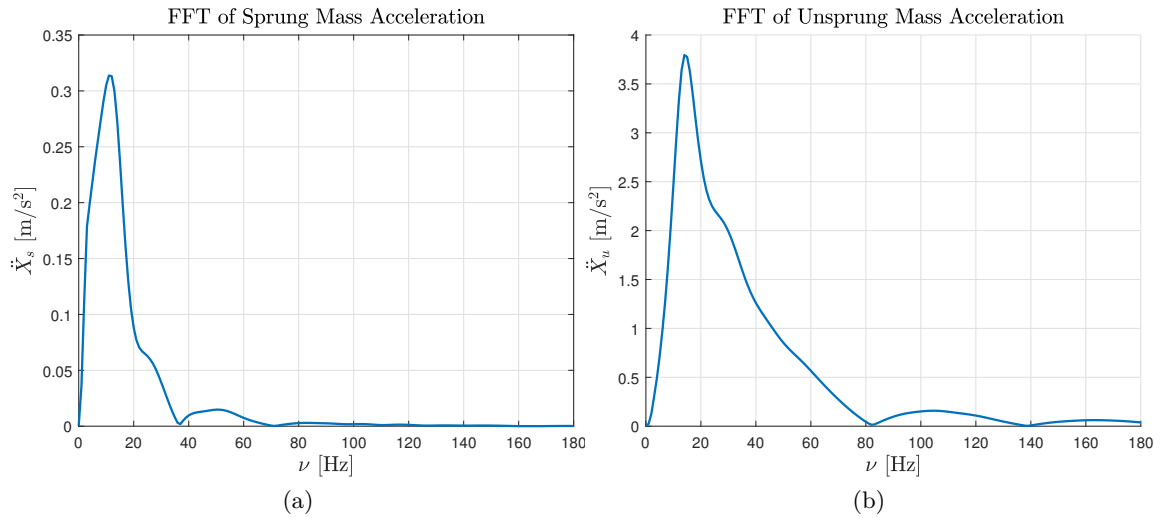


Figure 5.30: FFT plots of the sprung and unsprung mass acceleration for the nonlinear quarter car model with the hydraulic mount due to single asperity input signal.

top mount is effective in filtering the secondary ride frequency range.

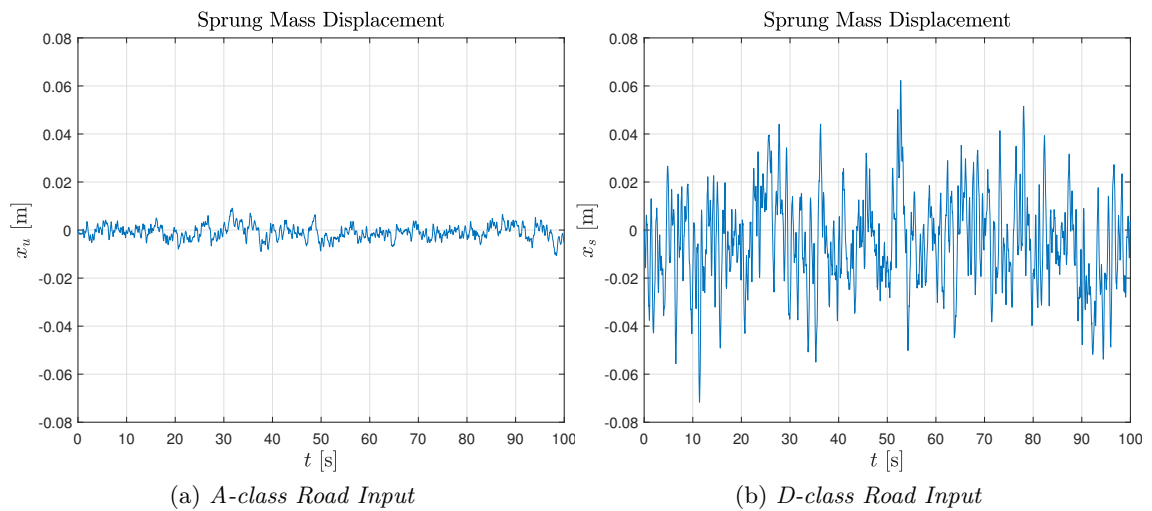


Figure 5.31: Sprung Mass Displacement in function of time for the quarter car model with the rubber top mount in the case of A-class road input (a) and D-class road input (b).

Time Simulation: Single Asperity Input

The displacement of sprung and unsprung masses due to the single asperity signal is shown in Figures 5.33 and 5.34.

The trend of both displacements is similar to that of the quarter car model with the hydraulic top mount, however it is possible to note that in this case the peaks are slightly higher for both sprung and unsprung masses. These conclusions can be drawn also looking at the acceleration, as the data shown in Tables 5.13 and 5.14, presenting RMS and range of acceleration. Acceleration values result to be higher than those of the quarter car

Table 5.11: RMS values and range of sprung and unsprung mass acceleration for the quarter car model with rubber top mount. Values in parentheses refer to the hydraulic top mount.

	$\ddot{x}_{s,RMS}$ (m/s ²)	$\ddot{x}_{s,range}$ (m/s ²)	$\ddot{x}_{u,RMS}$ (m/s ²)	$\ddot{x}_{u,range}$ (m/s ²)	$\eta_{rh,RMS}$ (-)
A-Class	0.288 (0.285)	2.18 (2.16)	0.917 (0.922)	6.88 (7.02)	0.0265 (0.0266)
D-Class	1.80 (1.79)	10.7 (10.6)	10.16 (10.15)	103.7 (104.11)	0.181 (0.183)

Table 5.12: Primary and secondary ride components of RMS sprung and unsprung mass acceleration for the quarter car model with the rubber top mount. Values in parentheses refers to the hydraulic top mount.

	0 – 5 Hz	5 – 20 Hz	0 – 5 Hz	5 – 20 Hz
	$\ddot{x}'_{s,RMS}$ (m/s ²)	$\ddot{x}''_{s,RMS}$ (m/s ²)	$\ddot{x}'_{u,RMS}$ (m/s ²)	$\ddot{x}''_{u,RMS}$ (m/s ²)
A-Class Input	0.217 (0.216)	0.188 (0.185)	0.271 (0.272)	0.862 (0.868)
D-Class Input	1.21 (1.21)	1.31 (1.29)	2.09 (2.09)	9.64 (9.65)

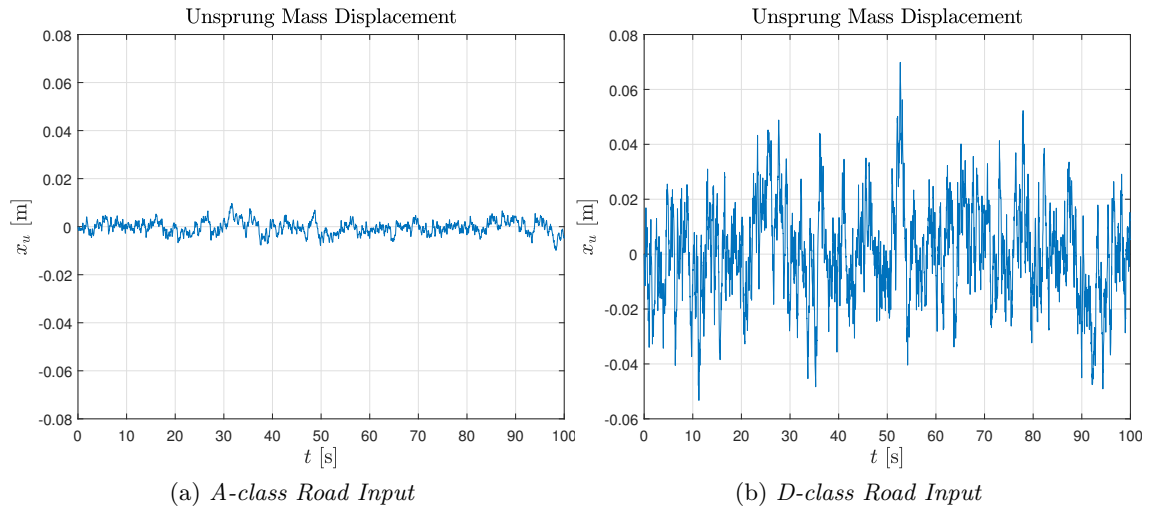


Figure 5.32: Unsprung Mass Displacement in function of time for the quarter car model with the rubber top mount in the case of A-class road input (a) and D-class road input (b).

model with the hydraulic top mount. This behaviour is likely due to the additional stage of damping present in the top mount model in the case of the hydraulic top mount.

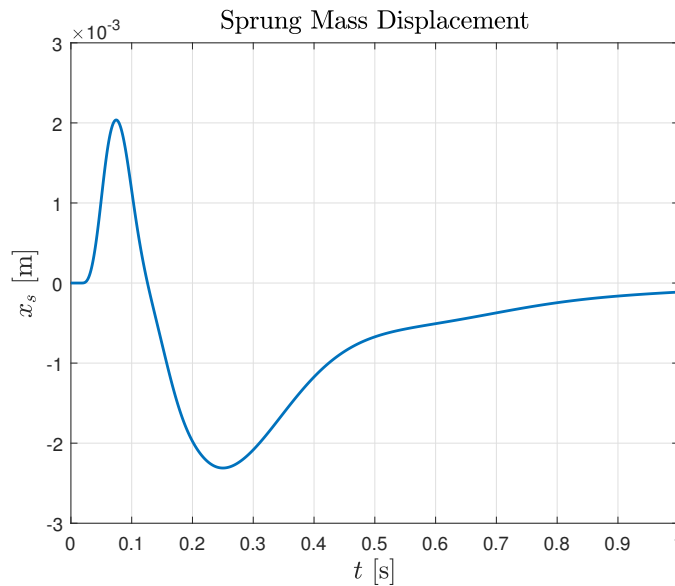


Figure 5.33: Displacement of the sprung mass due to single asperity input for the quarter car model with the rubber top mount.

Fast Fourier Transform: Random Road Inputs

The frequency response was analyzed through the fast FFT and all the relative plots are show in Figures 5.35a, 5.35b, 5.36a, 5.36b, 5.37a, 5.37b, 5.38a, 5.38b, in which the FFT of the hydraulic top mount model is used as reference. FFT plots for sprung and unsprung mass relative to the quarter car model with the rubber top mount are very similar to those relative to the quarter car model the hydraulic top mount and, the most important

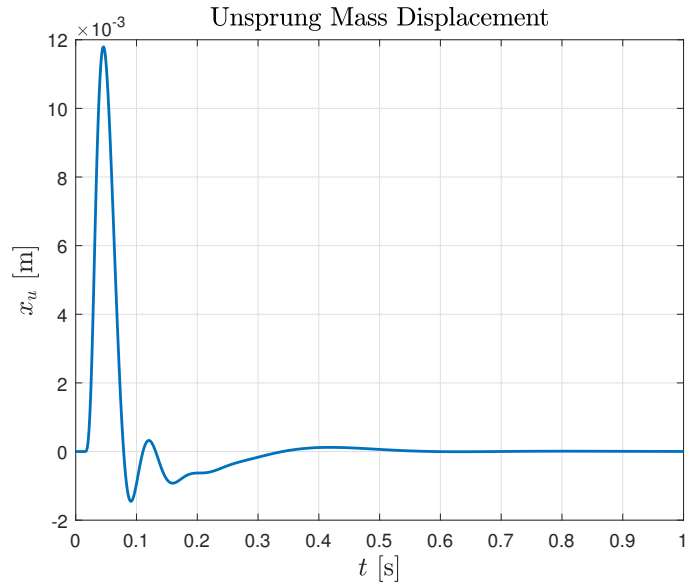


Figure 5.34: Displacement of the unsprung mass due to single asperity input for the quarter car model with the rubber top mount.

Table 5.13: RMS and range values for the acceleration of sprung and unsprung mass in the case of the nonlinear quarter car model with the rubber top mount due to a single asperity signal. Values in parentheses refer to the hydraulic top mount

$\ddot{x}_{s,RMS}$ m/s ²	$\ddot{x}_{u,RMS}$ m/s ²	$\ddot{x}_{s,range}$ m/s ²	$\ddot{x}_{u,range}$ m/s ²	η_{rh} (-)
0.741 (0.731)	10.82 (10.52)	6.76 (6.62)	134.9 (132.33)	0.136 (0.135)

frequency contributions occur between 0 and 15 Hz. The contributions beyond this value are practically null.

Table 5.14: Primary and secondary ride components of RMS sprung and unsprung mass acceleration of the quarter car model with the rubber top mount for single asperity input. Values in parentheses refer to the hydraulic top mount.

0 – 5 Hz	5 – 20 Hz	0 – 5 Hz	5 – 20 Hz
$\ddot{x}'_{s,RMS}$ (m/s ²)	$\ddot{x}''_{s,RMS}$ (m/s ²)	$\ddot{x}''_{u,RMS}$ (m/s ²)	$\ddot{x}''_{u,RMS}$ (m/s ²)
0.251 (0.258)	0.692 (0.669)	0.668 (0.657)	8.15 (7.98)

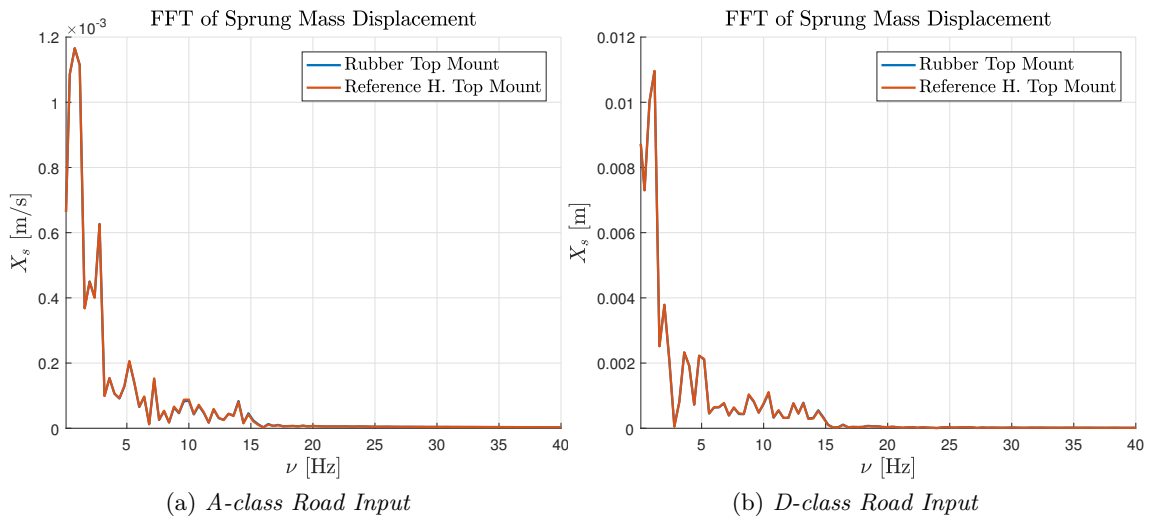


Figure 5.35: Fast Fourier Transform of the sprung mass displacement for the nonlinear quarter car model with the rubber top mount.

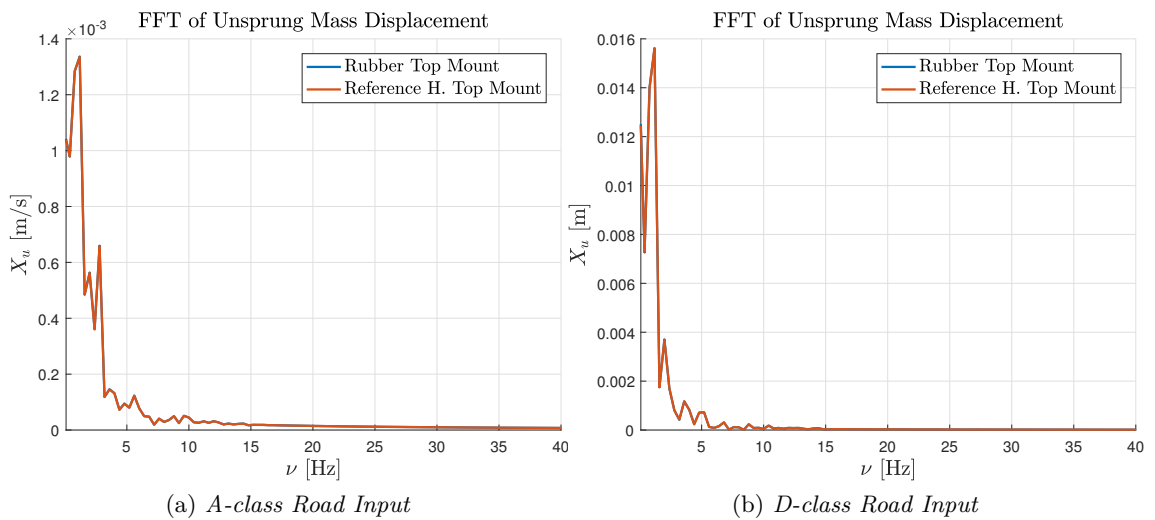


Figure 5.36: Fast Fourier Transform of the unsprung mass displacement for the nonlinear quarter car model with the rubber top mount.

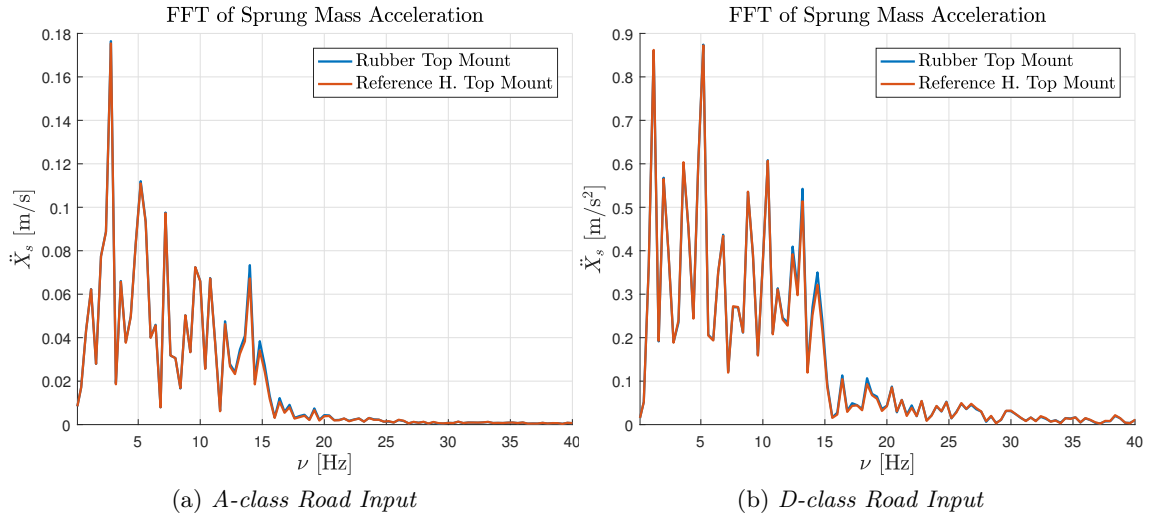


Figure 5.37: Fast Fourier Transform of the sprung mass acceleration for the nonlinear quarter car model with the rubber top mount.

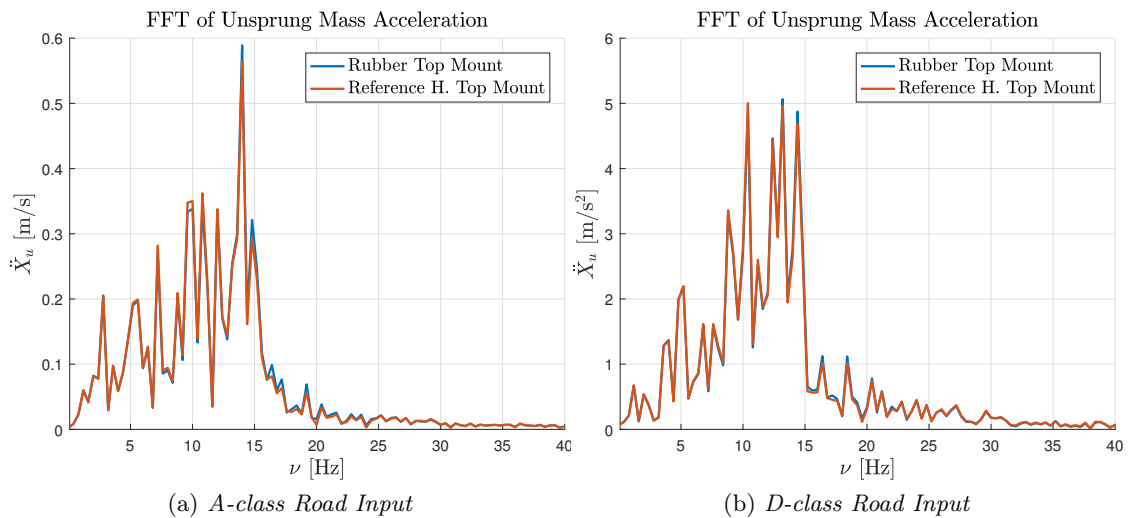


Figure 5.38: Fast Fourier Transform of the unsprung mass acceleration for the nonlinear quarter car model with the rubber top mount.

Fast Fourier Transform: Single Asperity Input

The last results coming from the simulations of the quarter car model in standard configurations are those relative to the frequency domain signals in the case of a single asperity input. In Figures 5.39a, 5.39b, 5.40a and 5.40b, FFT plots relative to the single asperity signal are displayed with reference to the hydraulic top mount case. Very few differences can be noticed with respect to the hydraulic top mount case. Therefore, similar conclusions to those drawn for the quarter car model with the hydraulic model can also be drawn for this configuration.

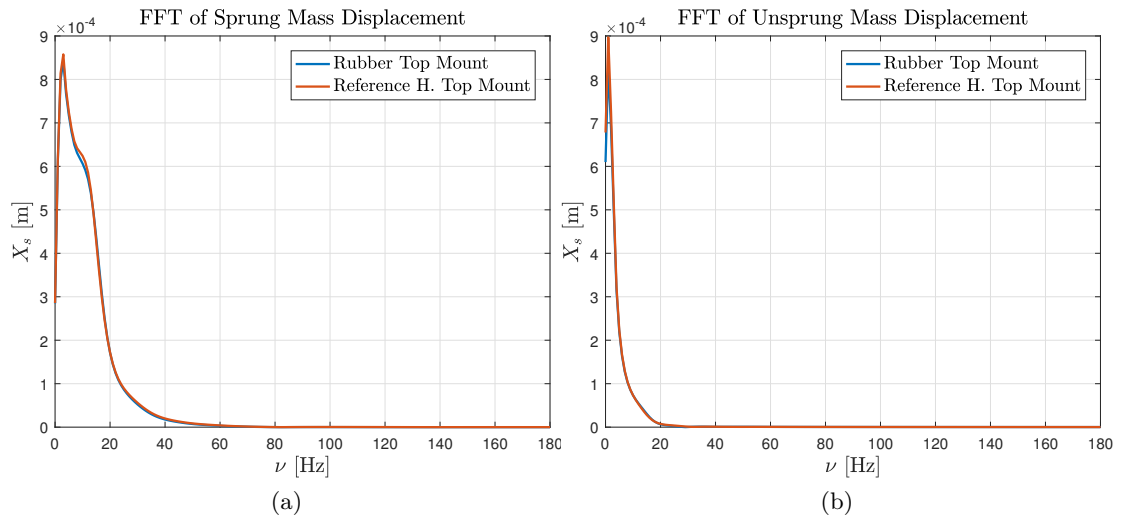


Figure 5.39: Fast Fourier Transform of sprung and unsprung mass displacement for the nonlinear quarter car model with the rubber top mount.

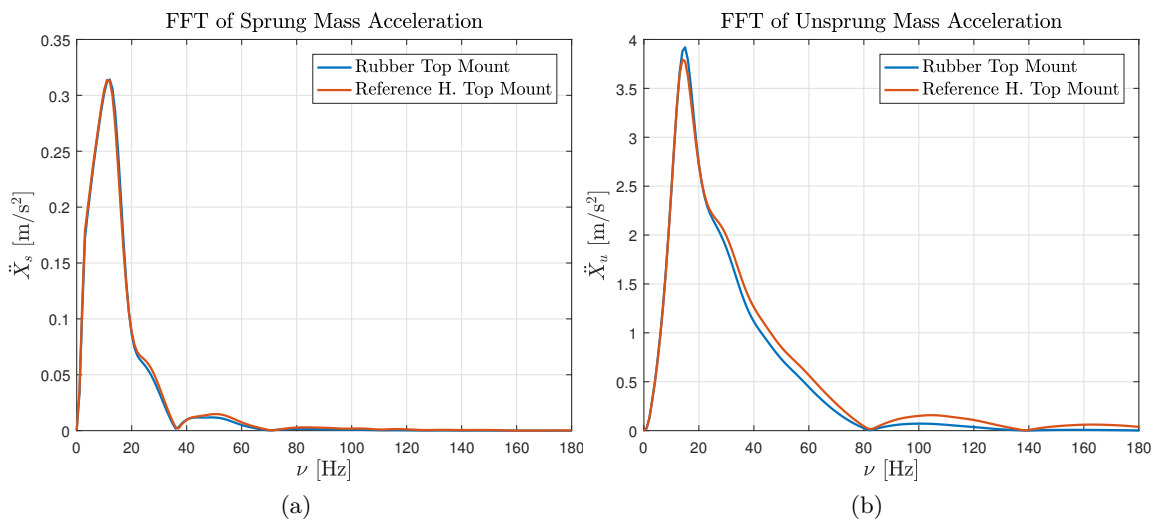


Figure 5.40: Fast Fourier Transform of sprung and unsprung mass displacement for the nonlinear quarter car model with the rubber top mount.

5.2.4 Quarter Car Model with the Hydraulic Top Mount in Series with the Suspension Strut

The last model that was developed, comprises the hydraulic top mount in series with the whole suspension strut. As was the case of the previous models, both time and frequency domain results were generated by means of the A-class and D-class random road inputs as well as by means of the single asperity input. This different configuration was tested in order to explore the synergy between different suspension elements. Because of the innovative nature of the present project, it is important to try to go out of the conventional schemes to look for any possibility of improvement.

Time Simulation: Random Roads Input Signal

In Figures 5.41a, 5.41b, 5.42a and 5.42b, time histories of sprung and unsprung mass displacement are presented. As expected, the A-Class input generated much smaller displacements and accelerations than the D-Class input. Nevertheless, it is worth noting that this configuration assures lower values of RMS acceleration for sprung mass and unsprung mass, not only with respect to the model comprising of the rubber top mount, but also with respect to the model with the hydraulic top mount in standard configuration. This can be seen in Tables 5.15 and 5.16.

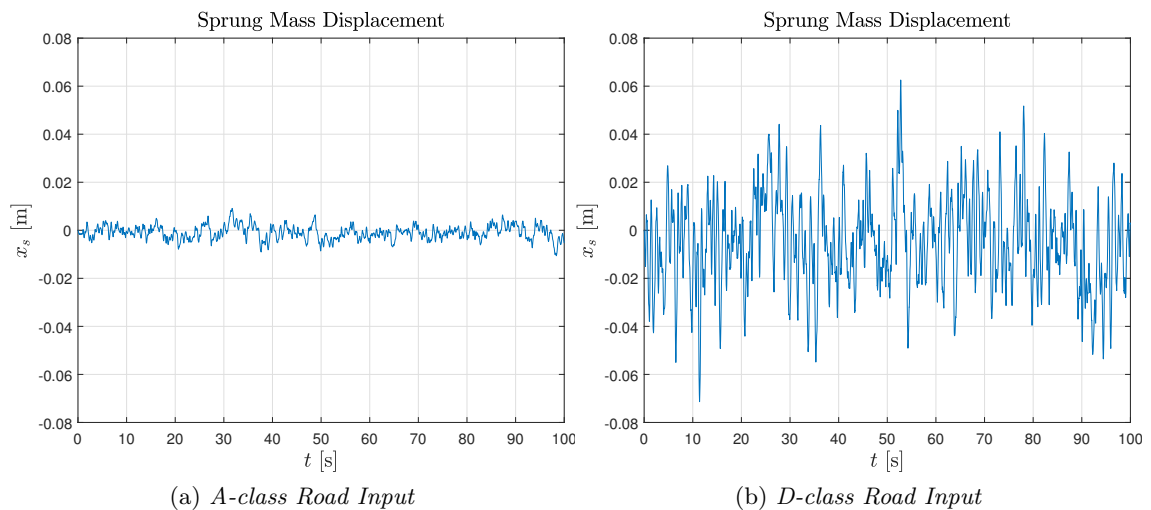


Figure 5.41: Sprung mass displacement in function of time for the quarter car model with the hydraulic top mount in series with the strut in the case of A-class road input (a) and D-class road input (b).

It is worth noting that this configuration for the quarter car model assures a higher degree of improvement with respect to both configurations seen in Sections 5.2.2 and 5.2.3 in the case of the sprung mass acceleration. In particular, considering D-class input, an improvement of 3.9 % and 4.5 % for the RMS sprung mass acceleration was recorded with respect to the hydraulic top mount in normal configuration and with respect to the rubber top mount. Moreover, the improvement is not restricted to the secondary ride, but

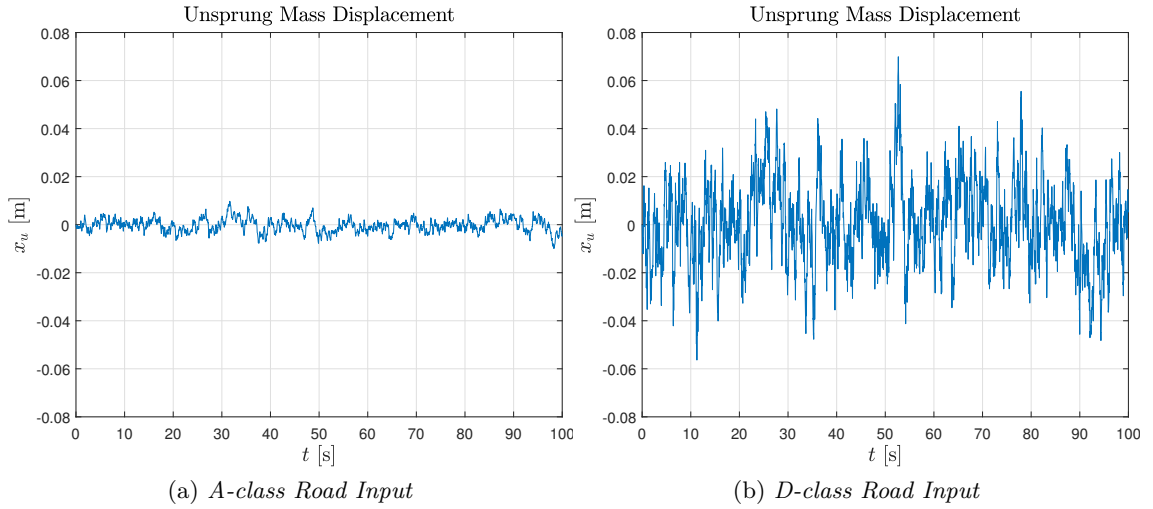


Figure 5.42: Unsprung mass displacement in function of time for the quarter car model with the hydraulic top mount in series with the strut in the case of A-class road input (a) and D-class road input (b).

Table 5.15: RMS values and range of sprung and unsprung mass acceleration for the quarter car model with the hydraulic top mount in series with the strut. Values in parentheses refer to standard configuration.

	$\ddot{x}_{s,RMS}$ (m/s ²)	$\ddot{x}_{s,range}$ (m/s ²)	$\ddot{x}_{u,RMS}$ (m/s ²)	$\ddot{x}_{u,range}$ (m/s ²)	$\eta_{rh,RMS}$ (-)
A-Class	0.272 (0.285)	2.04 (2.16)	0.972 (0.922)	7.40 (7.02)	0.0256 (0.0266)
D-Class	1.72 (1.79)	10.10 (10.65)	10.64 (10.15)	106.3 (104.11)	0.183 (0.183)

Table 5.16: RMS components of sprung and unsprung mass acceleration for the quarter car model with the hydraulic top mount in series with suspension strut. Values in parentheses refer to standard configuration.

	0 – 5 Hz	5 – 20 Hz	0 – 5 Hz	5 – 20 Hz
	$\ddot{x}'_{s,RMS}$ (m/s ²)	$\ddot{x}''_{s,RMS}$ (m/s ²)	$\ddot{x}'_{u,RMS}$ (m/s ²)	$\ddot{x}''_{u,RMS}$ (m/s ²)
A-Class Input	0.202 (0.216)	0.183 (0.185)	0.273 (0.272)	0.928 (0.868)
D-Class Input	1.14 (1.21)	1.26 (1.29)	2.11 (2.09)	10.23 (9.65)

a certain improvement can be appreciated in the primary ride as well. Conversely, the data relative to the unsprung mass shows a slight performance degradation; nevertheless

this is not a significant problem since only the sprung mass vibrations directly affect the vehicle occupants' experience.

Time Simulation: Single Asperity Input

Lastly, this configuration of the quarter car model was simulated with the single asperity input. In Figures 5.43 and 5.44, the displacement time histories of sprung and unsprung mass are reported, while Tables 5.17 and 5.18 contain the information about the RMS accelerations and road holding index.

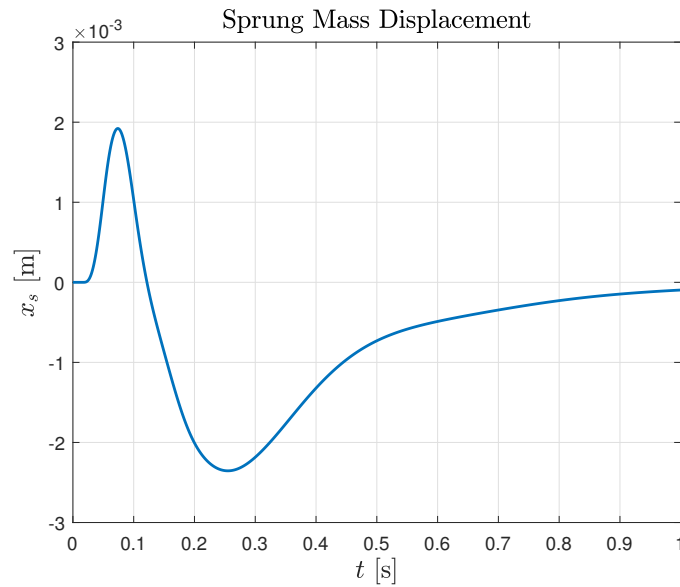


Figure 5.43: Displacement of the sprung mass due to single asperity input for the quarter car model with the hydraulic top mount in series with the strut.

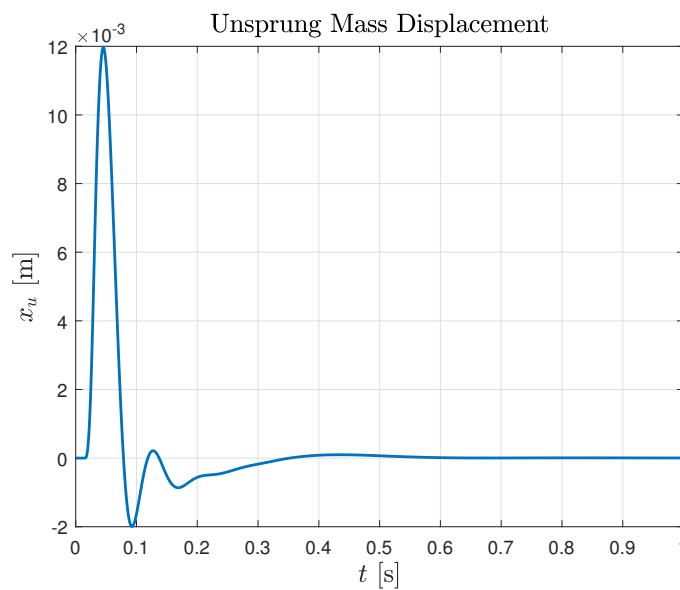


Figure 5.44: Displacement of the unsprung mass due to single asperity input for the quarter car model with the hydraulic top mount in series with the strut.

Table 5.17: RMS and range values for the acceleration of sprung and unsprung mass in the case of the nonlinear quarter car model with the hydraulic top mount in series with the strut due to a single asperity signal.

$\ddot{x}_{s,RMS}$ (m/s ²)	$\ddot{x}_{u,RMS}$ (m/s ²)	$\ddot{x}_{s,range}$ (m/s ²)	$\ddot{x}_{u,range}$ (m/s ²)
0.705 (0.731)	10.59 (10.52)	6.31 (6.62)	132.3 (132.3)

The data relative to the single asperity input, in accordance with those obtained by employing random road inputs highlights a general improvement in performance with respect to the other models. Furthermore, a lower value for the unsprung mass RMS acceleration was obtained despite the fact that both the components of RMS at the primary and secondary rides are higher. This strange behaviour can be attributed to an improvement given by the hydraulic top mount at higher frequencies: the primary and secondary ride components refer to a frequency range between 0 Hz and 20 Hz, while in the case of single asperity input, significant frequency contributions occur even at higher frequencies, as it was shown in Section 5.2.4.

Fast Fourier Transform: Random Road Inputs

The analysis of the frequency domain was made in the same way as it was for previous models, i. e., by using the FFT algorithm. Frequency domain plots are shown in Figures 5.45a, 5.45b, 5.46a, 5.46b, 5.47a, 5.47b, 5.48a and 5.48b. The FFT of the standard configuration of the hydraulic top mounts were used as a reference in this case as well. All the signals had similar as those discussed above, with a significantly high peak for both displacement at low frequency and a wider spectrum for the acceleration with a cutoff around 15 Hz. Moreover, the most important sprung mass acceleration contributions fall in the secondary ride region, while two different peaks at the primary and secondary rides were observed in the case of sprung mass displacement.

Table 5.18: Primary and secondary ride components of RMS of sprung and unsprung mass acceleration for the quarter car model with the hydraulic top mount in series with the strut. Values in parentheses refer to standard configuration.

	0 – 5 Hz	5 – 20 Hz	0 – 5 Hz	5 – 20 Hz
$\ddot{x}'_{s,RMS}$ (m/s ²)	$\ddot{x}''_{s,RMS}$ (m/s ²)	$\ddot{x}'_{u,RMS}$ (m/s ²)	$\ddot{x}''_{u,RMS}$ (m/s ²)	$\eta_{rh,RMS}$ (–)
0.239 (0.258)	0.614 (0.669)	0.651 (0.657)	8.11 (7.98)	0.137 (0.135)

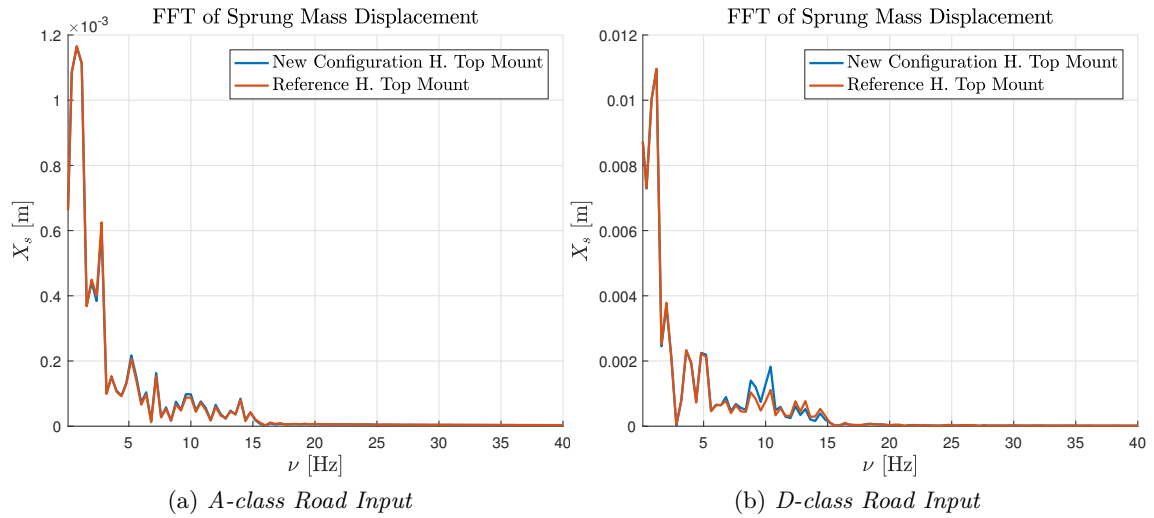


Figure 5.45: Fast Fourier Transform of the sprung mass displacement for the nonlinear quarter car model with hydraulic mount in series with the suspension strut.

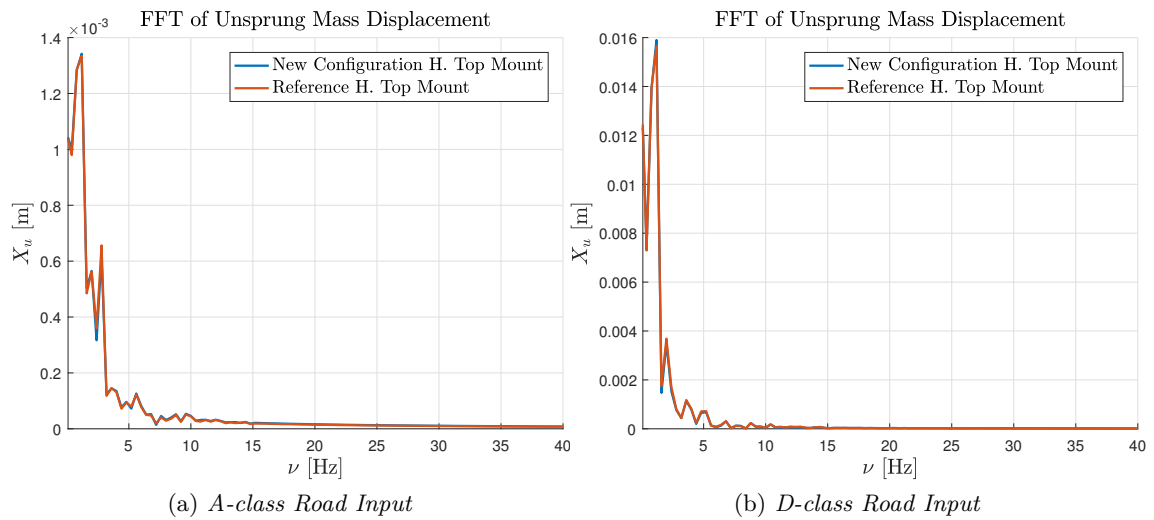


Figure 5.46: Fast Fourier Transform of the unsprung mass displacement for the nonlinear quarter car model with hydraulic mount in series with the suspension strut.

Fast Fourier Transform: Single Asperity Input

Figures 5.49a, 5.49b, 5.50a and 5.50b show the frequency domain data for the single asperity input. As was the case for the other quarter car models, the spectrum of the signal in the case of a single asperity input is wider than in the case of random inputs. This is especially true in the case of unsprung mass acceleration, which confirms that lower values of RMS components in the primary and secondary rides are caused by the contributions at frequencies higher than 20 Hz, in spite of the higher overall values. Additionally, a peak around 1 Hz can be easily noticed in the displacement plots, while both acceleration plots have a peak in the secondary ride range around 12 Hz.

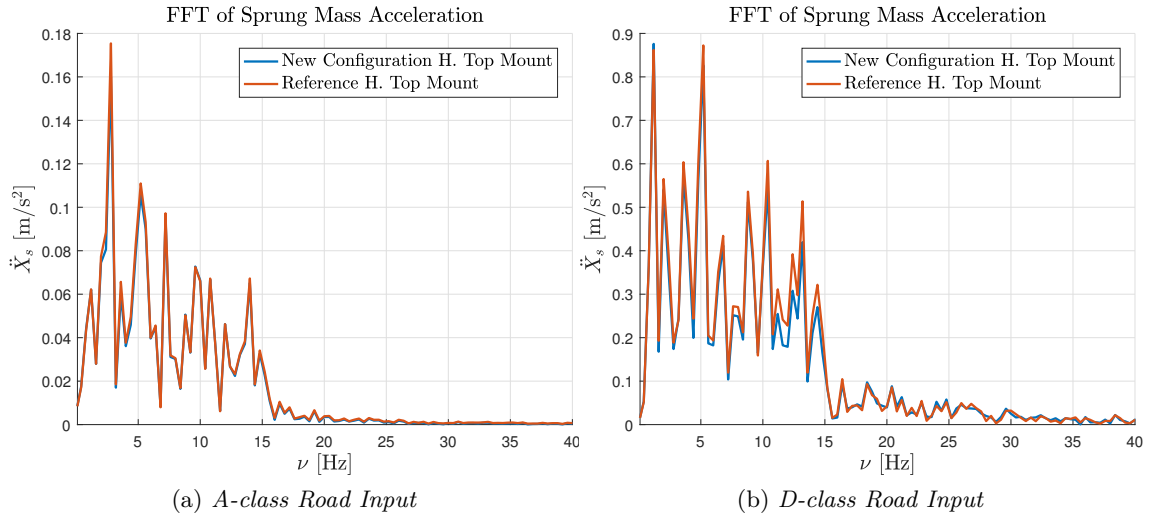


Figure 5.47: Fast Fourier Transform of the sprung mass acceleration for the nonlinear quarter car model with hydraulic mount in series with the suspension strut..

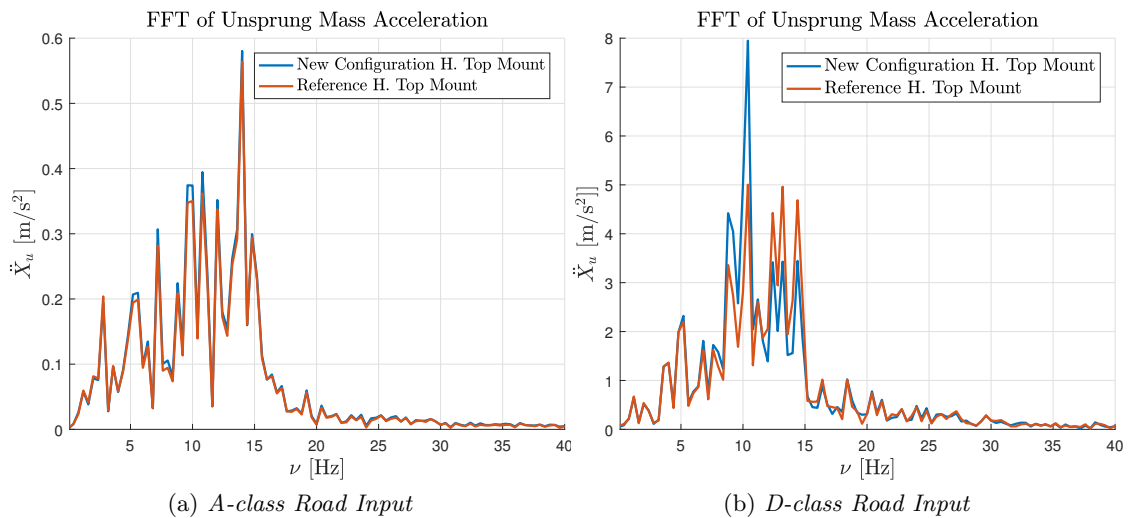


Figure 5.48: Fast Fourier Transform of the unsprung mass acceleration for the nonlinear quarter car model with hydraulic mount in series with the suspension strut.

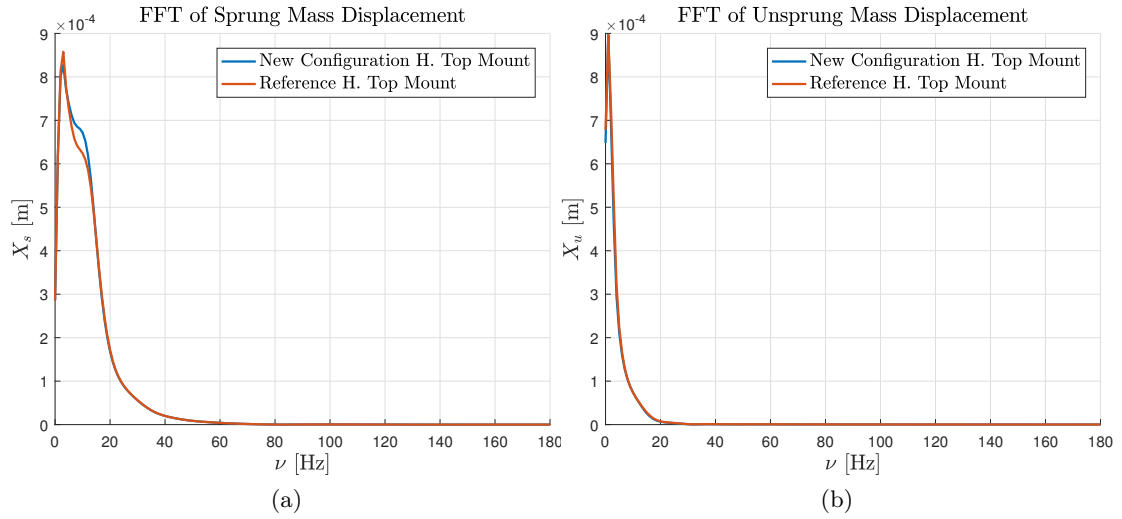


Figure 5.49: Fast Fourier Transform of sprung and unsprung mass displacement for the nonlinear quarter car model with hydraulic mount in series with the suspension strut.

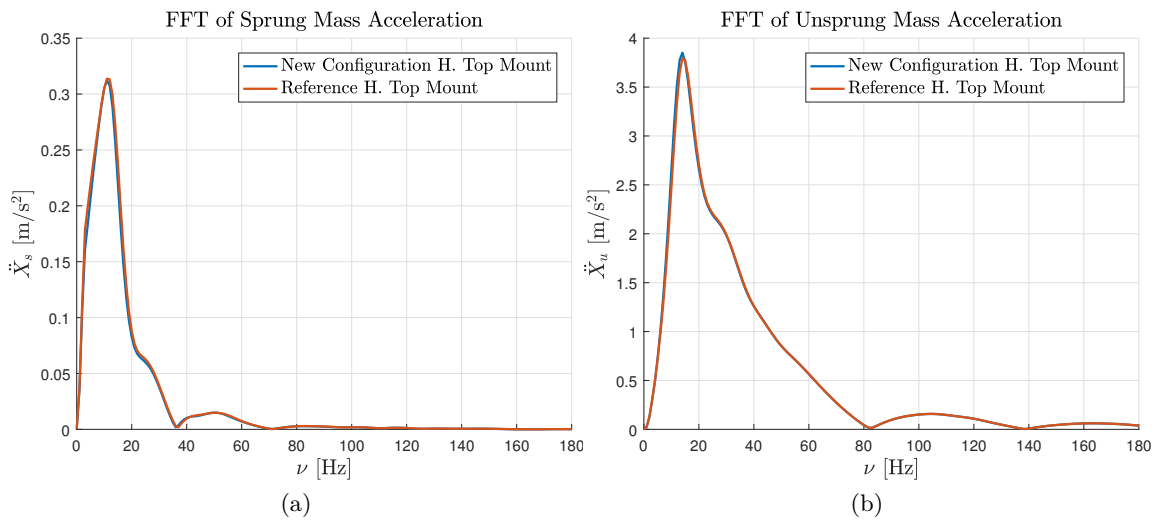


Figure 5.50: Fast Fourier Transform of sprung and unsprung mass acceleration for the nonlinear quarter car model with hydraulic mount in series with the suspension strut.

5.3 Concluding Remarks

In this chapter, all the most relevant results given by the simulations have been shown. The comparison between data relative to the hydraulic top mount and the data relative to the rubber top mount underlined that the employment of the new device introduces a benefit in terms of vertical acceleration, although in many cases it is difficult to appreciate.

However, it is important to keep in mind that all the data about hydraulic top mounts is relative to the baseline parameters: no kind of optimization was made in this phase. The basis for the optimization work is discussed in Chapter 6, in which a sensitivity analysis is discussed considering the standard configuration for the quarter car model with the hydraulic top mount, although a deeper insight into this topic is out of the scope of the present project.

Design of Experiments and Sensitivity Analysis

The employment of the Design of Experiments (DOE) tool in relation to the hydraulic top mount model is aimed at the individuation of the most influential parameters for the RMS acceleration of sprung and unsprung mass. The advantage of this methodology lies in the ability to perform different tests by changing more than one parameter at a time. In this way, potential interactions can be also taken into account; however, the completion of a full experimental plan can be time-consuming.

6.1 Design of Experiments Methodology

Any different phenomena is influenced by a certain number of factors. In order to discern among their significance and impact on the response, it is necessary to perform different experiments under different conditions. The DOE allows to efficiently create an experimental plan to perform different tests and analyze their results [28]. Indeed, this tool allows for the set up of an experiments plan in which more than one factor at time vary and then to analyze the significance of each single factor and interaction by means of the Analysis of Variances (ANOVA).

In the scope of the present project, the DOE method with full factorial plan has been applied to the parameters of the secondary rubber and hydraulic component of the hydraulic top mount. In particular, their effect on the RMS value of sprung and unsprung mass acceleration were evaluated, which correspond to the responses of the experiments. In other words, the factors are the parameters k_2 , c_2 , c_3 , and m_3 , while the responses are $\ddot{x}_{s,RMS}$ and $\ddot{x}_{u,RMS}$ since it was found that the top mount contributes most to the secondary ride frequency range.

Since the experiments are only different simulations of the model, and model differential

Table 6.1: Values of each Factor at different levels in the DOE plan.

Level	c_2	k_2	c_3	m_3
(-)	(Ns/mm)	(N/mm)	(Ns/mm)	(kg)
1	0.02	2	0.12	1
2	0.08	8	0.40	4
3	0.14	14	0.84	7
4	0.20	20	1.20	10
5	0.65	65	3.90	32.5
6	1.10	110	6.60	55
7	1.55	155	9.30	77.5
8	2.00	200	12	100

equations directly depend on the aforementioned factors, it was expected that most of the factors and also some interactions would have been significant, but, in this case, it was necessary to understand which factors had the highest influence on the response and how each factor influenced the output. In this way, the physical characteristics of the top mount bringing a comfort performance improvement could be analyzed.

The number of levels for each factor were chosen as a trade-off between accuracy and simulation time. The number of experiments depends on the number of factors (n) and on the levels number (k) according to the expression k^n in case of a full factorial plan. Therefore, the amount of tests rapidly increases as the number of levels increases. In this project, 8 levels were selected and, because of the 4 factors, 4096 experiments were necessary to complete the DOE plan. The values of each level was chosen using the reference value as the middle value (level 4), and then each factor was made to increase and decrease to generate each level. Thus, the lowest value was one order of magnitude lower than the reference and the highest was one order of magnitude higher than the reference. In Table 6.1, the values of each factor at each different level are shown.

Once the DOE plan had been created, the nonlinear quarter car model with the hydraulic top mount was simulated in time using the D-class road input in order to have considerable RMS values of acceleration that made the successive analysis easier. Only one replicate for each test was performed.

6.2 Analysis of Variances and Percentages of Contribution

The Analysis of Variances (ANOVA) is a tool aimed at assessing the variation of the output of the DOE in relation to the variation of the input factors or interactions. Once the response of the DOE is known, the effect of any single factor or interaction has to be analysed. Therefore, for each factor and interaction level, the mean between the corresponding value of the response is evaluated [29]. In order to perform the ANOVA on the above DOE, MiniTab[®] was used. The elements taken into account in the ANOVA are the

single factors and the second level interactions.

As it has been affirmed, 8 levels for each factor were selected, then each factorial mean was evaluated among 512 different values, obtaining 8 different means. Then, 64 different combinations were individuated among the levels of two factors, therefore each one of the interaction means has been evaluated between 64 different response values. Similarly, 512 means were calculated for the third order interactions. Once the mean values corresponding to each single factor and interaction level had been evaluated, the variance between the different mean values of the response at each level was calculated.

The variance of a set of data gives information about the variability on the set itself. In this case, it gives information about the variance caused by each single factor or interaction. However, the variance itself is not enough to make any sort of conclusion on factors and interactions: it is also necessary to evaluate the so-called “error variance” (σ_{err}^2), which is the variance of the response caused by all those factors and interactions not included in the ANOVA. Since the ANOVA performed in this project has only one replicate, σ_{err}^2 corresponds to the variance caused by the fourth order interactions that were not considered significant *a priori*.

The following step for the ANOVA is the evaluation of the F-ratios (φ) for each factor and interaction. They are the reference values in the understanding of the significance of each factor. It is evaluated by means of the formula shown in Equation (6.1) and they are compared to a limit value which depends on the chosen confidence level and on the degrees of freedom of the denominator and the numerator of Equation (6.1) [29].

$$\varphi_y = \frac{\sigma_y}{\sigma_{err}} \quad (6.1)$$

The confidence level determines the risk of error of considering a factor not statistically significant, while the degrees of freedom correspond to the number of values of a set of data necessary in order to reconstruct the set itself [29].

The degrees of freedom of the factor’s variance is equal to the number of values used to calculate the variance decreased by one. Instead, in the case of interactions, the number of degrees of freedom is equal to the product between the degrees of freedom of the factors comprising the interaction. Finally, the degrees of freedom of the error is evaluated as the difference between the total number of degrees of freedom, which is given by the total number of experiments decreased by one, and the sum of the degrees of freedom of the factors and the interactions included in the ANOVA.

For the present project, each factor has 7 degrees of freedom while each second order interaction counts 49 degrees of freedom and each third order interaction has 343 degrees of freedom. Since 4096 experiments were performed and the total number of the degrees of freedom is 4095, the number of degrees of freedom of the error is 2401.

By knowing the degrees of freedom of each factor and interaction, it is possible to evaluate the limit F-Ratio (φ_{lim}) at 95% of a two-sided confidence level. These values are shown in Table 6.2.

Table 6.2: Factors and interactions limit value for the F-Ratios at 95% confidence level.

$\varphi_{lim,f}$	$\varphi_{lim,i2}$	$\varphi_{lim,i3}$
(-)	(-)	(-)
2.01	1.35	1.00

The percentages of contribution method is aimed at estimating the sensitivity of the output of a DOE plan due to a particular factor or interaction. The reference parameter in order to perform this analysis is the Sum of Squares (Q), which can be evaluated, in the scope of the ANOVA, as the product between the degrees of freedom and the variance, but it is thoretically defined as the sum of the squared difference between each element of a certain set of data and its mean as it is shown in Equation (6.2). Its importance derives from the ability to understand the different impact of each different factors on the model [29].

$$Q_y = \sum_{i=0}^n (y - \bar{y})^2 \quad (6.2)$$

Since the sum between factors, interactions and error sums of squares (Q_y , Q_{y-z} and Q_{err}) is equal to the total sum of squares (Q_{tot}), an estimation of the percentages of contribution can be given by the ratio between the sum of squares of each single factor and interactions and the total sum of squares. However, to have better results, it is convenient to employ the corrected Sum of Squares after having performed the “pooling” operation. Pooling is performed by including the variance of factors that are not statistically significant into the error variance (σ_{err}^2). Therefore, the variance (σ_{err}^2), the sum of squares (Q'_{err}) and the degrees of freedom of the error after pooling (df'_{err}) vary according to Equations (6.3), (6.4) and (6.5), where the degrees of freedom and the sum of squares of factors that are not statistically significant are defined (df_{ns} and Q_{ns}) as well as the degrees of freedom and the sum of squares of the error (df_{err} and Q_{err}).

$$df'_{err} = df_{err} + df_{ns} \quad (6.3)$$

$$Q'_{err} = Q_{err} + Q_{ns} \quad (6.4)$$

$$\sigma_{err}^2 = \frac{Q'_{err}}{df'_{err}} \quad (6.5)$$

In order to evaluate the corrected sum of squares (\hat{Q}_y), it is necessary to eliminate the variability caused by the error from the sum of squares. Formulas to evaluate the corrected sum of squares of the factors and of the error (\hat{Q}_{err}) are presented in Equation

(6.6), (6.7).

$$\hat{Q}_y = Q_y - df_y \cdot \sigma_{err}^2 \quad (6.6)$$

$$\hat{Q}_{err} = Q_{err} + \sum (df_{ns}) \cdot \sigma_{err}^2 \quad (6.7)$$

6.3 ANOVA and Percentages of Contribution Results

The output of the ANOVA is summarized in Tables 6.3 and 6.4, showing the degrees of freedom (df), sum of squares (Q), variance (σ) and F-Ratio (φ) for each factor and interaction. Another relevant output of the ANOVA is represented by the main effects plots, which are shown in Figures 6.1a, 6.1b, 6.2a, 6.2b, 6.3a, 6.3b, 6.4a and 6.4b, and by interaction plots, presented in 6.5a, 6.5b, 6.6a, 6.6b, 6.7a, 6.7b, 6.8a, 6.8b, 6.9a, 6.9b, 6.10a and 6.10b.

These plots show the variability of the output according to the different level of each factor and also the nature of the interactions between different factors. In particular, if the different lines of the interaction plots are parallel, interactions between two factors do not occur. However, if they cross or diverge, a negative or positive interaction occurs, respectively [29]. The effect and interaction plots also show how the variation of a parameter affects the output.

Statistical practice requires that all those factors or interactions whose F-Ratio (φ) is higher than the corresponding limit value (φ_{lim}) are considered as significant with the established confidence level, otherwise no conclusion can be made. In this particular case, all the factors would have been considered significant, as expected, since the experiments are simulations of a model built on the same parameters considered as factors and interactions. For this reason, the significance of a factor or interaction is not really the most relevant result in this case; the most explanatory result of the DOE is the relative importance of factors and interactions. The F-Ratios shown in Tables 6.3 and 6.4 allow one to hypothesize which are the most important factors. For both outputs, F-Ratios of k_2 , m_3 and c_3 are higher than those of the factor c_2 and the interactions. Referring to the interactions, only those between c_3 and m_3 in the case of $\ddot{x}_{u,RMS}$ and between k_2 and c_3 actually have a role in the variability of the relative outputs, but in both cases their contribution seems to be smaller than the single factors k_2 and m_3 . Nevertheless, the analysis performed through the percentages of contribution method gives a more complete picture.

These results are in accordance with the information given by effects and interaction plots, which show how the variation of c_2 only causes a very subtle variation on both outputs. The only relevant interactions are: the second order interactions $c_3 - m_3$ and $k_2 - c_3$ namely for $\ddot{x}'_{u,RMS}$ and $\ddot{x}'_{s,RMS}$ and the third order interactions $k_2 - c_3 - m_3$ for both outputs. The ANOVA states that all the analyzed factors are relevant, however it is worth noting that most of them have little effect on the output. For this reason, it is

possible to consider the high importance factor as an initial approximation. The weight of any factor or interaction of the model can be estimated through the percentages of contribution analysis.

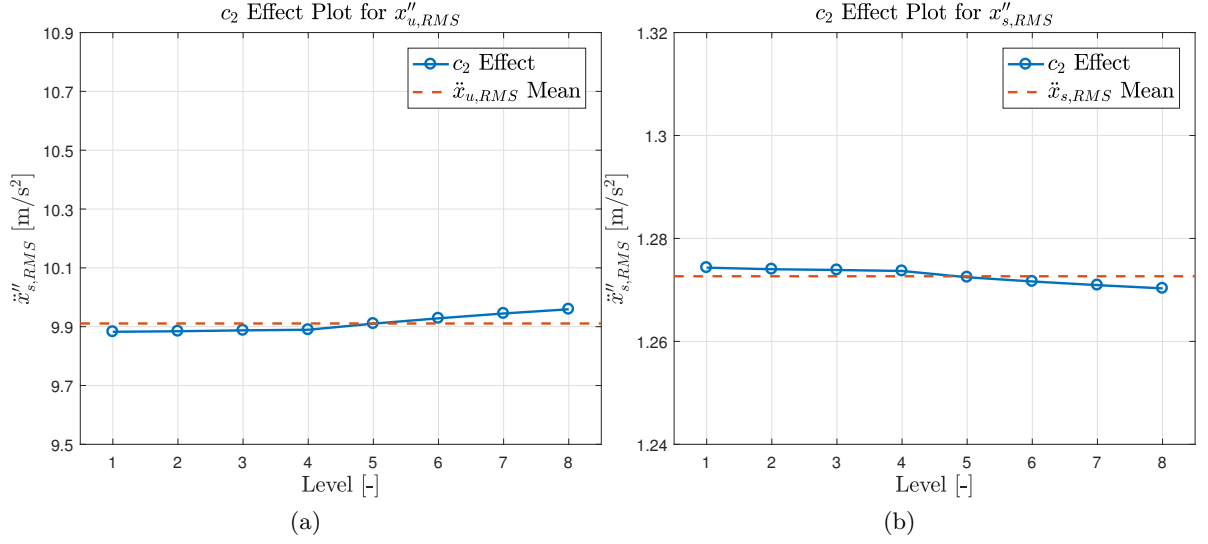


Figure 6.1: Effect of factor c_2 on the variation of $\ddot{x}_{u,RMS}$ and $\ddot{x}_{s,RMS}$.

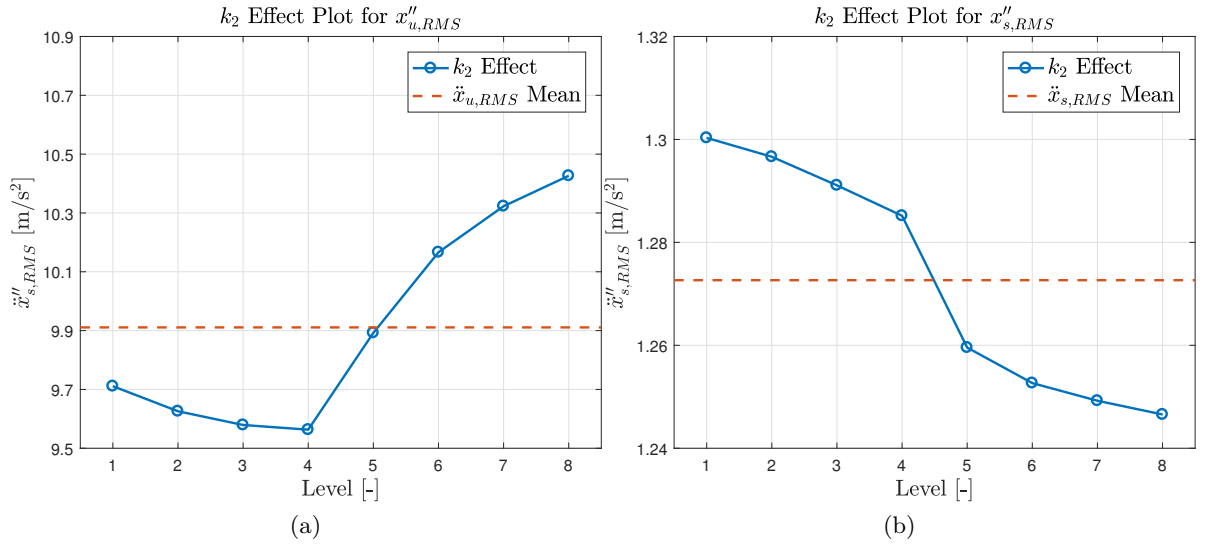


Figure 6.2: Effect of factor k_2 on the variation of $\ddot{x}_{u,RMS}$ and $\ddot{x}_{s,RMS}$.

Table 6.3: ANOVA summary table for $\ddot{x}'_{u,RMS}$.

Source	DoF (<i>df</i>) (-)	Sum of Squares (<i>Q</i>) $((m/s^2)^2)$	Variance (σ^2) $((m/s^2)^2)$	F-Ratio (φ) (-)
Model	1694	1401.25	0.8272	679.46
Factors	28	736.65	26.309	21 610.47
	c_2	3.23	0.4609	378.58
	k_2	436.90	62.414	51 267.65
	c_3	239.36	34.194	28 087.45
	m_3	57.17	8.166	6708.17
2-Way Interactions	294	446.90	1.516	103.15
	$c_2 - k_2$	6.15	0.1256	103.15
	$c_2 - c_3$	0.21	0.0042	3.49
	$c_2 - m_3$	0.37	0.0076	6.27
	$k_2 - c_3$	184.43	3.764	3091.76
	$k_2 - m_3$	95.23	1.943	1596.37
	$c_3 - m_3$	160.43	3.274	2689.39
3-Way Interactions	1372	217.77	0.1587	130.38
	$c_2 - k_2 - c_3$	1.30	0.0038	3.11
	$c_2 - k_2 - m_3$	1.53	0.0045	3.67
	$c_2 - c_3 - m_3$	0.97	0.0028	2.32
	$k_2 - c_3 - m_3$	213.96	0.6238	512.40
Error	2401	2.92	0.0012	
Total	4095	1404.17		

Table 6.4: ANOVA summary table for $\ddot{x}'_{s,RMS}$.

Source	DoF (<i>df</i>) (-)	Sum of Squares (<i>Q</i>) ((m/s ²) ²)	Variance (σ^2) ((m/s ²) ²)	F-Ratio (φ) (-)
Model	1694	4.002	2.362×10^{-3}	6.930×10^2
Factors	28	2.519	8.998×10^{-2}	3.590×10^4
c_2	7	8.57×10^{-3}	1.224×10^{-3}	3.590×10^2
k_2	7	1.862	2.660×10^{-1}	7.8024×10^4
c_3	7	1.256×10^{-1}	1.794×10^{-2}	5.264×10^3
m_3	7	5.235×10^{-1}	7.478×10^{-2}	2.1938×10^4
2-Way Interactions	294	1.178	4.007×10^{-3}	1.1755×10^3
$c_2 - k_2$	49	2.30×10^{-2}	4.70×10^{-4}	1.6025×10^2
$c_2 - c_3$	49	8.4×10^{-4}	1.700×10^{-5}	5.00
$c_2 - m_3$	49	4.41×10^{-3}	9.0×10^{-5}	2.642×10^1
$k_2 - c_3$	49	2.04×10^{-1}	4.174×10^{-3}	1.2244×10^3
$k_2 - m_3$	49	4.516×10^{-1}	9.217×10^{-3}	2.7039×10^3
$c_3 - m_3$	49	4.937×10^{-1}	1.008×10^{-2}	2.9555×10^3
3-Way Interactions	1372	4.937×10^{-1}	1.008×10^{-4}	2.9555×10^1
$c_2 - k_2 - c_3$	3432.38×10^{-3}	7	7×10^{-6}	2.03
$c_2 - k_2 - m_3$	343	6.95×10^{-3}	2.0×10^{-5}	5.94
$c_2 - c_3 - m_3$	343	4.10×10^{-3}	1.2×10^{-5}	3.50
$k_2 - c_3 - m_3$	343	2.909×10^{-1}	8.48×10^{-4}	2.4882×10^2
Error	2401	8.18×10^{-3}	3×10^{-6}	
Total	4095	4.010		

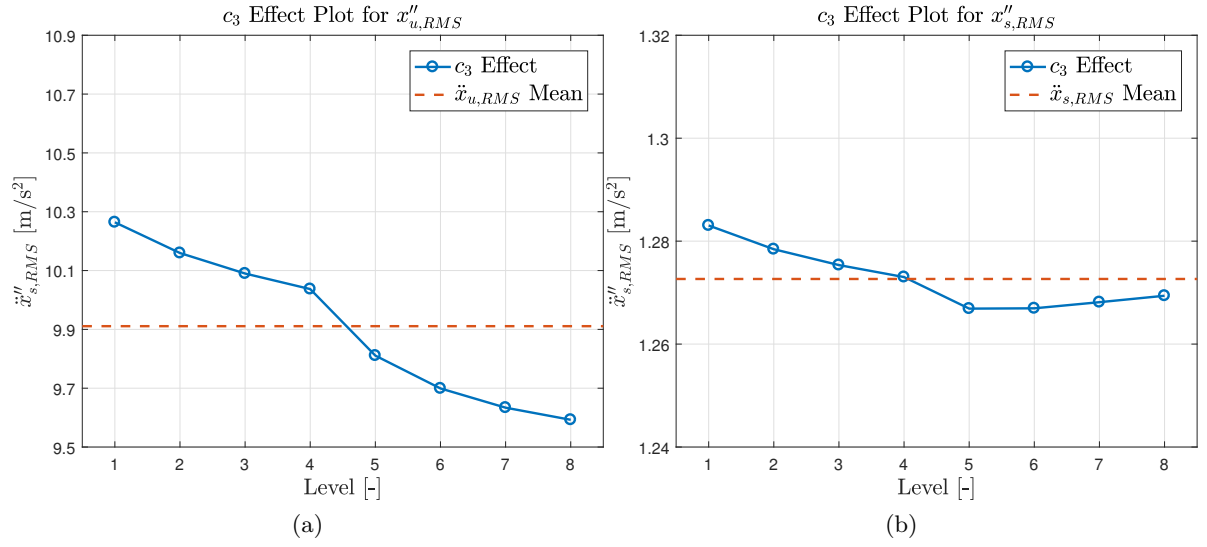


Figure 6.3: Effect of factor c_3 on the variation of $\ddot{x}_{u,RMS}$ and $\ddot{x}_{s,RMS}$.

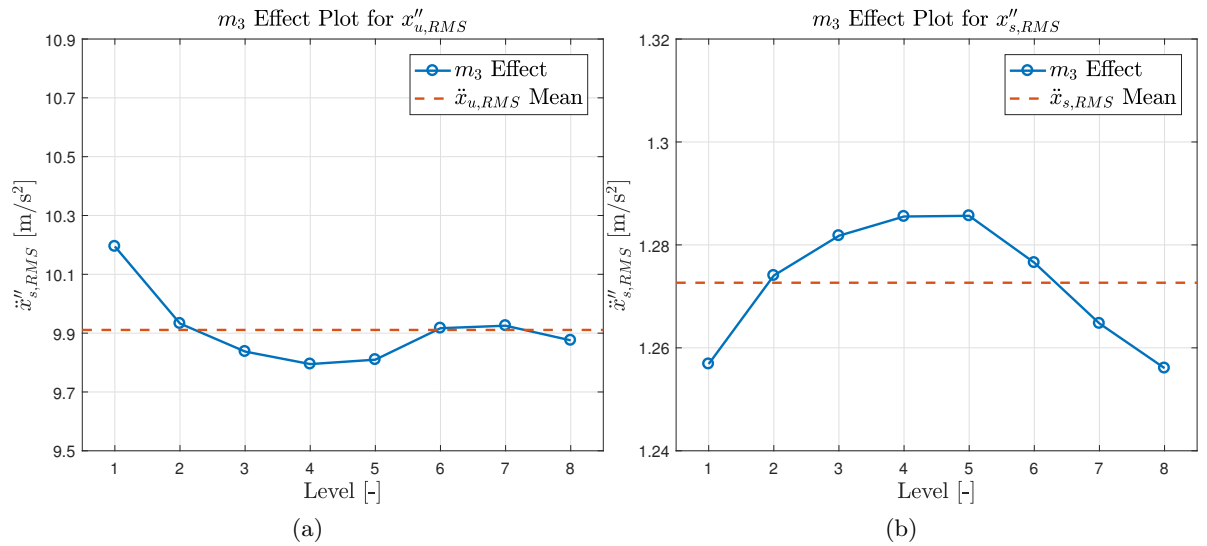


Figure 6.4: Effect of factor m_3 on the variation of $\ddot{x}_{u,RMS}$ and $\ddot{x}_{s,RMS}$.

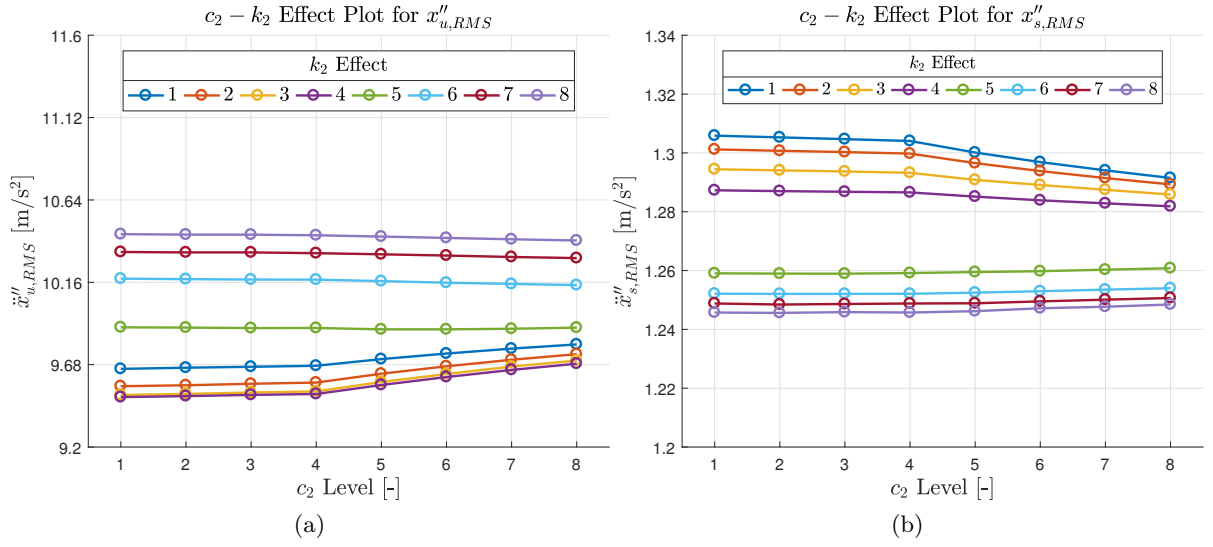


Figure 6.5: $c_2 - k_2$ interaction plots for $\ddot{x}_{u,RMS}$ and $\ddot{x}_{s,RMS}$

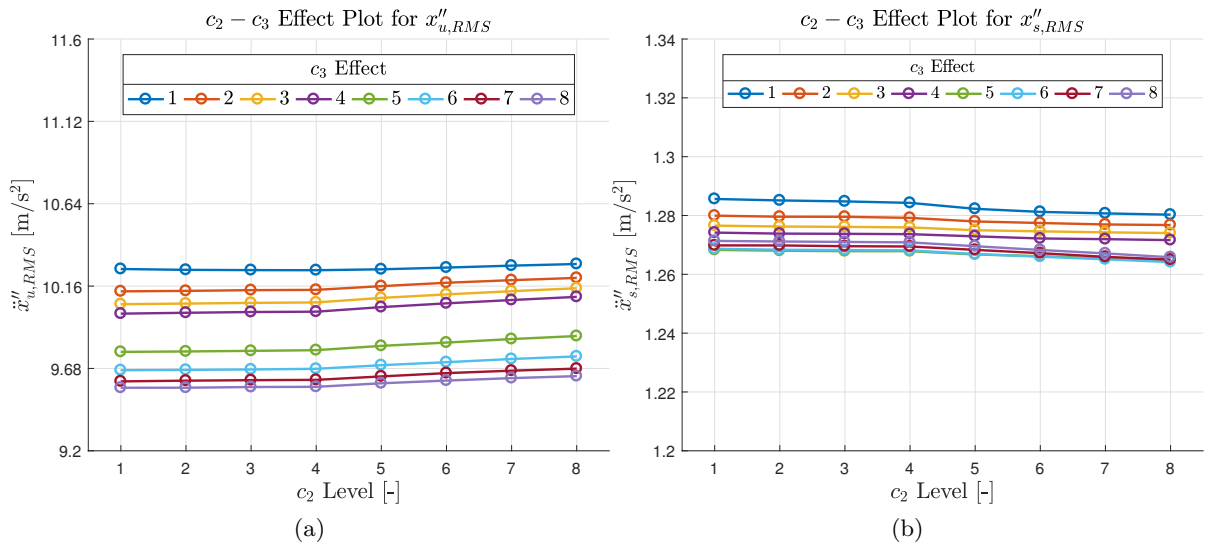


Figure 6.6: $c_2 - c_3$ interaction plots for $\ddot{x}_{u,RMS}$ and $\ddot{x}_{s,RMS}$

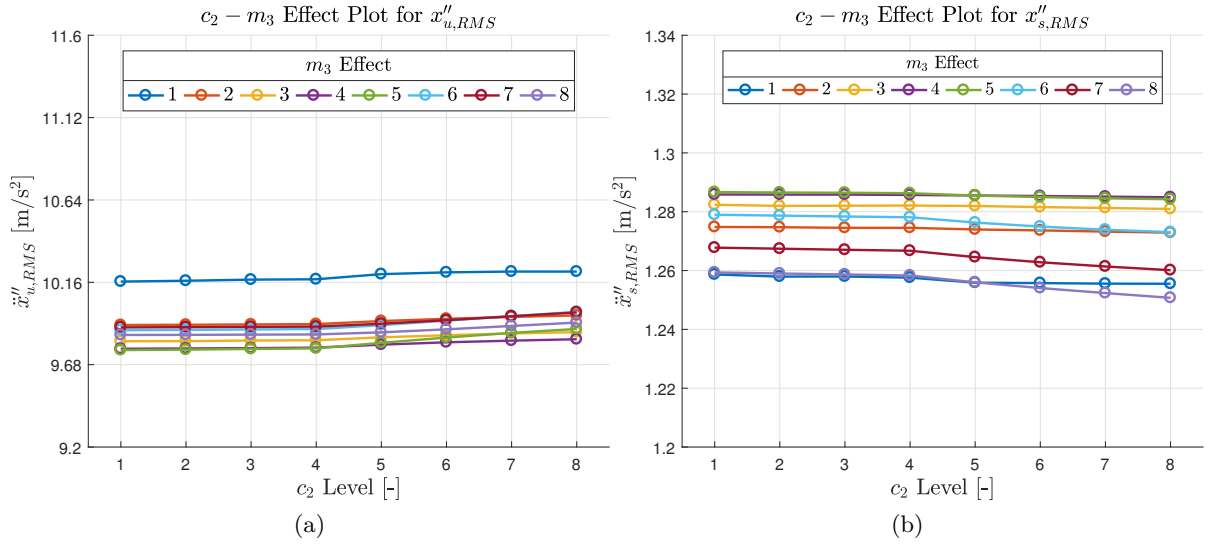


Figure 6.7: $c_2 - m_3$ interaction plots for $\ddot{x}_{u,RMS}$ and $\ddot{x}_{s,RMS}$

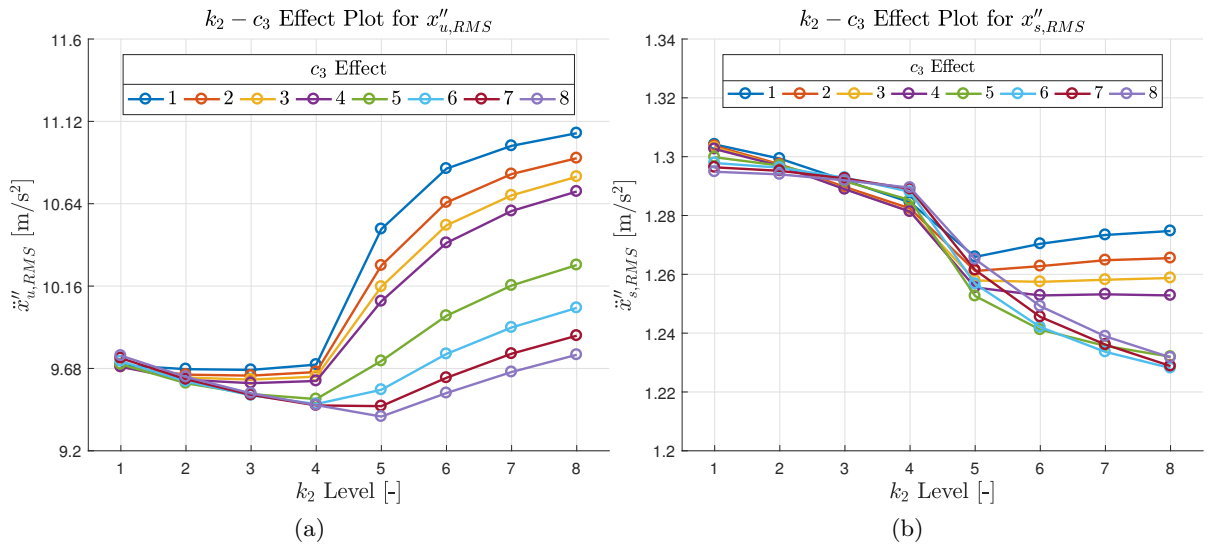


Figure 6.8: $k_2 - c_3$ interaction plots for $\ddot{x}_{u,RMS}$ and $\ddot{x}_{s,RMS}$

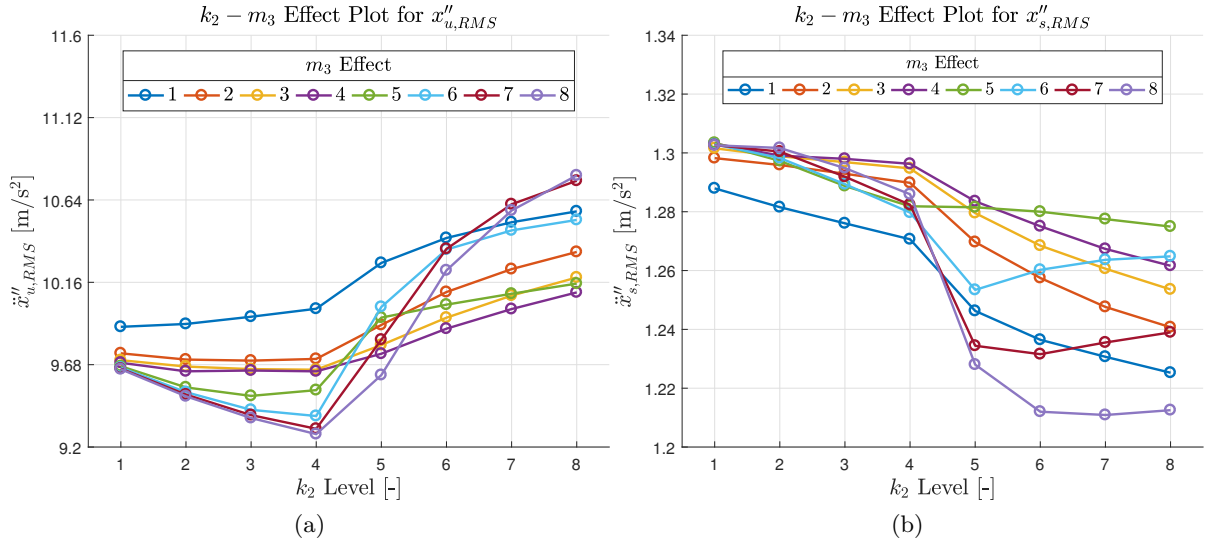


Figure 6.9: $k_2 - m_3$ interaction plots for $\ddot{x}_{u,RMS}$ and $\ddot{x}_{s,RMS}$

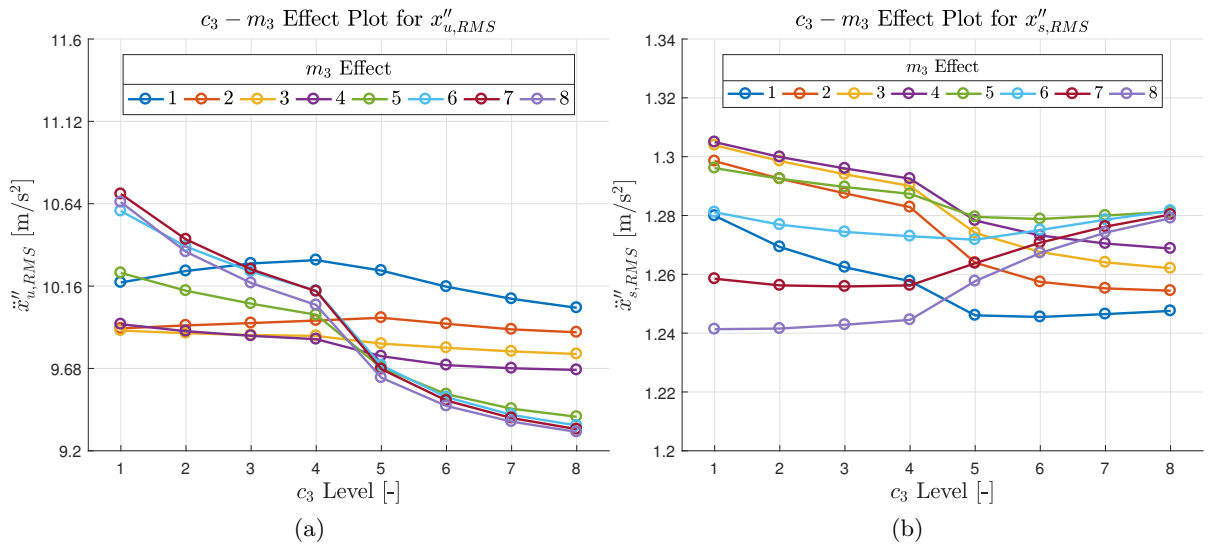


Figure 6.10: $c_3 - m_3$ interaction plots for $\ddot{x}_{u,RMS}$ and $\ddot{x}_{s,RMS}$

Since all the factors and interactions were found to be statistically significant, no pooling was performed. In Tables 6.5 and 6.6, the values for the corrected sum of squares (\hat{Q}) can be seen, while in Figures (6.11) and 6.12, the result of Percentages of Contribution analysis is shown in graphical form.

In particular, Figures 6.11 and 6.12 provide evidence that factors k_2 and m_3 , i. e. the stiffness of the secondary rubber and fluid inertia, have an important contribution on the variability of the RMS acceleration and then on the performance of the hydraulic top mount. Other than these two parameters, the viscosity of the fluid, represented by c_3 especially on the unsprung mass, should not be disregarded. Moreover, the analysis provides evidence that the interactions $c_3 - m_3$ and $k_2 - c_3$ affect the performance of the mount for the unsprung mass and the sprung mass, as well as that the third order interaction between k_2 , c_3 and m_3 is relevant for both outputs.

It is also important to underline that the contribution of the error is higher than that of some parameters; this is caused by the presence of many factors and interactions whose contributions are significant according to the F-test, but they are not relevant with respect to other factors. Because of this, it would not make sense to take into account all those parameters whose contributions are less than that of the error, since it would not be possible to distinguish among the two. For this reason, Figures 6.11 and 6.12 only show the contribution of the most relevant parameters, excluding the least relevant factors.

Thanks to the DOE, it was possible to start the analysis leading to the optimization of the hydraulic mount: it was possible to provide a picture of the most influential parameter. However, this analysis is not enough to fully understand the behaviour of the mount. Before proceeding with the optimization, it is essential to understand how the considered factors and interactions affect the physics of the hydraulic top mount and eventually in which way they impact the quarter car model.

The physics of the top mount is clearly summarized by its dynamic stiffness. Therefore, it is essential to understand how the different parameters modify the shape of the dynamic stiffness in frequency and which shape gives more benefit to the vehicle performance. The effect of the dynamic stiffness on the vibration absorption performance of sprung and unsprung mass is a topic for Chapter 7.

Table 6.5: Sums of Squares and their corrected values for $\ddot{x}_{u,RMS}$.

	df	\hat{Q}	Percentages of contribution
	(-)	((m/s ²) ²)	(%)
c_2	7	0.31	0.23
k_2	7	436.89	31.11
c_3	7	239.35	17.05
m_3	7	57162	4.07
$c_2 - k_2$	49	6.09	0.43
$c_2 - c_3$	49	0.15	0.011
$c_2 - c_3$	49	0.31	0.022
$k_2 - c_3$	49	184.37	13.13
$k_2 - m_3$	49	95.17	6.78
$c_3 - m_3$	49	160.37	11.42
$c_2 - k_2 - c_3$	343	0.88	0.063
$c_2 - k_2 - c_3$	343	1.11	0.079
$c_2 - k_2 - c_3$	343	0.55	0.178
$c_2 - k_2 - c_3$	343	2.50	0.35
Error	2401	4.98	0.42
Total	4095	1404.42	100.00

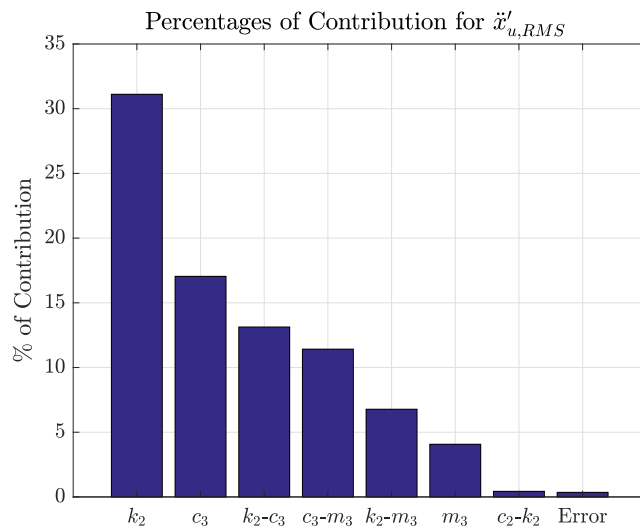


Figure 6.11: Bar chart for the contribution of the significant factors and interactions for the unsprung mass acceleration.

Table 6.6: Sum of Squares and their corrected values for $\ddot{x}_{s,RMS}$.

	df'	\hat{Q}	Percentages of contribution
	(-)	$((\text{m/s}^2)^2)$	(%)
c_2	7	8.5×10^{-3}	0.21
k_2	7	1.86	46.43
c_2	7	1.26×10^{-1}	3.13
m_3	7	5.23×10^{-1}	13.05
$c_2 - k_2$	49	2.28×10^{-2}	0.57
$c_2 - c_3$	49	6.73×10^{-4}	0.017
$c_2 - m_3$	49	4.2×10^{-3}	0.11
$k_2 - c_3$	49	2.04×10^{-1}	5.10
$k_2 - m_3$	49	4.52×10^{-1}	11.26
$c_3 - m_3$	49	4.94×10^{-1}	12.31
$c_2 - k_2 - c_3$	343	1.2×10^{-2}	0.030
$c_2 - k_2 - c_3$	343	5.8×10^{-33}	0.14
$c_2 - k_2 - c_3$	343	2.9×10^{-3}	0.73
$c_2 - k_2 - c_3$	343	2.90×10^{-1}	7.23
Error	2401	1.40×10^{-2}	0.35
Total	4095	4.010	100.00

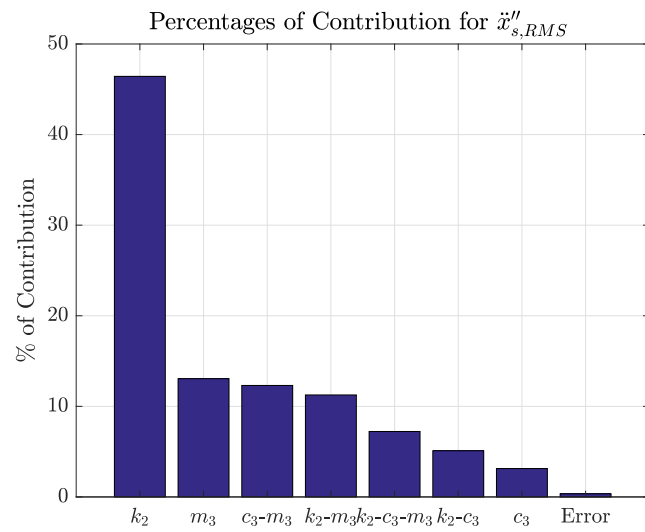


Figure 6.12: Bar chart for the contribution of the significant factors and interactions for the sprung mass acceleration.

CHAPTER 7

Top Mount Dynamic Stiffness Influence on Performance

The physics of the mount is described by its dynamic stiffness amplitude and phase; Chapter 6 discussed the impact of different parameters on the overall performance of the quarter car model, while the aim of this chapter is to go more in depth with the frequency analysis in order to point out feasible opportunities for improvement. In particular, the different effects of the significant parameters and interactions, pointed out in Chapter 6, on top mount dynamic stiffness are investigated in this chapter.

7.1 The Role of the Hydraulic Top Mount Dynamic Stiffness on the Sprung Mass Acceleration

The starting point of the analysis of the DOE result is the sprung mass acceleration since it is the most relevant performance parameter inasmuch as it is directly felt by vehicle occupants contrary to the unsprung mass acceleration. Chapter 6 discussed which parameters of the model are the most influential. In particular, it is clear that k_2 is the parameter that gives the highest variation in terms of sprung mass acceleration. In Figures 7.1, 7.3 and 7.5, variation in amplitude of dynamic stiffness according to k_2 , m_3 and c_3 is reported, while in Figures 7.2, 7.4 and 7.6, the variation in phase can be appreciated.

By joining the information contained in these plots and the plots relative to the factorial effects presented in Chapter 6, it is possible to predict which are the most suited physical characteristics of the hydraulic top mount in order to assure the best performance.

According to the ANOVA, the highest values of k_2 give the most important benefit. Looking at the plots in Figures 7.1 and 7.2, it is possible to note that the highest benefit should be caused by the lowest stiffness amplitude in the frequency range of interest (5 – 20 Hz), while the phase of the transfer function is higher than that given by the low

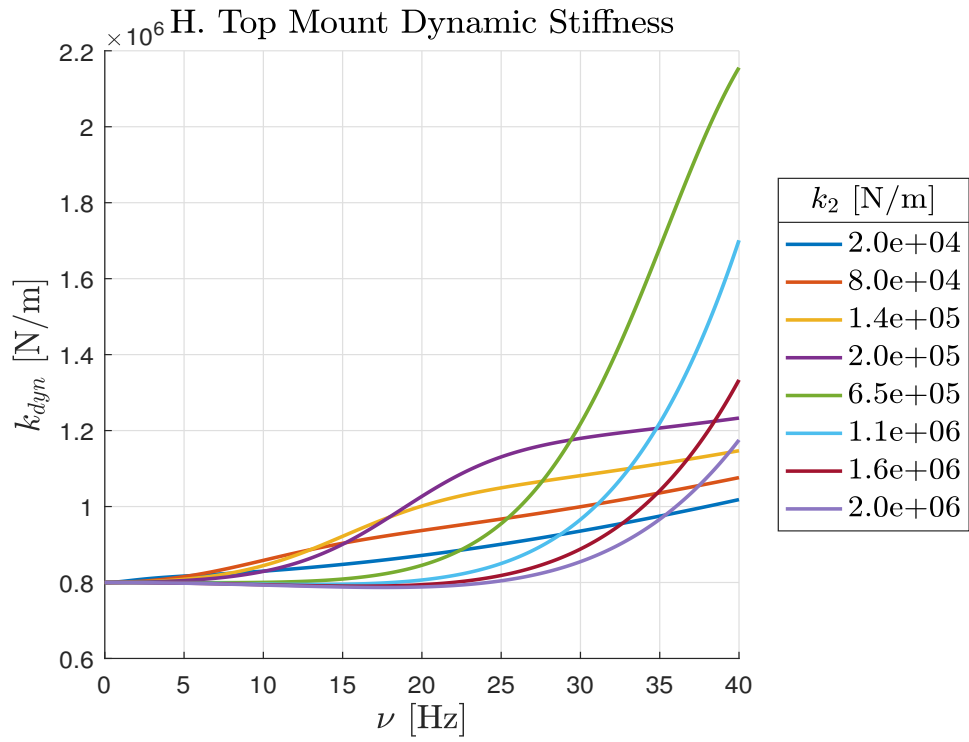


Figure 7.1: Variation of the dynamic stiffness amplitude according to the variation of the secondary rubber stiffness k_2 .

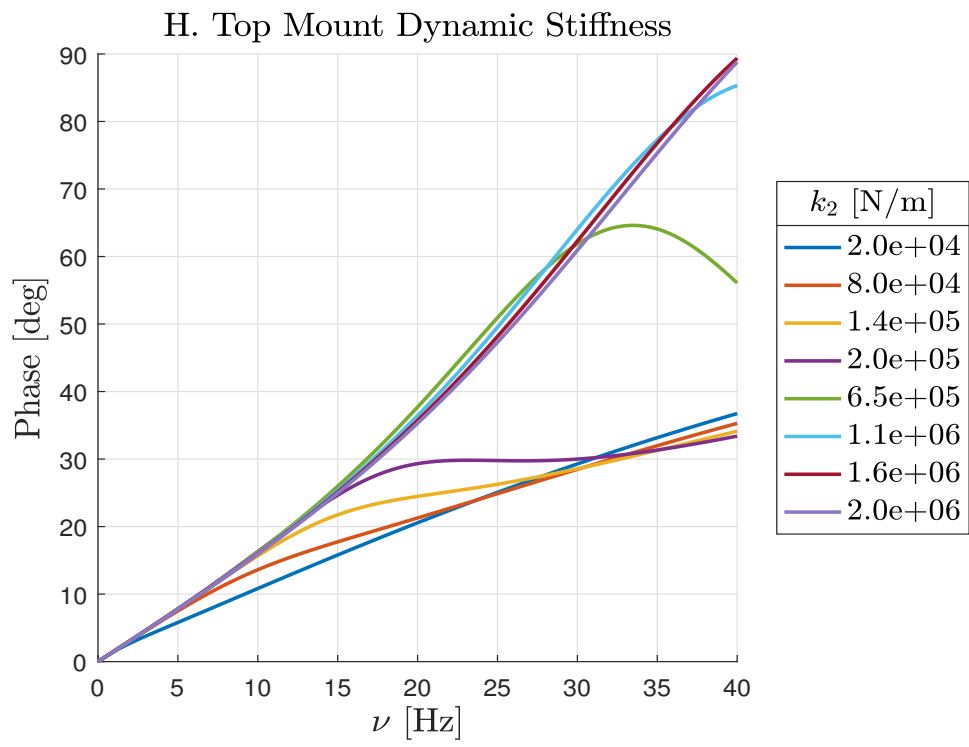


Figure 7.2: Variation of the dynamic stiffness phase according to the variation of the secondary rubber stiffness k_2 .

k_2 values, although it is pretty similar among the curves related to the high k_2 values. It

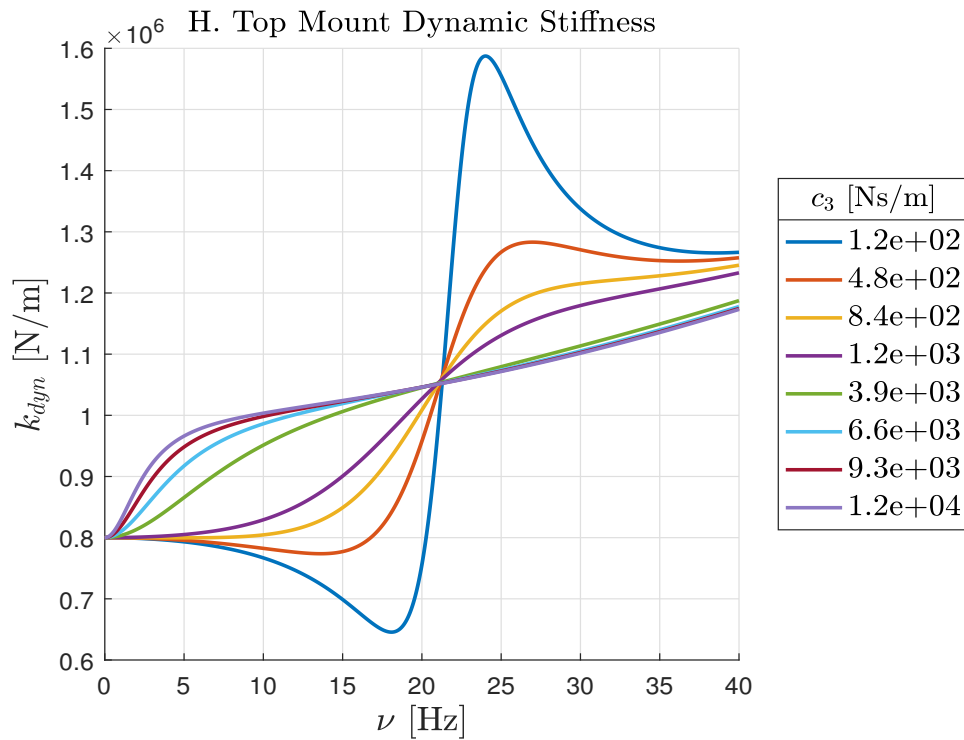


Figure 7.3: Variation of the dynamic stiffness amplitude according to the variation of the fluid viscosity c_3 .

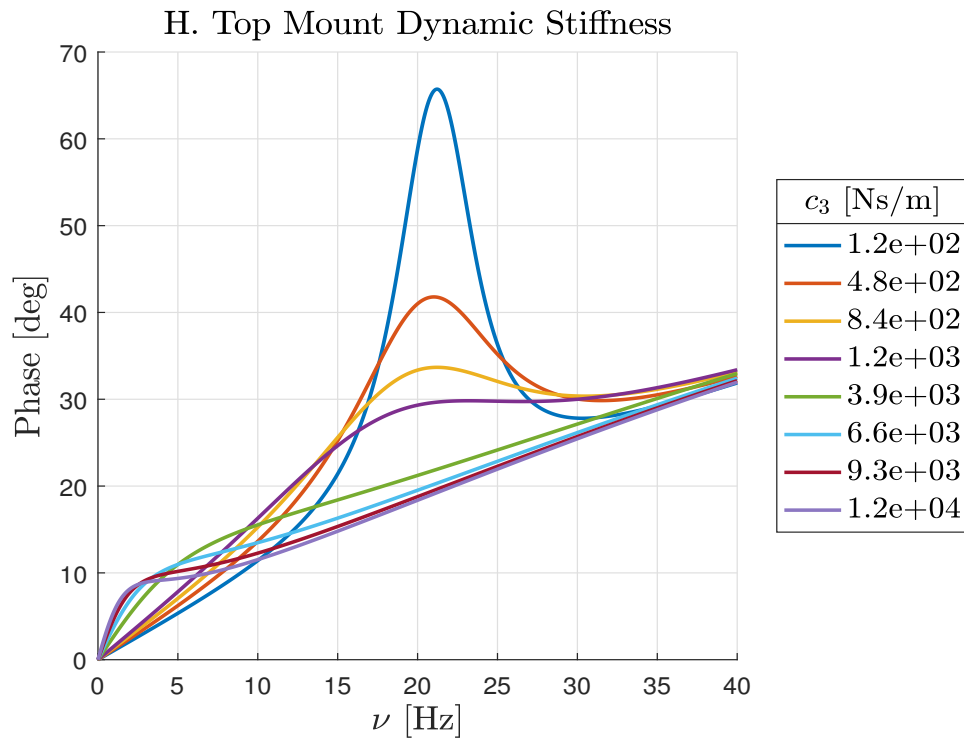


Figure 7.4: Variation of the dynamic stiffness phase according to the variation of the fluid viscosity c_3 .

is important to underline that by increasing this parameter, the frequency at which the

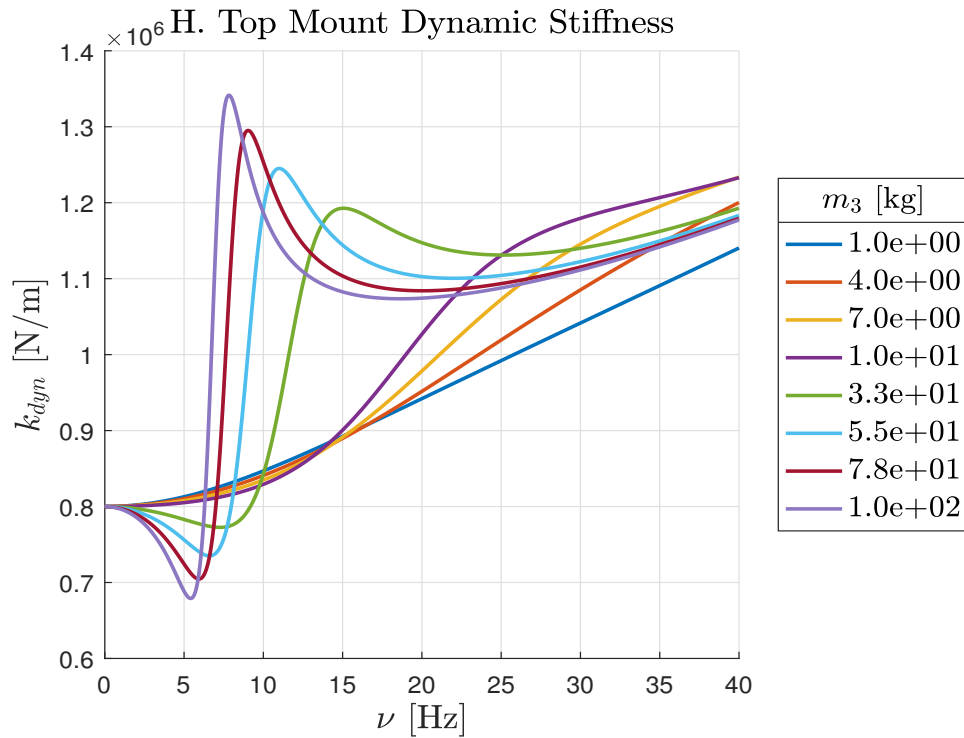


Figure 7.5: Variation of the dynamic stiffness according to the variation of the fluid inertia m_3 .

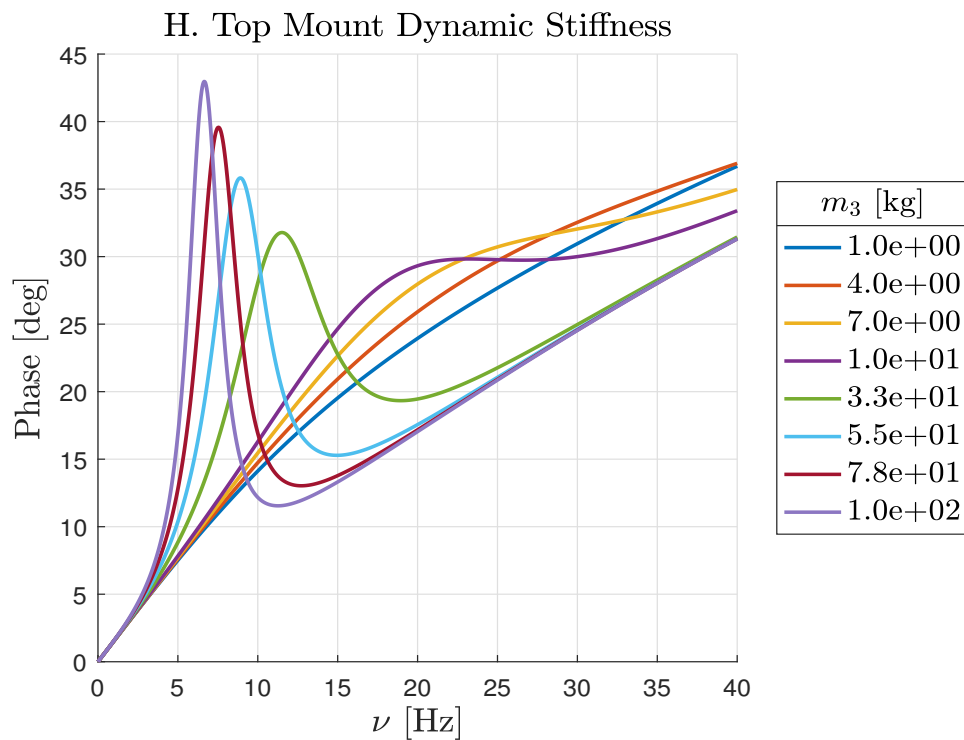


Figure 7.6: Variation of the dynamic stiffness phase according to the variation of the fluid inertia m_3 .

step in dynamic stiffness amplitude occurs is moved forward and its amplitude becomes increasingly higher.

The other important parameter is the fluid inertia m_3 . In this case, the most beneficial values are the the lowest and the highest ones, since both give an improvement with respect to the mid-range value in terms of RMS of sprung mass vertical acceleration. In particular, it is worth noting that the highest values for m_3 shift the frequency at which the step in amplitude occurs at increasingly lower values. Moreover, and they cause an undershoot and an overshoot which are increasingly relevant as m_3 is increased. Therefore, similar to the effect in k_2 , the highest values of m_3 give a low dynamic stiffness amplitude around 5 – 10 Hz, but they also assure a high dynamic stiffness amplitude around 10 – 20 Hz with the peak, in amplitude and phase, properly around 10 Hz, close to the wheel hop frequency of the quarter car model. Looking at the interaction between k_2 and m_3 , one can better understand the desired dynamic stiffness: according to the ANOVA, this interaction is significant and the most relevant improvement is obtained for high values of both parameters. Thanks to the linearity of the hydraulic top mount model, the superposition principle can be applied. Therefore, it is possible to affirm that high values of m_3 tune the frequency step around wheel hop frequency, while high values of k_2 contribute to making this step sharper and, at the same time, they increase the value of the amplitude after the step.

The third single factor, although less significant than the other two, is c_3 . In this case, mid-range values seem to assure the best performance. Similar to the previous cases, these values assure the highest values of phase in the considered frequency range, even though a peak can be observed only around 20 Hz if this is the only parameter that is changed. This could also explain why its contribution is relatively small. However, considering the interactions with the other two parameters, a low value for c_3 is advisable since it is able to enhance the characteristic shape individuated as the most suited for this problem.

In conclusion, it is possible to affirm that the most beneficial shape for dynamic stiffness is the one whose step occurs around the resonance frequency in the secondary ride (wheel hop frequency) and then the one reaching the peak in phase and amplitude around that frequency. At this point, it is important to understand the physics behind this particular shape.

7.2 The Physical Characteristics of the Hydraulic Top Mount Dynamic Stiffness

When the hydraulic top mount is excited with a harmonic function, it is possible to express its dynamic stiffness as in Equation (7.1), where $K(\omega)$ and $C(\omega)$ are the frequency dependent equivalent stiffness and damping.

$$K_{dyn}(\omega) = \frac{F_t}{X_t} = K(\omega) + j\omega C(\omega) \quad (7.1)$$

This formulation can be useful only in the case of harmonic input displacement with constant amplitude and frequency. Therefore, it is usually only suited to frequency domain

studies in which only the response of the system at a certain frequency is analyzed [2]. Moreover, if it is possible to overcome this assumption in the case of periodic input by expressing it as a sum of a finite number of harmonics through the Fourier series method, the same cannot be done in the case of a general aperiodic input since it can only be written as the sum of an infinite number of harmonics leading to non-causal results [30]. When this assumption is not met, it is necessary to replace this formulation through the equivalent viscous damping formulation, which consist of using a set of viscous dampers having the same behaviour of the structural damping in frequency. For this reason, in the scope of the present project, it was only employed to understand the frequency response of the mount in the case that the transfer function assumes the shape mentioned in Section 7.1 in the frequency range of interest (5 – 20 Hz).

It has been affirmed that an advisable shape for the dynamic stiffness has a peak in phase around the wheel hop resonance frequency of the vehicle. In such cases, according to Equation (7.1), a high value of equivalent damping is obtained, which becomes the dominating parameter of the dynamic stiffness. The high equivalent damping obtained through this shape, then, should be able to kill the harmonics at resonance frequency and to reduce the acceleration response of the sprung mass.

The structural damping model allows one to understand that a frequency dependent damping is advisable in order to have the best performance of the mount since it is relatively easy to tune the damping to be the highest when it is actually necessary. As stated, the model is not useful for time domain evaluations. Therefore, whenever it is necessary to make this type of comparison, the structural damping model must be replaced with the equivalent viscous damping model.

7.3 First Attempt of Hydraulic Top Mount Parameters Optimization

Having recognized which shape is the best suited for the transfer function of the top mount, it was, then, possible to make a first attempt to understand the capabilities of the new top mount. It has been shown that it is advisable to have a peak in the the dynamic stiffness phase in order to assure the highest value of damping around the wheel hop frequency. Therefore, the parameters were modified to have a resonance peak in the secondary ride range. However, it is important not to choose a transfer function where the peak is too narrow in order to avoid robustness problems. A change in the suspension or tire parameters of the quarter car model could influence the wheel hop frequency and then nullify the benefit given by the hydraulic top mount or even worsen the performance.

In Table 7.1, the resonance frequency and the phase peak of the dynamic stiffness are shown as well as the parameter values necessary to obtain this shape, together with the results in terms of sprung mass acceleration and the road holding index.

It is noticeable that lower values of RMS acceleration can be reached by changing the

values of k_2 , m_3 and c_3 to 550 N/mm, 80 kg and 0.5 Ns/mm, respectively. In this way, the resonance frequency was shifted around the wheel hop frequency and the dynamic stiffness phase increased as indicated in Table 7.1, in which the reference value of the baseline hydraulic top mount and of the rubber top mount are reported as well. By tuning the hydraulic top mount around a frequency close to the wheel hop, it is possible to obtain an improvement of 7.0% for acceleration with respect with the baseline model of the hydraulic top mount and an improvement of 8.4% with respect to the rubber top mount quarter car model. At this point, the real problem is the translation of these characteristics to an actual device.

Table 7.1: New values of RMS acceleration for the sprung mass after the variation of m_3 , k_2 , and c_3 to have a phase peak in secondary ride frequency range.

	Parameters		Outputs			
	ν_{res} (Hz)	Φ_{res} (deg)	$\ddot{x}_{s,RMS}$ (m/s ²)	$\dot{x}'_{s,RMS}$ (m/s ²)	$\ddot{x}''_{s,RMS}$ (m/s ²)	$\eta_{rh,RMS}$ (-)
Tuned H. Top Mount	11.1	132.9	1.74	1.22	1.20	0.194
Reference H. Top Mount			1.79	1.21	1.29	0.183
Rubber Top Mount			1.80	1.21	1.31	0.181

For the sake of clarity, in Figure 7.7, the dynamic stiffness of the top mount is shown and a really high peak at wheel hop frequency for both amplitude and phase is evident, as it has been suggested in Section 7.1. In Figure 7.8 it is possible to appreciate the superimposition of the sprung mass acceleration FFT for the base and the tuned hydraulic top mount. It is noticeable that, while the lower frequencies remain untouched by the change, while lower peaks can be appreciated in the secondary ride range.

In Figure 7.7 the displacement Fast Fourier Transform (FFT) is shown and it can be seen that a higher displacement is present close to 10 Hz. This is the result of a low dynamic stiffness at that frequency value. Therefore, it is also important to check that the displacement value remains in the tolerance range before applying this type of solution.

Another negative aspect of the tuned parameters for the hydraulic top mount is the value of road holding index, which tend to increase in case of the tuned mount along with its RMS value. This counter-effect causes a worsening in vehicle handling, which must be investigated before applying this new solution. In Figure 7.10, a time history of the road holding index is presented; it noticeable that the in the case of the reference top mount, the road holding index has lower peaks as suggested by the lower RMS values.

The last necessary check to accept the proposed model is the verification of its robustness in off-design conditions. The parameter that can undergo to the largest variation is the stiffness of the wheel ($k - w$): it is strictly linked to the inflation pressure of the tire.

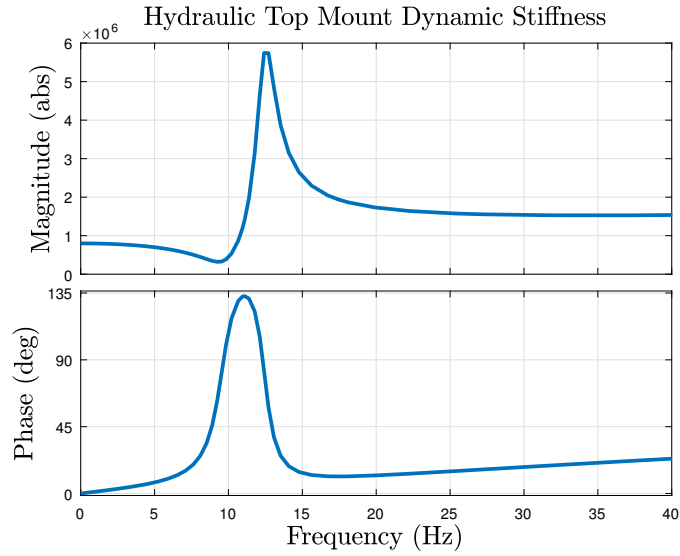


Figure 7.7: Dynamic stiffness Bode Plot in case of the tuned parameters.

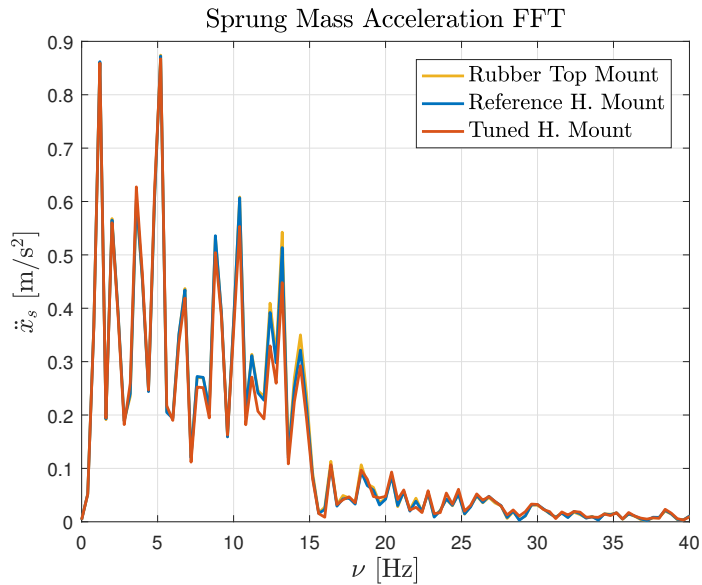


Figure 7.8: Comparison between the FFT of the sprung mass acceleration for quarter car model with the hydraulic top mount before and after the tuning and for the quarter car model with the rubber top mount.

For this reason, a sensitivity analysis of the RMS acceleration of the sprung mass was carried out to verify that the proposed solution were also robust in off-design conditions. In order to check the sensitivity of this quarter car model to variations in wheel stiffness (k_w), the quarter car model with the tuned hydraulic top mount was simulated with a wheel stiffness that varies by $\pm 15\%$. In Figure 7.11, it is possible to see the variation of the RMS values of the sprung mass acceleration for the reference and tuned top mount as well as those for the rubber top mount. It is clear that in all the three cases wheel stiffness variation causes a relevant variation for the RMS value of the acceleration, but it varies in

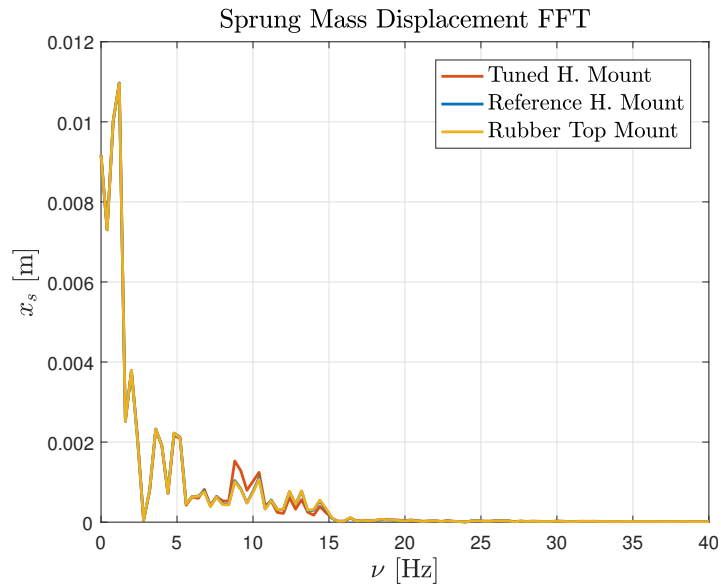


Figure 7.9: Comparison between the FFT of the sprung mass displacement for quarter car model with the hydraulic top mount before and after the tuning.

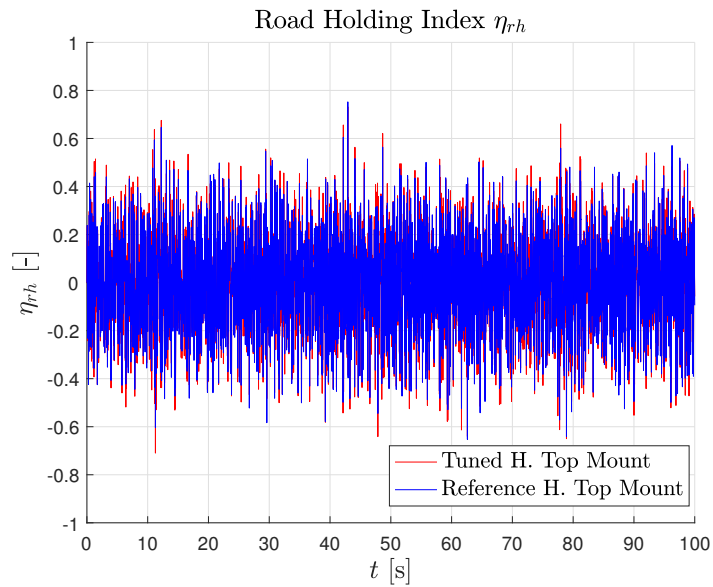


Figure 7.10: Comparison between the Road Holding Index time histories for the two different set of parameters for the Hydraulic Top Mount

the same way in all three cases. Therefore, the new top mount is able to assure the same robustness as the reference hydraulic mount and, more importantly, as the conventional rubber top mount.

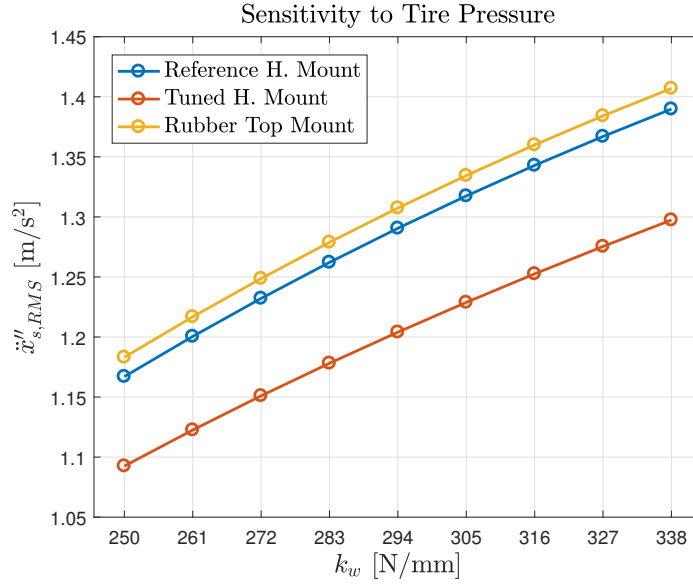


Figure 7.11: Variation of RMS values of the sprung mass acceleration due to the variation of the wheel stiffness (k_w) in the case of the reference hydraulic top mount (blue), tuned hydraulic top mount (red) and rubber top mount (yellow).

7.4 The Role Top Mount Dynamic Stiffness on the Unsprung Mass Acceleration

The acceleration of the unsprung mass is the second output considered in the DOE plan, however this performance parameter is not really relevant in the assessment of comfort performance since it is not directly felt by vehicle occupants.

The analysis can be performed similarly to the case of sprung mass. Referring to the plots showing the dynamic stiffness variation shown in Section 7.1 and to the main effects plots shown in Chapter 6, it is noticeable that an increase in the dynamic stiffness amplitude helps in the reduction of RMS unsprung mass acceleration.

In particular, according to the data shown in Chapter 6, the values of k_2 that most reduce the acceleration are the mid-range values, which cause an increase of in dynamic stiffness amplitude without reducing its phase, bringing an overall increase in equivalent damping and stiffness in that range.

The viscosity of the fluid c_3 , instead, seems to be more beneficial at the upper end values, which, according to Figures 7.3 and 7.4, lead to an increase in amplitude and reduction in phase of k_{dyn} . This trend can be explained by the increase of equivalent stiffness of the mount.

The parameter m_3 is not very influential for the unsprung mass acceleration. Similar to k_2 , mid-range values ensure the lowest RMS acceleration for the unsprung mass; the resulting dynamic stiffness is the one with the lowest amplitude among the group composed of the highest m_3 values and the lowest values of phase between 5 and 10 Hz. Therefore, also in this case, a high equivalent stiffness is assured in the first part of the frequency

range, similar to the case of c_3 . The same cannot be affirmed for the remaining part of the frequency range of interest since mid-range values of m_3 makes a higher dynamic stiffness in amplitude and phase and since, in that case, it would be tuned around lower frequency values.

In conclusion, a high value of equivalent stiffness seems to improve the ride performance relative to the sprung mass of the vehicle, however it is worth noting that the reduction of unsprung mass acceleration is not the objective of ride comfort improvement since the customer, i. e. the passenger of a vehicle, can only feel a reduction in sprung mass acceleration.

7.5 Hydraulic Top Mount in Series with the Suspension Strut

Once a solution for the standard configuration for the top mount and shock absorber has been accepted, it was decided to test the same solution on the second arrangement developed. In Chapter 5, it was shown that this solution can offer some advantages in terms of sprung mass acceleration, but not in terms of unsprung mass. The aim of this section is to understand if the optimized solution for the standard configuration can assure the same performance improvements. In order to perform this task, the model described in Chapter 4 has been simulated with the new hydraulic mount.

In Table 7.2, the results of the simulation are shown, which contains the RMS sprung mass acceleration (\ddot{x}_{RMS}) and its components for primary and secondary ride (\ddot{x}'_{RMS} , \ddot{x}''_{RMS}), as well as the RMS value of the road holding index ($\eta_{rh,RMS}$). From the data in the table, an improved performance can be assured with the optimized solution for the standard configuration: a further 2.5 % in performance can be gained with respect to the standard configuration, while the overall gain is equal to 10.7 % relative to the traditional rubber top mount. For the other configurations, the primary ride performance remained almost untouched, passing from the baseline to the optimized condition, but, as was seen in Chapter 5, this configuration is also able to assure a slightly better performance in that frequency range.

In Figure 7.12, the FFT of the sprung mass displacement for both configurations with the hydraulic top mount and rubber mount have been superimposed. This plot confirms the performance improvement in the whole frequency range.

In addition, Table 7.2 reports the RMS value of the road holding index, which is instead slightly higher than the corresponding values for the other models. Therefore, prior to accepting this configuration, it is important to verify that this drawback is not critical.

The last aspect that was verified for this solution was its robustness due to tire pressure changes, as it was for the optimized solution for the standard quarter car model configuration. In Figure 7.13, the sensitivity of the new model to the wheel stiffness in comparison to that of the old model is shown. Since the two lines are parallel, no interaction between

Table 7.2: RMS values of sprung mass acceleration and road holding index for the quarter car model with optimized h. top mount in series with the strut.

	0 – 5 Hz		5 – 20 Hz	
	$\ddot{x}_{s,RMS}$ (m/s ²)	$\ddot{x}'_{s,RMS}$ (m/s ²)	$\ddot{x}''_{s,RMS}$ (m/s ²)	$\eta_{rh,RMS}$ (–)
New Configuration Tuned H. Top Mount	1.66	1.16	1.17	0.194
Std. Configuration Tuned H. Top Mount	1.74	1.22	1.20	0.194
Rubber Top Mount	1.80	1.21	1.31	0.181

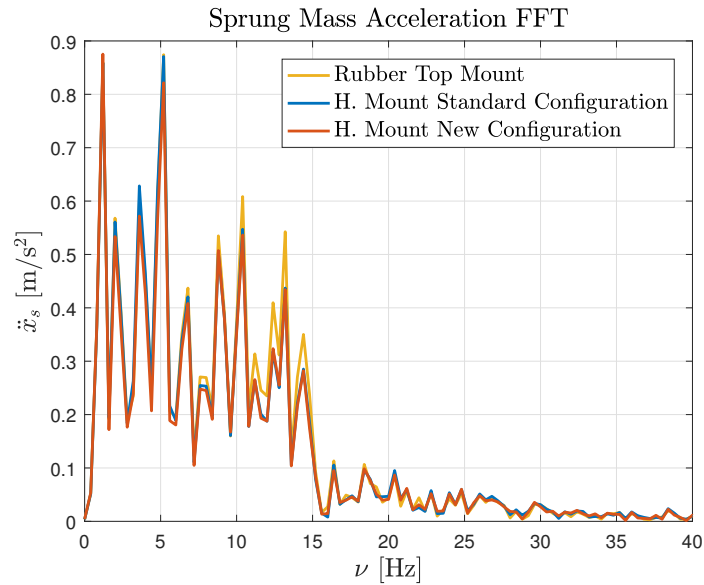


Figure 7.12: FFT of the sprung mass acceleration for the two configurations of the quarter car model with the hydraulic top mount and for the quarter car model with the rubber top mount.

the tire stiffness and the different position of the mount occurs.

Looking at the results obtained with this new configuration, it seems obvious to prefer this second solution, especially considering that this hydraulic mount has been optimized only for the standard configuration and a potential higher improvement could be achieved. Nevertheless, before adopting this arrangement, it is also necessary to consider its impact on handling performance, which was not analyzed in this project except for the road holding index.

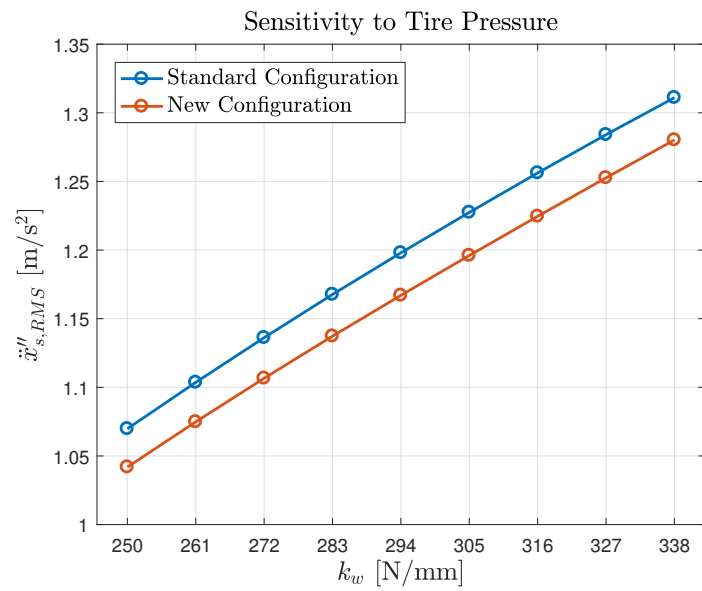


Figure 7.13: Sensitivity of the two different configurations for the hydraulic top mount to the variation of tire stiffness.

CHAPTER 8

Conclusions and Recommendations

The first important result of the project was the building of a hydraulic mount model and its subsequent integration into a quarter car model, which allowed for the systematic comparison of the characteristics of two different top mounts. The realization of such mathematical models was an important result on its own, since it is the first example in literature of a quarter car model integrated with a hydraulic top mount, although different models for the hydraulic mount can be found for other applications.

Moreover, throughout the whole project, the benefits given by the employment of the hydraulic top mount in place of the rubber one become apparent. It has been proven that this kind of device can improve the ride comfort performance of the vehicle in the secondary ride range without affecting the performance at lower frequencies, i. e. at the primary ride, which are usually filtered by other suspension components, like primary elastic elements. This aspect is the second important result of this project: the employment of a standard rubber device, usually results in a trade-off between the primary and the secondary ride. The improvement obtained through the implementation of the hydraulic top mount model in the quarter car model is presented in Table 8.1. It is possible to note that the hydraulic mount in the new arrangement offers the highest improvement in terms of RMS acceleration of the sprung mass according to the model developed in this project. Clearly, it is necessary to verify the feasibility of the mount manufacturing as well as of that of new suspension arrangement. As previously underlined, the hydraulic mount in the new configuration is able to give not only improvements in the secondary ride, but also a non-negligible improvement in primary ride, while a subtle worsening of the performance occurs in the primary ride in the case of the standard configuration.

Another important aspect of the project was the identification of the best suited dynamic stiffness transfer function for the top mount to improve ride comfort performance. It was found that it is necessary to assure a rather high amount of damping around the vehicle wheel hop frequency which corresponds to the target frequency in the design of the

Table 8.1: Summary of the improvement obtained through the implementation of the hydraulic top mount in the quarter car model in terms of RMS of sprung mass acceleration with respect to the rubber top mount configuration.

	$\ddot{x}_{s,RMS}$ (m/s ²)	$\ddot{x}'_{s,RMS}$ (m/s ²)	$\ddot{x}''_{s,RMS}$ (m/s ²)
Hydraulic mount (Standard configuration)	3.3 %	-0.83 %	8.4 %
Hydraulic mount (New configuration)	7.8 %	4.13 %	10.7 %

top mount. It was seen that rather than the single parameter values, it is more important to focus on the phase and on the resonance frequency of the mount. Therefore different strategies can be adopted to reach the desired shape.

Moreover, an opportunity for future improvement was discovered by changing the position of the top mount in the suspension assembly, although further research is necessary to study the feasibility of the new arrangement. Indeed, it could heavily impact the geometry of the suspension and, if that research were to yield positive results, it would be necessary to optimize the mount for this different arrangement.

A relevant amount of work has been carried out in the scope of this project, but a great many aspects must be explored before the solution were to arrive on the market. The first step that should be performed in the future is the development of a full-vehicle mathematical model in order to test the component from a broader point of view. A consequent deeper optimization of the mount parameters could yield further improvements. At that point, a feasibility study for the manufacturing of the mount with proper physical characteristic should be performed and then it would be necessary to proceed with tests on the actual device by using a full-scale vehicle. Another interesting strategy to test the device is represented by Hardware in the Loop (HIL) techniques: they allow one to insert the actual suspension assembly into the differential equation loop. The importance of this technique lies in the possibility of conducting tests on actual devices like suspensions inside a lab and then to arrive at a full-scale vehicle test with a clear idea of the potential results. In the case that all of these tests are conducted, it would be important to analyze handling indications other than only comfort problems.

Furthermore, it is important to carry out a cost/benefit analysis in order to verify that the performance improvement brought on by this device is worth the potentially higher development and manufacturing costs.

In conclusion, the realization of the hydraulic mount and quarter car models, together with the identification of the best transfer function for the mount through simulations, the attempt to use different arrangements for the suspension, and the reduction in the sprung mass acceleration highlighted by simulation are some of the most important results of the present project. However, the amount of work which should be carried on in future, as it

has been suggested here, makes the present work only a small step toward the realization of the highlighted results in actual vehicles underlining the pioneering nature of the project.

Bibliography

- [1] Giancarlo Genta and Lorenzo Morello. *The Automotive Chassis. Volume 1: Components Design*. Berlin: Springer Science+Business Media B.V., 2009. Chap. Suspensions, pp. 133–237.
- [2] L. Morello, L. Rosti Rossini, G. Pia, and A. Tonoli. *The automotive Body, Volume II: System Design*. New York: Springer Science + Business Media B. V., 2011. Chap. Noise, Vibration, Harshness, pp. 239–363.
- [3] Y. Yunhe, N. G. Naganathan, and R. V. Dukkipati. “A literature review of automotive vehicle engine mounting system”. In: *Mechanism and Machine Theory* 36 (2001), pp. 123–142.
- [4] Vibracoustic. 2016. URL: <https://www.vibracoustic.com/en/products/passenger-car/chassis/chassis-mounts/top-mount>.
- [5] Vibracoustic. 2016. URL: <https://www.vibracoustic.com/en/products/passenger-car/powertrain/powertrain-mounts/hydro-engine-mount>.
- [6] JE Colgate, C-T Chang, Y-C Chiou, WK Liu, and LM Keer. “Modelling of a hydraulic engine mount focusing on response to sinusoidal and composite excitations”. In: *Journal of Sound and Vibration* 184.3 (1995), pp. 503–528.
- [7] F. Golnaraghi, A. Khajepour, and A. Geisberger. “Nonlinear Modelling of Hydraulic Mounts: Theory and Experiment”. In: *Journal of Sound and Vibration* 249.2 (2002), pp. 371–397.
- [8] L. Morello and G. Genta. *The Automotive Chassis, Volume 2: System Design*. Berlin: Springer Science + Business Media B. V., 2009. Chap. Comfort Performance, pp. 349–426.
- [9] J. Tamboli and S. G. Joshi. “Optimum Design of a Passive Suspension System of a Vehicle Subjected to Actual Random Excitations”. In: *Journal of Sound and Vibration* 219.2 (1999), pp. 193–205.
- [10] P. E. Uys, P. S. Els, and M. Thoresson. “Suspension settings for optimal ride comfort of off-road vehicles travelling with different speed”. In: *Journal of Terramechanics* 44 (2007), pp. 163–175.

- [11] Mina MS Kaldas, Kemal Çalışkan, Roman Henze, and Ferit Küçükay. “The influence of damper top mount characteristics on vehicle ride comfort and harshness: parametric study”. In: *SAE International Journal of Passenger Cars-Mechanical Systems* 5.2012-01-0054 (2012), pp. 1–21.
- [12] Mina Kaldas, Kemal Çalışkan, Roman Henze, and Ferit Küçükay. “Optimization of damper top mount characteristics to improve vehicle ride comfort and harshness”. In: *Shock and Vibration* 2014 (2014), pp. 1–15.
- [13] W. C. Flower. “Understanding Hydraulic Mounts for improved Vehicle Noise, Vibration and Ride Qualities”. In: *SAE Technical Paper 850975* (1985).
- [14] J. Christopherson and G. Nakahie Jazar. “Dynamic behavior comparison of passive hydraulic engine mounts. Part 1: Mathematical analysis”. In: *Journal of Sound and Vibration* 290 (2006), pp. 1040–1070.
- [15] J. Christopherson and G. Nakahie Jazar. “Dynamic behavior comparison of passive hydraulic engine mounts. Part 2: Finite Element Analysis”. In: *Journal of Sound and Vibration* 290 (2006), pp. 1071–1090.
- [16] T. D. Gillespie. *Fundamental of Vehicle Dynamics*. Warrendale: Society of Automotive Engineers, Inc., 1992. Chap. Ride, pp. 125–193.
- [17] R. N. Marzabani and M. Fard. “Hydraulic Enigne Mounts: a survey”. In: *Journal of Vibrations and control* 20.10 (2014), pp. 1439–1463.
- [18] B. Piquet, C. A. Maas, and Capou F. “Next Generation of Suspension Bushings: Review of Current technologies and Expansion Upon New 3rd Generation Production Data”. In: *SAE Technical Paper Series* (2007).
- [19] W. Sauer and Y. Guy. “Hydro Bushings - Innovative NVH Solutions in Chassis Technology”. In: *SAE Technical Paper Series* (2003).
- [20] C. Scheiblegger and A. Hillis. “Hydro mounts: An in-depth modelling hydro mounts in vehicles for durability load analyses and vehicle dynamics simulation”. In: *Proceedings of the 13th International Symposium on Advanced Vehicle Control-AVEC*. Ed. by CRC press/Balkema - Taylor and Francis Group. Munich, Germany, 2016.
- [21] International Organization for Standardizations. *Mechanical vvibration and shock - Evaluation of human exposure to whole-body vibration (ISO Standard No 2631-1). Part 1: General Requirements*. 1997.
- [22] Robert Muksian and Charles D. Jr Nash. “A model for the response of seated humans to sinusoidal displacements of the seat”. In: *Journal of Biomechanics* 7 (1974), pp. 209–215.
- [23] Cho-Chung Liang and Chi-Feng Chiang. “A study on biodynamic models of seated human subjects exposed to vertical vibration”. In: *Journal of Industrial Ergonomics* 36 (2005), pp. 869–890.

- [24] M. Demic, J. Lukic, and Z. Milic. “Some aspects of the investigation of random vibration influence on ride comfort”. In: *Journal of Sound and Vibration* 253.1 (2002), pp. 109–129.
- [25] Renato Galluzzi, Andrea Tonoli, Nicola Amati, Gabriele Curcuruto, Piero Conti, Giordano Greco, and Andrea Nepote. “Regenerative Shock Absorber and the Role of the Motion Rectifier”. In: (2016).
- [26] G. Kim and R. Singh. “A study of passive and adaptive hydraulic engine mount systems with emphasis non-linear characteristics”. In: *Journal of Sound and Vibration* 179.3 (1995), pp. 427–453.
- [27] International Organization for Standardizations. *Mechanical vibration - Road surface profiles - Reporting of measured data (ISO Standard No 8608:2016)*. 2016.
- [28] Hoang Pham. *Springer handbook of engineering statistics*. Springer Science & Business Media, 2006.
- [29] Mario Vianello and Paolo De Blasi. “Measure and Prevention: Methodological Instruments for Reliability”. Lecture Notes from “Product Quality Design” course at Politecnico di Torino. 2016.
- [30] Giancarlo Genta. *Vibration dynamics and control*. New York: Springer-Verlag US, 2009. Chap. Damped Discrete Vibrating Systems, pp. 60–92.

Appendix A

Summary of Linear Differential Equations and Transfer Functions

In this appendix, the Linear Differential Equations (Linear Differential Equation (LDE)) and the Transfer Functions (TF) presented in chapter 3 is presented: all the equations are summarized in Table A.1 and A.2.

Table A.1: Table containing Linear Differential Equation (LDE) and Transfer Function (TF) of the two different types of mounts presented in Chapter 3.

	Hydraulic Mount	Rubber Mount
LDE	$f_t = k_1 x_t + c_1 \dot{x}_t + m_3 \ddot{x}_t + c_3 (\dot{x}_t - \dot{x}'_t)$	$f'_t = k'_1 x_t + c'_1 \dot{x}_t$
TF	$G = \frac{F_t}{X_t} = \frac{(c_1 s + k_1)(m_3 s^2 + (c_2 + c_3)s + k_2) + (m_3 s^2 + c_3 s)(c_2 s + k_2)}{m_3 s^2 + (c_2 + c_3)s + k_2}$	$G' = \frac{F'_t}{X_t} = k_1 + c_1 s$
	$G_v = \frac{F_t}{\dot{X}_t} = \frac{(c_1 s + k_1)(m_3 s^2 + (c_2 + c_3)s + k_2) + (m_3 s^2 + c_3 s)(c_2 s + k_2)}{s(m_3 s^2 + (c_2 + c_3)s + k_2)}$	$G'_v = \frac{F'_t}{\dot{X}_t} = \frac{k_1 + c_1 s}{s}$

Table A.2: Table containing Linear Differential Equation (LDE) and Transfer Function (TF) for the two different linear quarter car models presented in Chapter 3.

	Hydraulic Mount	Rubber Mount
LDE	$\ddot{x}_u = -\frac{k_w}{m_u}(x_u - u) + \frac{c_s}{m_u}(\dot{x}'_s - \dot{x}_u) + \frac{k_s}{m_u}(x_s - x_u)$ $\ddot{x}_s = -\frac{c_s}{m_s}(\dot{x}'_s - \dot{x}_u) + \frac{k_s}{m_s}(x_s - x_u)$ $\dot{x}'_s = \frac{f_t}{c_s} + \dot{x}_u$	$\dot{x}'_s = \frac{f_t}{c_s} + \dot{x}_u$
TF	$H = \frac{(c_s s + G)(m_s s^2 + k_s) + c_s G s}{(c_s s + k_s)(c_s s + G) - c_s^2 s^2}$ $I = \frac{(c_s s + G)k_w}{(c_s s + G)(m_u s^2 + c_s s + k_w)H - (c_s s + G)k_s - c_s G s - c_s^2 H s^2}$ $J = s^2 I$ $K = I \cdot H$ $L = s^2 K$	$H' = \frac{(c_s s + G')(m_s s^2 + k_s) + c_s G' s}{(c_s s + k_s)(c_s s + G') - c_s^2 s^2}$ $I' = \frac{(c_s s + G')k_w}{(c_s s + G')(m_u s^2 + c_s s + k_w)H' - (c_s s + G')k_s - c_s G' s - c_s^2 H s^2}$ $J' = s^2 I'$ $K = I' \cdot H'$ $L' = s^2 K'$

Appendix B

Bounce and Hop Mode

B.1 Bounce and Wheel Hop Frequencies

Bounce and hop frequencies for the quarter car model correspond to two first resonance peaks of its frequency response. For a common vehicle, bounce frequency usually is around $1 - 1.5\text{Hz}$, while hop frequency typically lies in the range between 10 and 15 Hz.

These frequency values depend on the parameters of the quarter car model: the sprung mass (m_s), the unsprung mass (m_u), the wheel rate (k_s) and tire rate (k_w). The equations to evaluate the ride and hop frequencies are shown in Equation (B.1) and (B.2).

$$\nu_{\text{bounce}} = \frac{1}{2\pi} \sqrt{\frac{RR}{m_s}} \quad (\text{B.1})$$

$$\nu_{\text{hop}} = \frac{1}{2\pi} \sqrt{\frac{k_s + k_w}{m_u}} \quad (\text{B.2})$$

Where RR is the ride rate of the quarter car model. It is evaluated as in Equation (B.3).

$$RR = \sqrt{\frac{k_s \cdot k_w}{k_s + k_w}} \quad (\text{B.3})$$

It is important to underline that there is also a nonlinear damper in the system that affects the values of these frequencies. The effect of the damper is always to reduce the “undamped” resonance frequency (ν_{bounce}), therefore slightly lower resonance frequencies are expected when they are evaluated through simulations. However, the damping coefficient of shock absorbers normally employed in the automotive field does not significantly affect the bounce and hop frequencies because of the coefficient’s relatively low value.

In order to evaluate these frequencies, it is sufficient to know the parameters of the quarter car model. In the case of the model used in this project, values are taken directly from a real car, and therefore it is necessary to transport the spring stiffness and the sprung mass to the centre of the wheel by means of the motion ratio (MR), i. e. by multiplying

Table B.1: Values of the quarter car model parameters at component level.

k_{spring} (N/mm)	$w_{vehicle}$ (N)
40	6235.41

Table B.2: Values of quarter car model parameters at the centre of the wheel.

k_s (N/mm)	m_s (kg)	k_w (N/mm)	m_u (kg)
34.3	545	294.7	80

them by the square of the motion ratio (MR), which depends on the geometry of the suspension.

In Table B.1, the actual value of sprung mass and spring rate are reported.

By knowing the motion ratio ($MR = 0.93$), it is possible to transport the value shown in Table B.1 at the centre of the wheel. Values of the quarter car model parameters at the centre of the wheel are shown in table B.2.

At this point, it is possible to evaluate the ride frequency and the wheel hop frequency for the model analyzed in this project. The values of ride frequency and bounce frequency are shown in Table B.3.

As it was affirmed, the other important element of the quarter car model is the shock absorber which is modelled as a nonlinear and non-symmetric damper in this project. In addition, the characteristic curve of the shock absorber refers to the component. Therefore, it was necessary to transport its characteristic curve to the centre of the wheel by dividing the damper stem speed by the motion ratio and multiplying the force by the same value.

Theoretical values of bounce and hop frequencies can be verified by means of the frequency response analysis. However, since in the quarter car model used in this project, a hydraulic top mount is present, to verify them it is first necessary to disable the module. The same analysis can be made, then, with the enabled module to analyze its impact in the quarter car model.

Table B.3: Theoretical values for ride and wheel hop frequencies.

ν_{bounce} (Hz)	ν_{hop} (Hz)
1.19	10.2

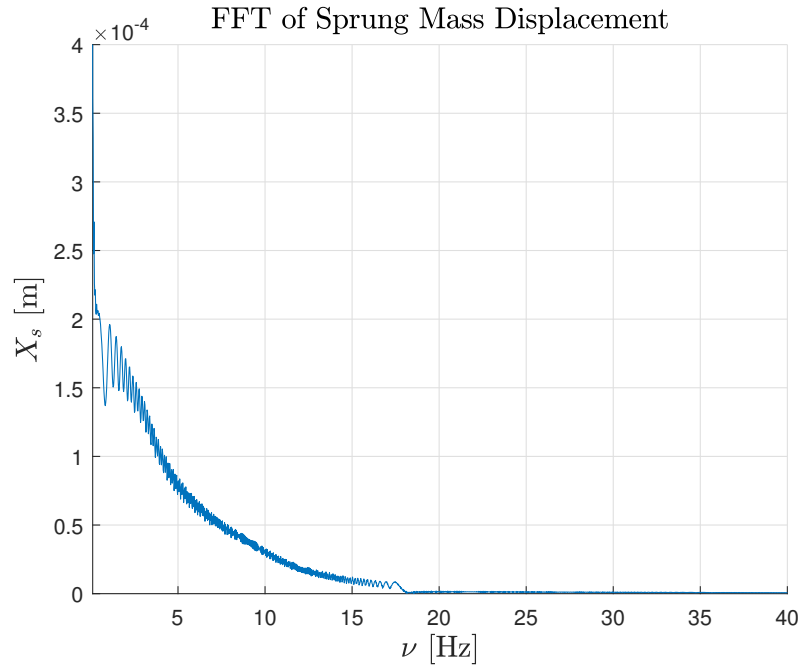


Figure B.1: Fast Fourier Transform for the displacement of the sprung mass.

B.2 Frequency response

B.2.1 Disabled Hydraulic Mount

As discussed, the quarter car model taken into account throughout this project is characterized by the presence of a hydraulic top mount; in order to assess ride and wheel hop frequency of the model, it is necessary to deactivate this module, thus obtaining a well-known quarter car model.

Another important characteristic of the system is its nonlinearity due to the shock absorber. For this reason, it is not possible to provide an analytic solution of the system in the Laplace domain. Therefore, it was decided to numerically evaluate the frequency response function by means of its Fast Fourier Transform (FFT) using the algorithm implemented in MATLAB[®]. Thus, it is possible to understand the contribution of each individual frequency value to the frequency response.

In Figure B.1, it is possible to see the FFT of the sprung mass displacement in the case of the hydraulic top mount module is deactivated. It is noticeable that there is a peak at a frequency of 1.075 Hz, which is clearly the bounce frequency of the vehicle. As expected, this frequency is slightly lower than the theoretical one because of the presence of the shock absorber, but it is still very near to that value.

In that same figure, it can be seen that another small peak is present around a frequency of 10.2 Hz, which should correspond to the wheel hop frequency. Wheel hop mode can be seen clearly in looking at Figure B.2, which shows the FFT of the unsprung mass displacement. For frequencies higher than the bounce, the displacement of the sprung mass becomes very small and the wheel hop mode is hardly noticeable by only analyzing

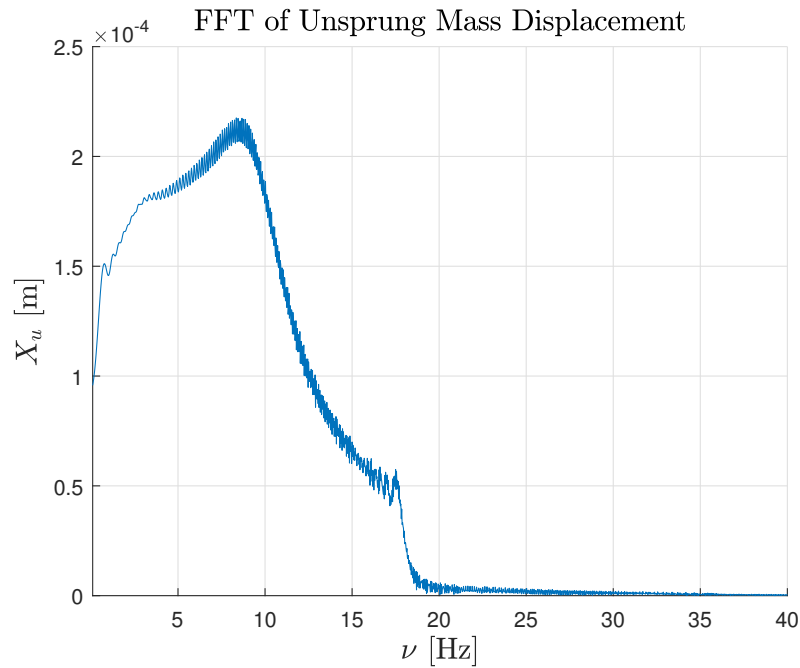


Figure B.2: Fast Fourier Transform for the displacement of the unsprung mass.

its frequency response. Instead, the FFT of the unsprung mass displacement led a clearly noticeable peak at a frequency of 8.35 Hz. Conversely, in only considering the frequency response of the unsprung mass displacement, it is not possible to capture the bounce since the low frequency vibrations are hidden by the hop mode.

B.2.2 Enabled Hydraulic mount

The same analysis made with the disabled hydraulic mount can be made once the hydraulic mount model has been enabled. In Figures B.3 and B.4, it is possible to understand the effect of the hydraulic top mount in bounce and hop modes. It can be seen that the hydraulic top mount does not affect the bounce mode, but it causes an increase in the wheel hop frequency which goes from 8.35 Hz to 10.90 Hz.

In Figures B.5 and B.6, the superimposition of the two plots is shown; a small increase in amplitude beyond the hop frequency can be seen, but also a slightly better behavior of the top mount for frequencies lower than the wheel hop is shown.

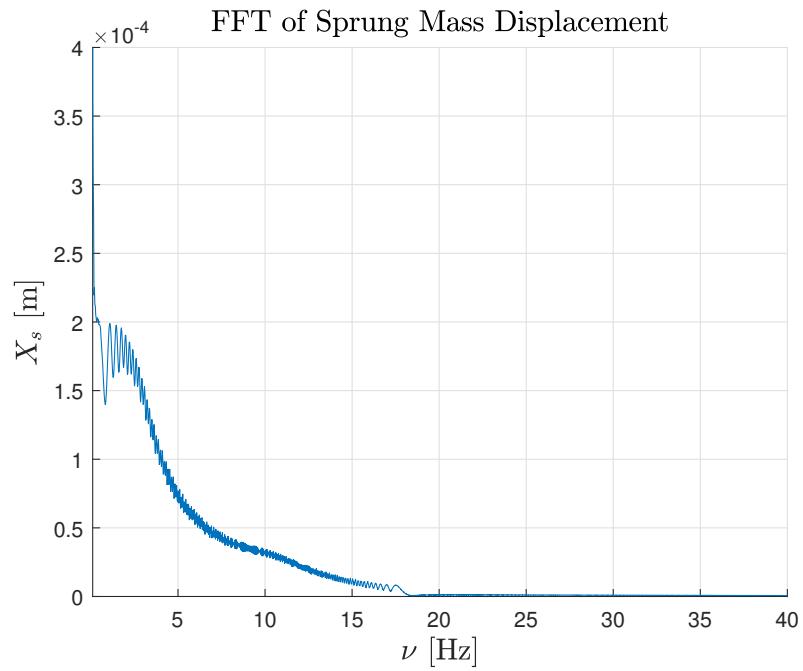


Figure B.3: Fast Fourier Transform of the sprung mass displacement with the enabled hydraulic top mount.

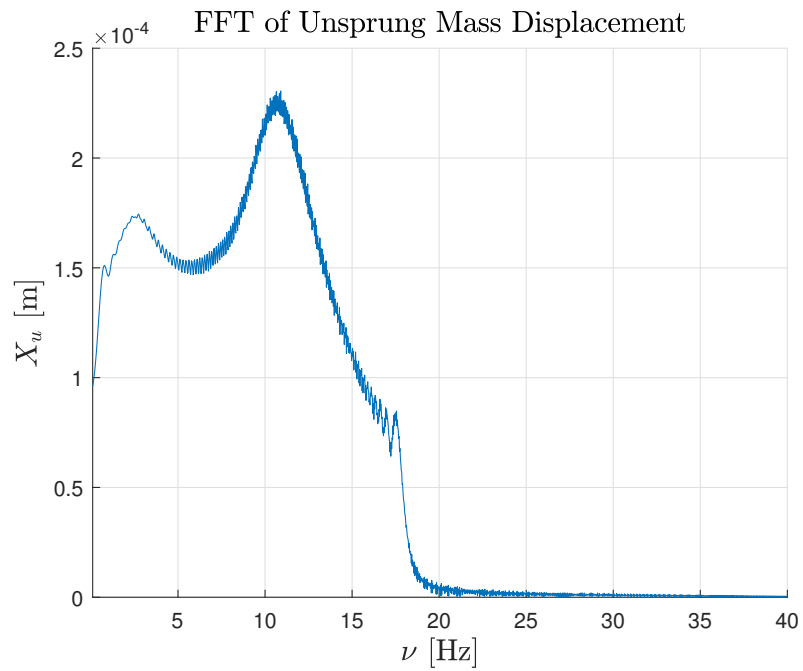


Figure B.4: Fast Fourier Transform of the unsprung mass displacement with the enabled hydraulic top mount.

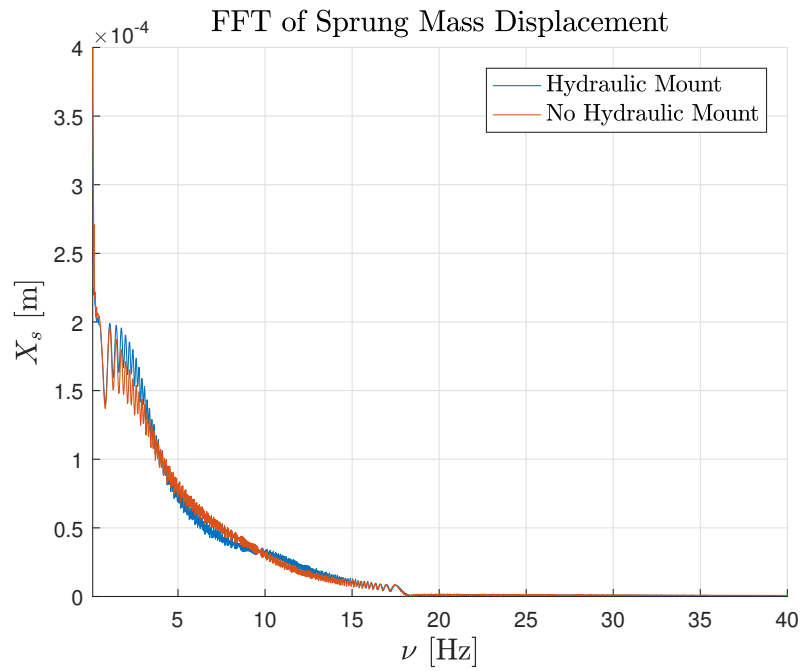


Figure B.5: Comparison between Fast Fourier Transform of the sprung mass displacement for the two different cases.

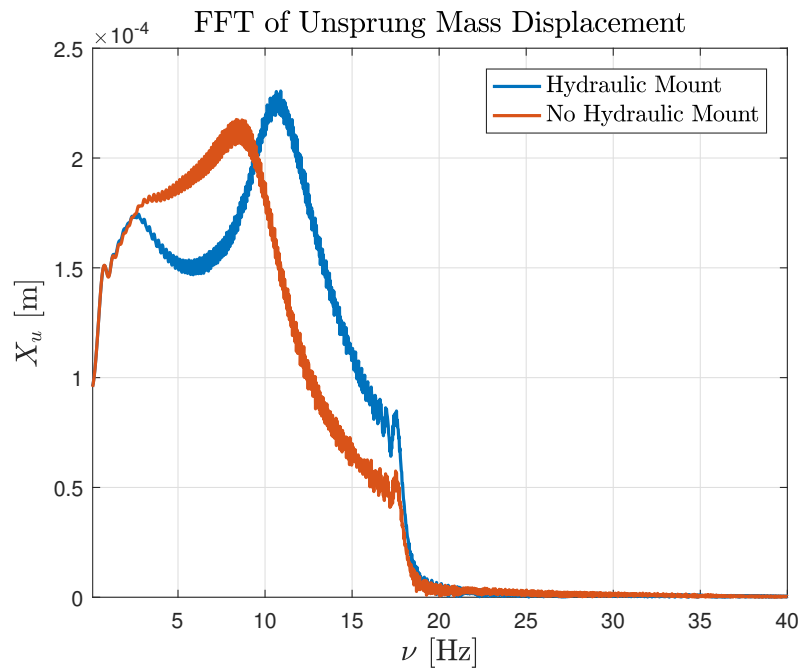


Figure B.6: Comparison between Fast Fourier Transform of the unsprung mass displacement for two different cases.

Appendix C

Quarter Car Model Plots

This appendix contains all the plots relative to the results obtained through the simulation of different models which are shown in the main body of the thesis.

C.1 Linear Quarter Car Models with the Hydraulic Top Mount

C.1.1 Time Simulation

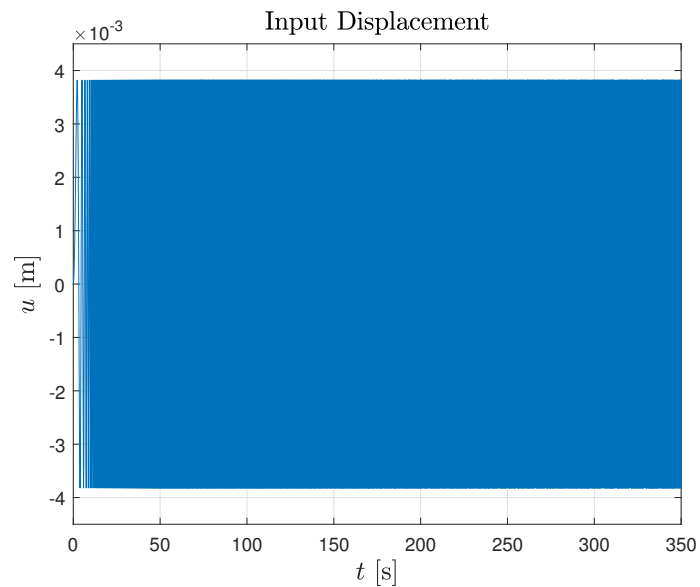


Figure C.1: Input signal for the linear quarter car models.

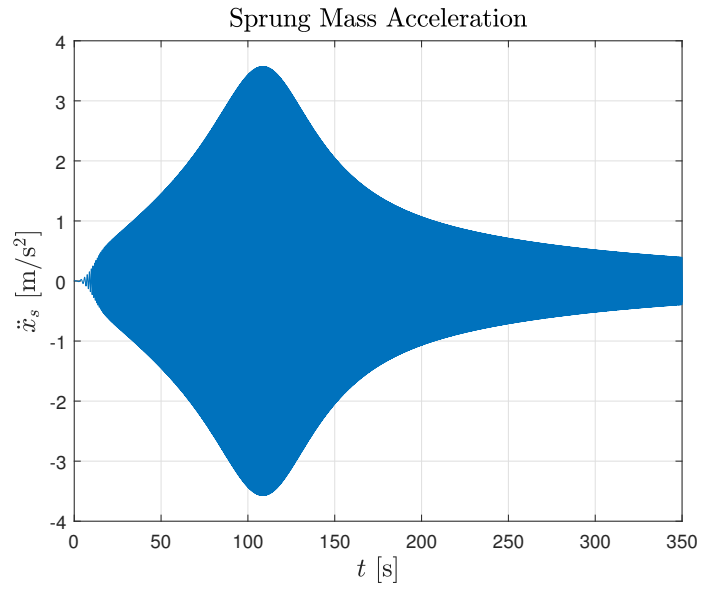


Figure C.2: Time history of the sprung mass acceleration in the linear quarter car model with the hydraulic top mount.

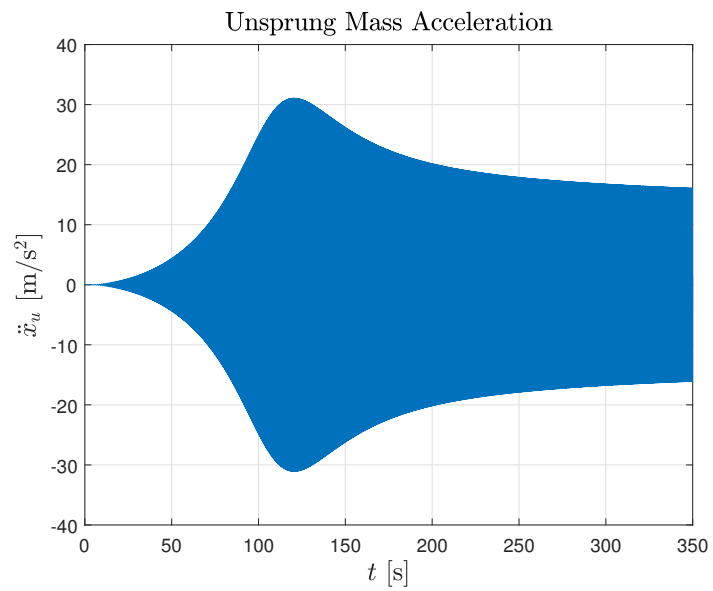


Figure C.3: Time history of the unsprung mass acceleration in the linear quarter car model with the hydraulic top mount.

C.1.2 Bode Diagrams

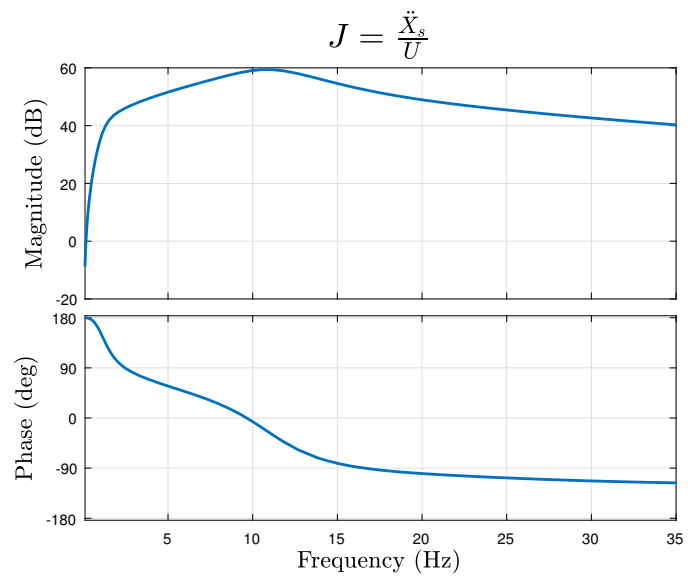


Figure C.4: Bode diagram for amplitude and phase for the transfer function between sprung mass acceleration and input displacement in case of quarter car model with the hydraulic top mount.

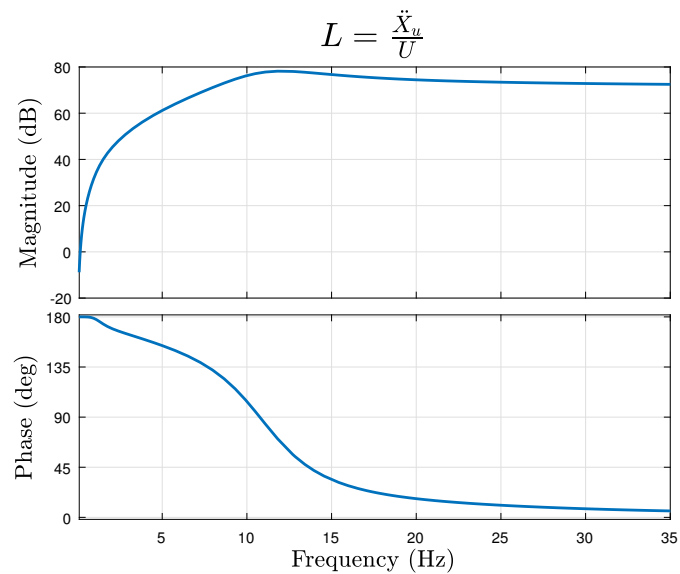


Figure C.5: Bode diagram for amplitude and phase for the transfer function between unsprung mass acceleration and input displacement in case of quarter car model with the hydraulic top mount.

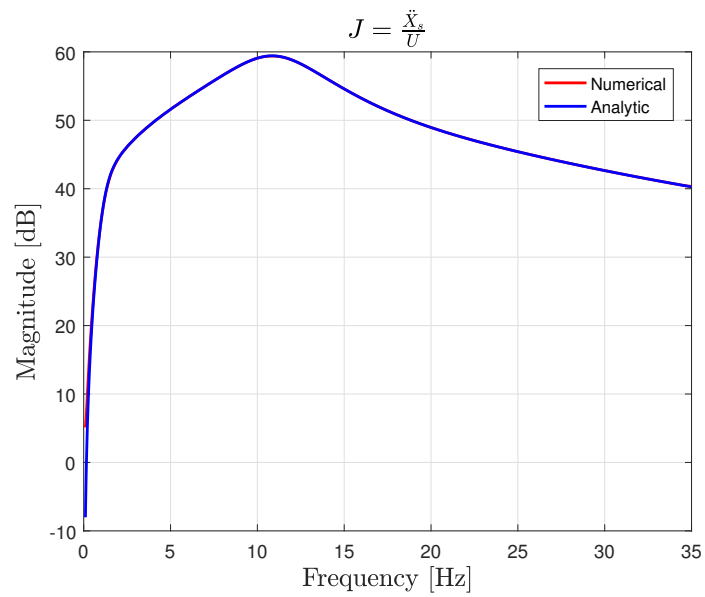


Figure C.6: Bode diagram for the transfer function K between the acceleration of the sprung mass and the input signal for the quarter car model with the hydraulic top mount.

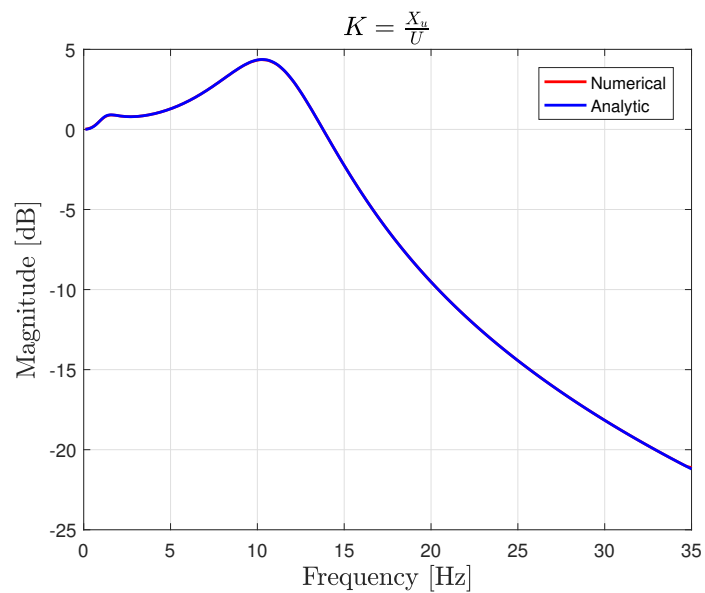


Figure C.7: Bode diagram for the transfer function K between the displacement of the unsprung mass and the input signal for the quarter car model with the hydraulic top mount.

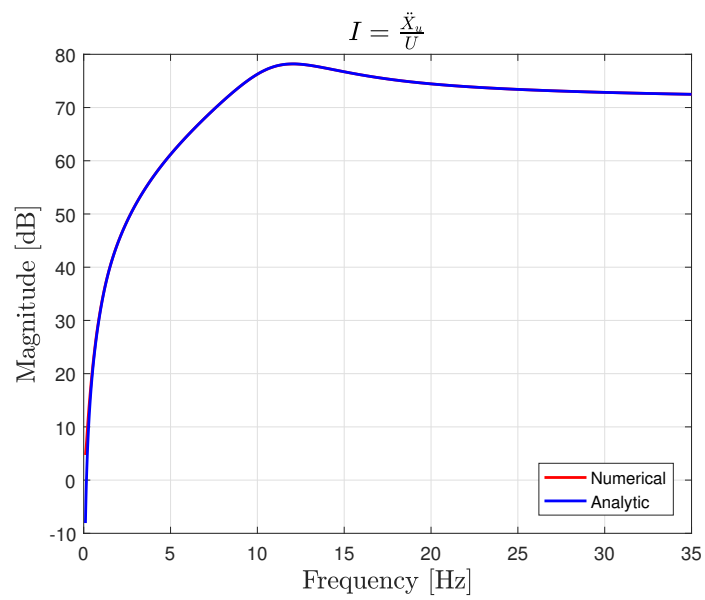


Figure C.8: Comparison between the analytic and estimated amplitude Bode diagram of the transfer function L for the quarter car model with the hydraulic top mount.

C.2 Linear Quarter Car Models with the Rubber Top Mount

C.2.1 Time Simulation

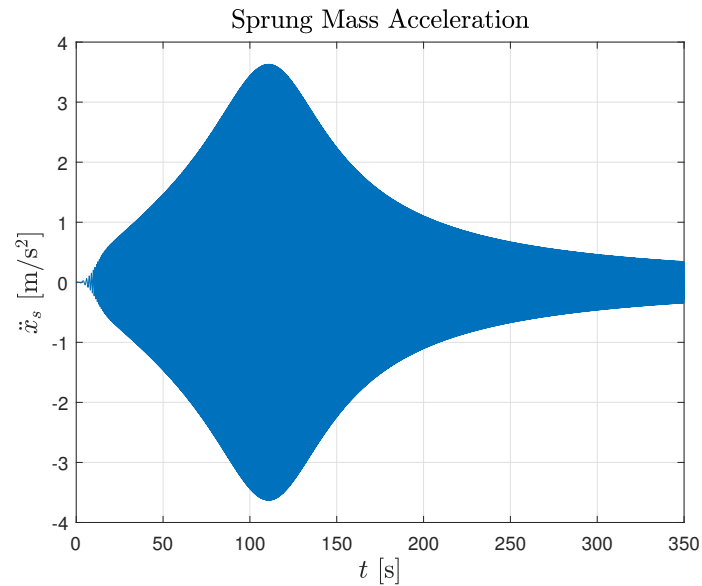


Figure C.9: Sprung mass acceleration in function of time for the quarter car model with the rubber top mount.

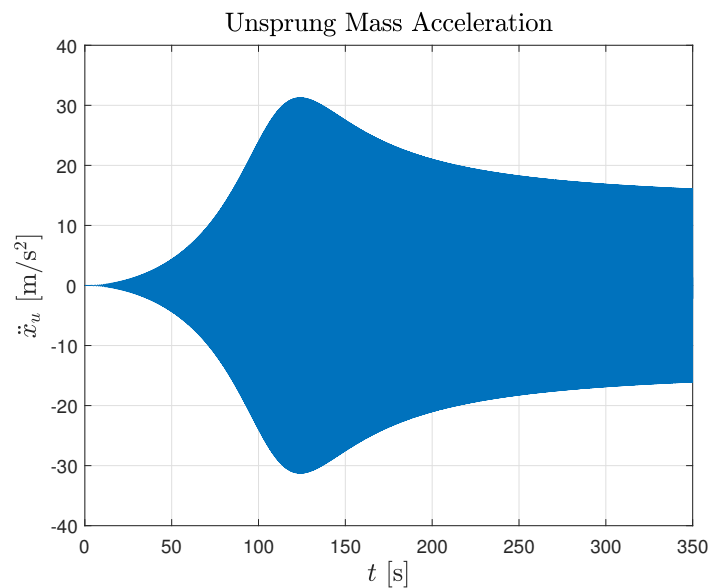


Figure C.10: Unsprung mass acceleration in function of time for the quarter car model with the rubber top mount.

C.2.2 Bode Diagrams

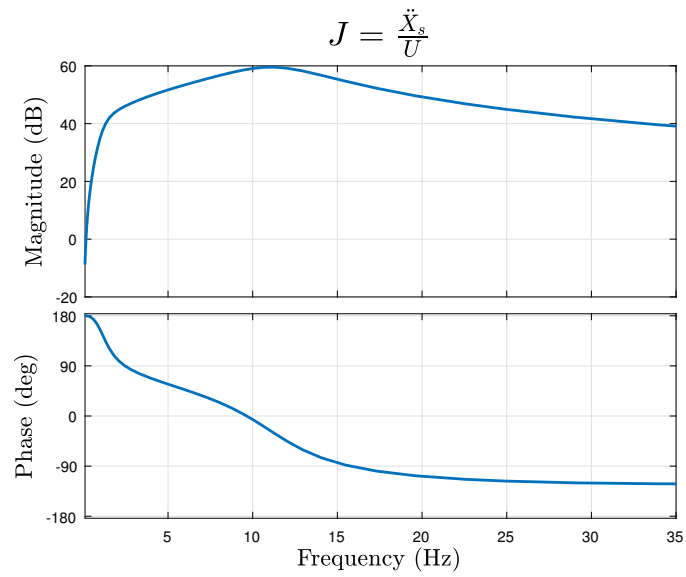


Figure C.11: Bode diagram for amplitude and phase of the transfer function J between the sprung mass acceleration and the input signal in case of quarter car with the rubber top mount.

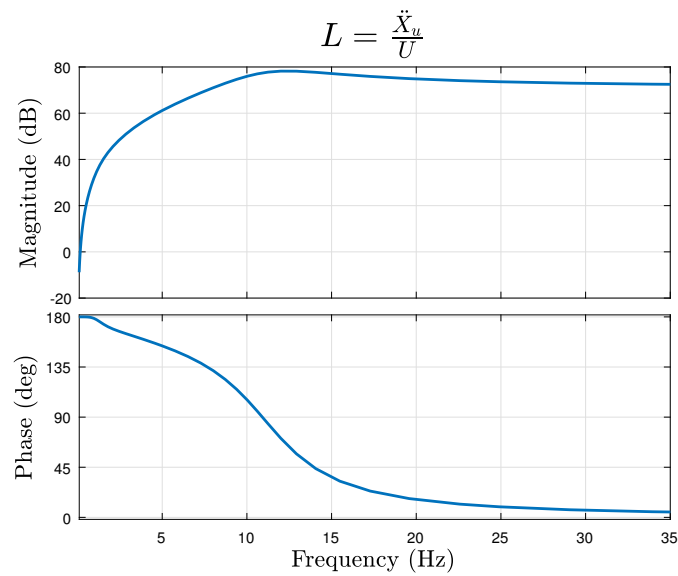


Figure C.12: Bode diagram for amplitude and phase of the transfer function L between the unsprung mass acceleration and the input signal in case of quarter car with the rubber top mount.

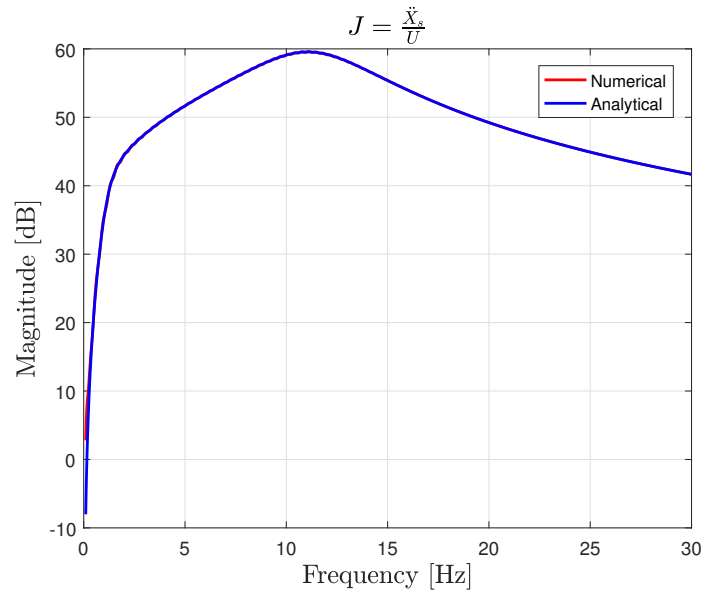


Figure C.13: Comparison between the analytic and estimated amplitude Bode diagram of the transfer function J for the quarter car model with the rubber top mount.

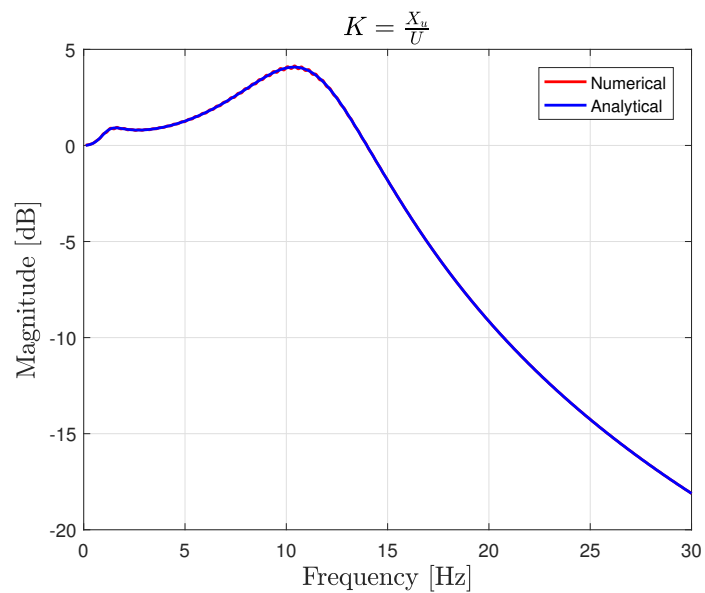


Figure C.14: Comparison between the analytic and estimated amplitude Bode diagram of the transfer function K for the quarter car model with the rubber top mount.

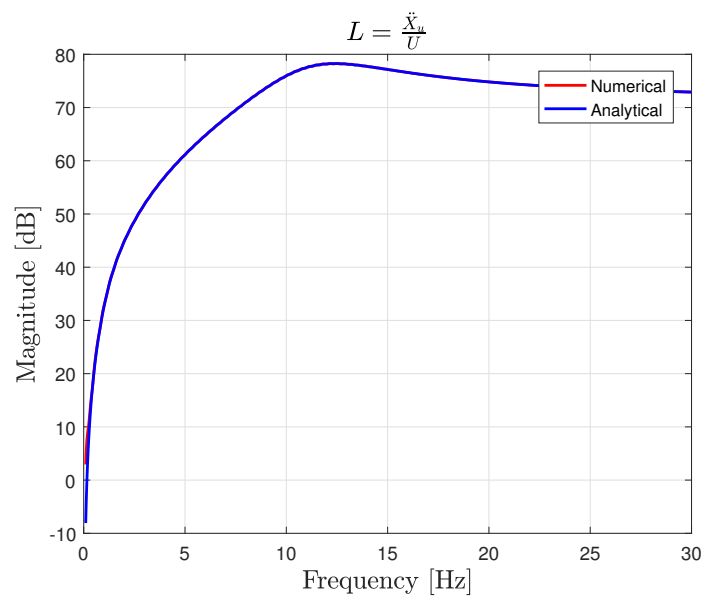


Figure C.15: Comparison between the analytic and estimated amplitude Bode diagram of the transfer function L for the quarter car model with the rubber top mount.

C.3 Nonlinear Quarter Car Models with the Hydraulic Top Mount

C.3.1 Time Histories

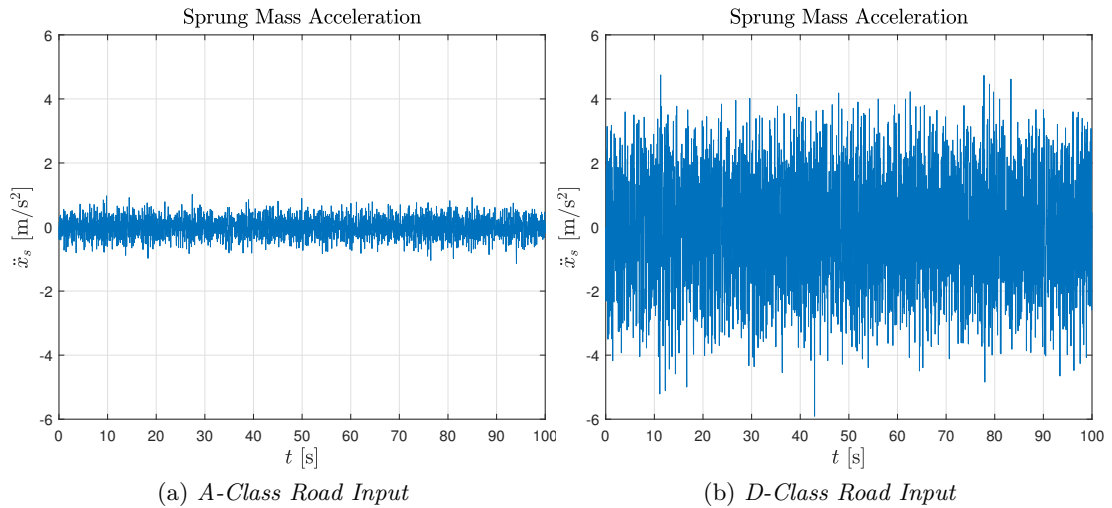


Figure C.16: Sprung mass acceleration in function of time for the quarter car model with the hydraulic top mount in case of A-class road input (a) and D-class road input (b).

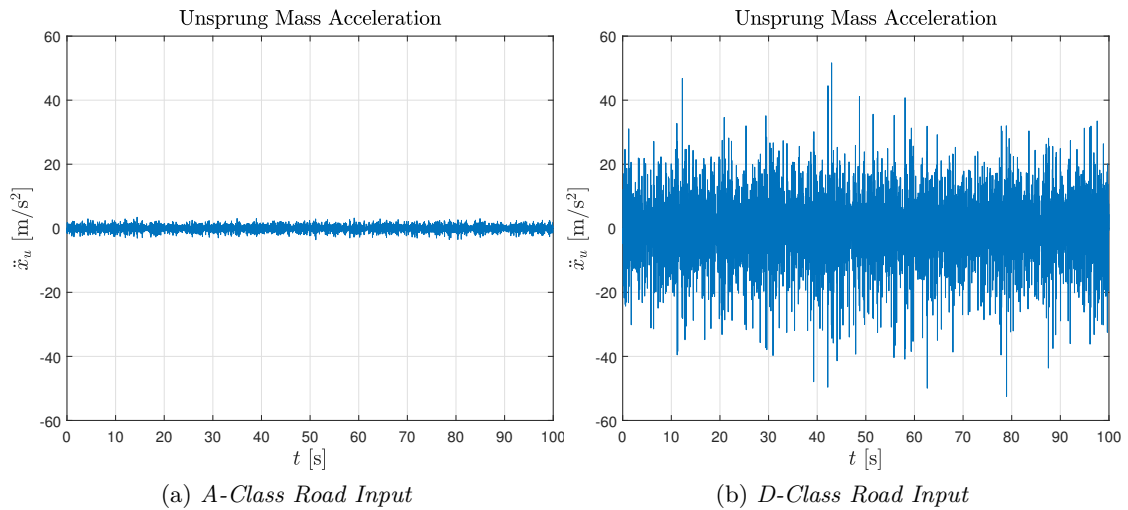


Figure C.17: Unsprung mass acceleration in function of time for the quarter car model with the hydraulic top mount in case of A-class road input (a) and D-class road input (b).

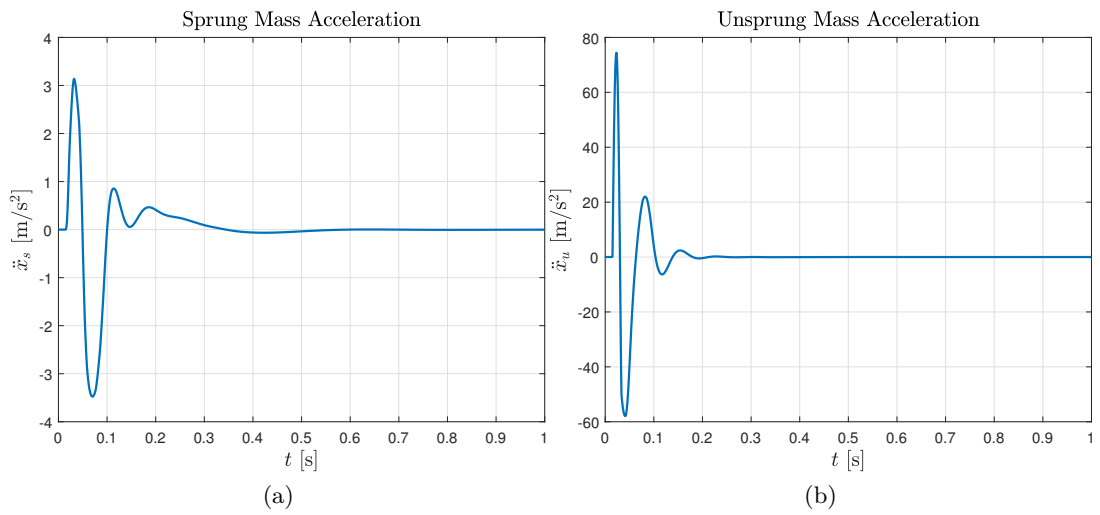


Figure C.18: Sprung and unsprung mass acceleration in function of time for the quarter car model with the hydraulic top mount in case of single asperity input signal.

C.4 Nonlinear Quarter Car Model with the Rubber Top Mount

C.4.1 Time Histories

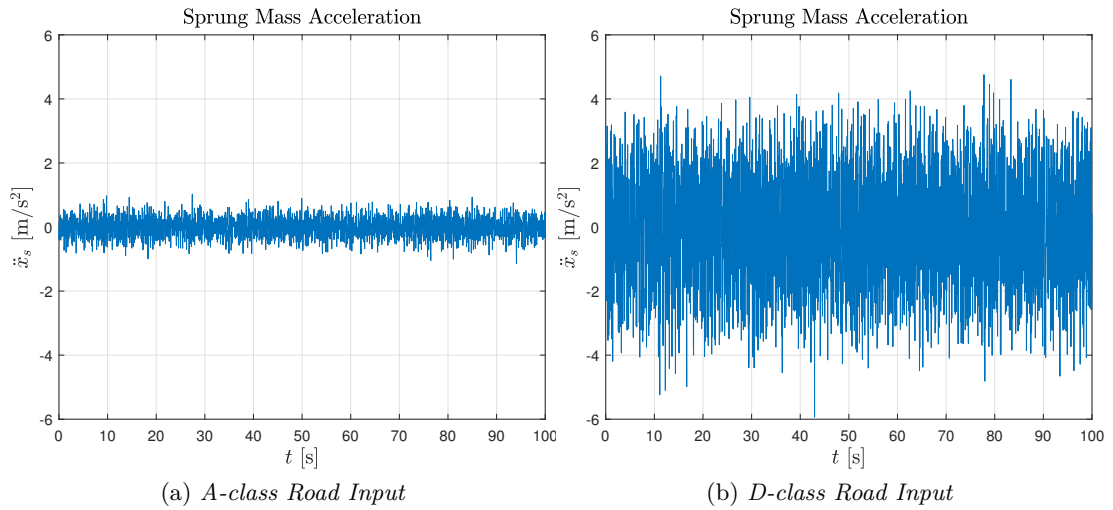


Figure C.19: Sprung mass acceleration in function of time for the quarter car model with the rubber top mount in case of A-class road input (a) and D-class road input (b).

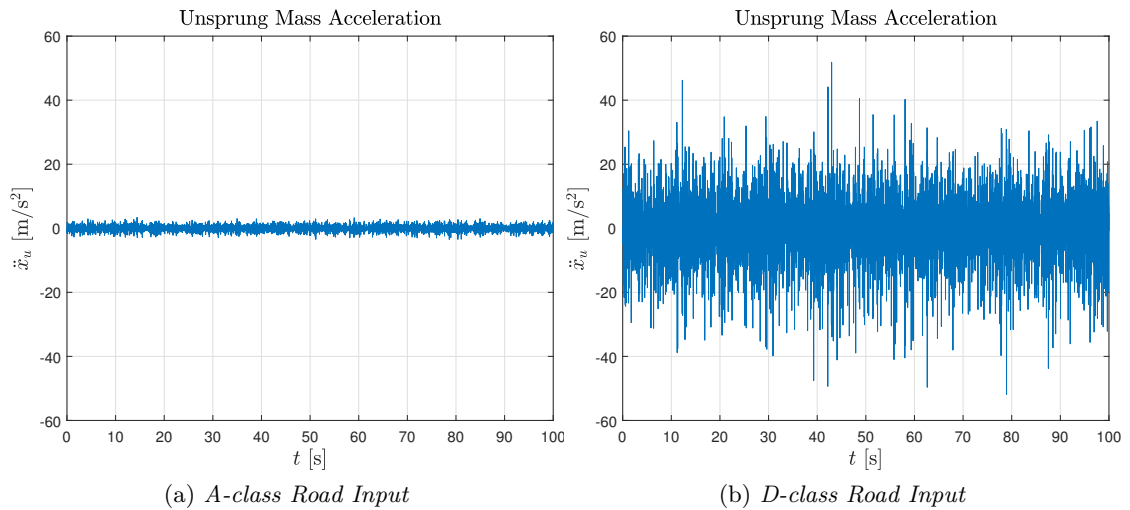


Figure C.20: Unsprung mass acceleration in function of time for the quarter car model with the rubber top mount in case of A-class road input (a) and D-class road input (b).

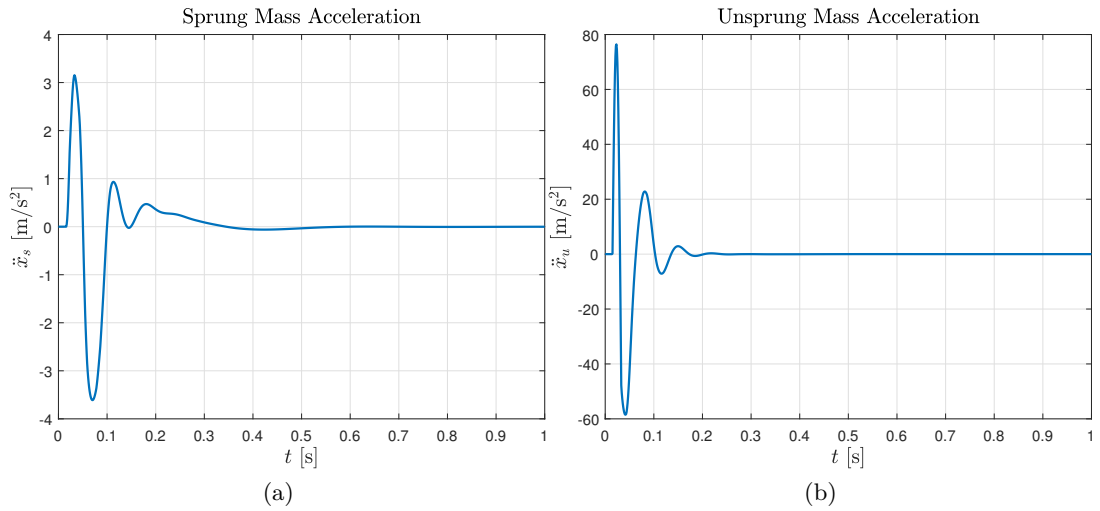


Figure C.21: Sprung and unsprung mass acceleration in function of time for the quarter car model with the hydraulic top mount in case of single asperity input.

C.5 Nonlinear Quarter Car Models with the Hydraulic Top Mount in Series with Suspension Strut

C.5.1 Time Histories

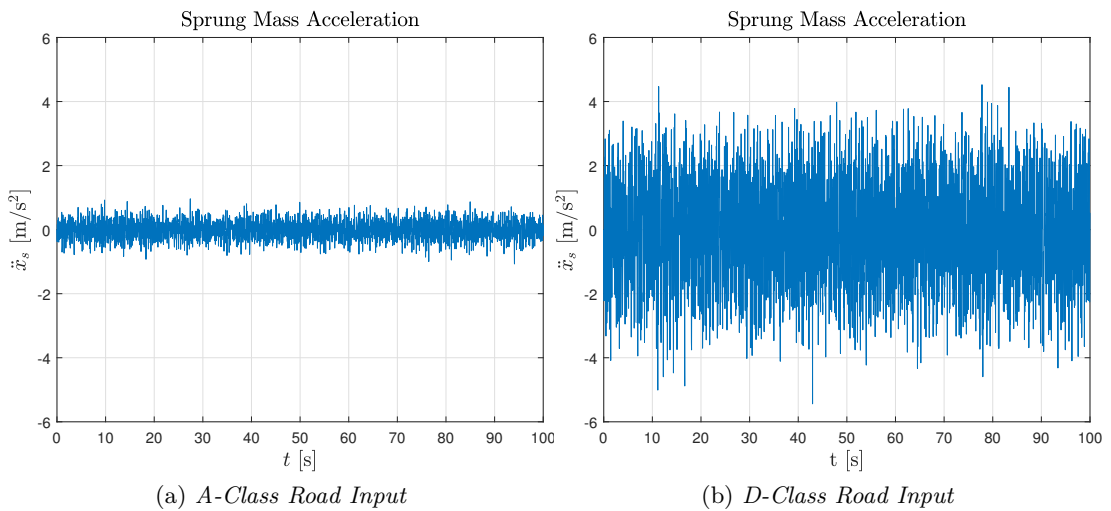


Figure C.22: Sprung mass acceleration in function of time for the quarter car model with the hydraulic top mount in case of A-class road input (a) and D-class road input (b).

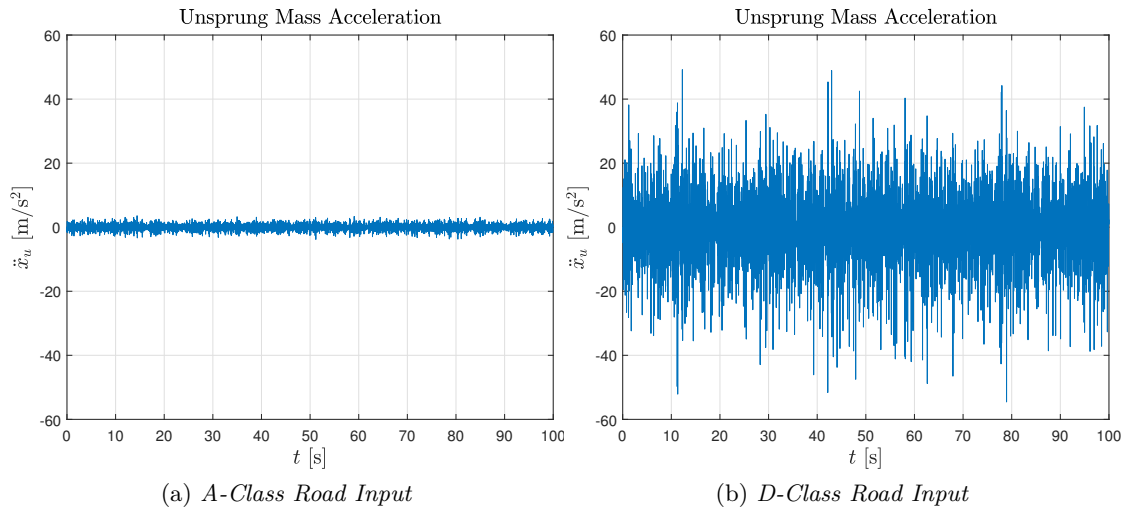


Figure C.23: Unsprung mass acceleration in function of time for the quarter car model with the hydraulic top mount in case of A-class road input (a) and D-class road input (b).

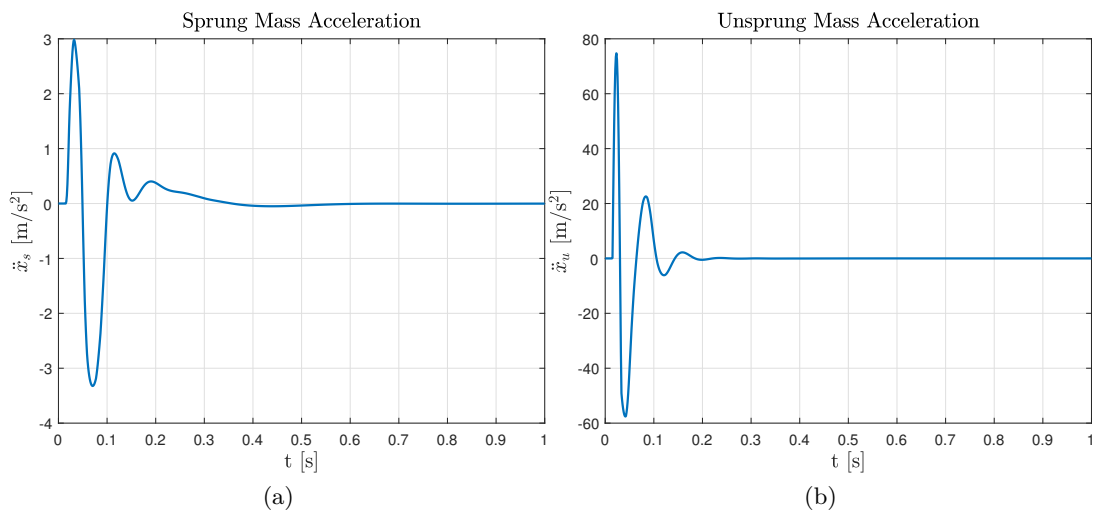


Figure C.24: Sprung and unsprung mass acceleration in function of time for the quarter car model with the hydraulic top mount in case of single asperity input signal.

Vita Auctoris

NAME: Salvatore Marco Cubisino

PLACE OF BIRTH: Catania

YEAR OF BIRTH: 1995

EDUCATION: Politecnico di Torino, B.Sc in Automotive Engineering, Torino, Italy, 2016

Politecnico di Torino, M.Sc in Automotive Engineering, Torino, Italy, 2018

University of Windsor, M.Sc in Automotive Engineering, Windsor, ON, Canada, 2018